

Engineered Protein Circuits for Cancer
Therapy

Thesis by
Andrew C. Lu

In Partial Fulfillment of the Requirements for
the degree of
Synthetic Biology and Systems Biology, PhD

The Caltech logo, featuring the word "Caltech" in a bold, orange, sans-serif font, centered within a light yellow rectangular background.

CALIFORNIA INSTITUTE OF TECHNOLOGY
Pasadena, California

2025
(Defended June 6th 2025)

ACKNOWLEDGEMENTS

It's often said that you should keep work and personal life separate. Never, under any circumstances, work with your significant other. Well, I have found that advice to be untrue for me personally. I love science and my work. It is an absolute privilege to do something that feels as much like a hobby as it does a profession. So it's even more of a privilege to be able to share this hobby with the most important person in my life, Victoria. I love that I can ask Victoria for advice during experiments, or get her feedback on the grant I'm writing. I love that we can be excited for each other's new data, because we actually understand the nuances of each other's experiments and how they fit into the bigger picture of our scientific story. Of course, sometimes we're tired, things are not going so well, and we don't want to talk about work. But the amazing part of being married and sharing a life together is that work is only a fraction of all that we have. So I want to start this section by acknowledging Victoria, who is my newly married wife (8/31/2024!), best friend, and fellow lab mate. We met almost 10 years ago now (fittingly, during a summer research program as undergraduates). A decade later, we are found again inseparable, at the same institution at Caltech, and in the same lab with Michael. During this time, we did everything as a team. We graduated college together, applied for jobs together, applied for MD-PhD and DVM-PhD programs together, and joined the same lab together. Victoria has always been here every step along the way while completing my thesis work, and I am so looking forward to what comes next for the both of us.

At this point, one might be wondering why Victoria and I joined the same lab at Caltech. Funnily enough, we explicitly talked about this before starting graduate school and decided that it was probably best if we learned complementary skill sets during training. This, of course, usually means joining different labs.

Well, one fateful evening in April 2021, before I started my rotation in Michael's lab, I was working on a grant with Michael to use some of the technology in the lab to do cell-based delivery of circuits to reprogram macrophages. As we discussed, I quickly realized that I was the wrong person to be in this meeting; this was much better suited for Victoria, who at that

point had spent most of her scientific journey in the world of immunology. The meeting was on Zoom, and I waved to the side for Victoria to listen in on our discussion. Towards the end of the meeting, I mentioned that my partner had experience working with immune cells, and might be a good person to join our quest.

Fast forward a few weeks, Victoria and I ended up spending quite a bit of time working together on this grant with Michael. Towards the end of this process, we both recognized something that felt true, even if we didn't yet see how much it would matter. Working with Michael was inspiring, challenging, fun—everything you could possibly ever want in a PI. I distinctly remember we went on a long walk around Davis, where we were at the time, when we both realized that we might want to rotate in the Elowitz lab.

Four years later—we both firmly believe that the decision to join Michael's lab was, separately, one of the best decisions we have ever made. It is a true testament to the breadth and depth of the lab that Victoria and I have been able to join the same lab and yet work on completely different topics and still learn very complementary skills.

While writing this thesis, I looked at quite a lot of former grad students' theses in the lab just to see how they structured their chapters. In doing so, I always took a quick peek at their acknowledgment sections. It's interesting—people always talk about Michael with the highest praise, and almost always in much the same way. I will again echo those sentiments here. Michael is truly the best combination of kind, youthfully inquisitive, curious, supportive, and absolutely brilliant scientist and human being I have ever met or probably will ever meet. From Michael, I learned that it's okay to not understand something, to ask the “dumb” questions, to question all assumptions, and to think general and out of the box. Often, I will go into a meeting with a very specific agenda, only to be “derailed” by some of Michael's thoughts, only to realize a few days later how deep and insightful his thoughts really were.

One thing that is maybe a little less talked about with Michael is his unique ability as a people manager. He is thoughtful about any signs of potential conflict, is sensitive to the problems and feelings of all the different personalities in the lab, and seems to have an intuitive sense

for when to push people or when to let them wander a little. Whenever a new rotation student joins, I always say that joining our lab feels like joining a small lab (in terms of the attention you get from the PI) disguised as a big lab (with enough resources and support to do what you want to do).

I also want to take this time to thank everyone who has helped me along my scientific journey. A special thank you to Dr. Gayle Slaughter of the Baylor College of Medicine summer undergraduate research program, who encouraged me to pursue science and put me in the lab of Dr. Bert O'Malley. It was in Dr. O'Malley's lab that I got to learn from Aarti Rohira, a smart and amazingly kind postdoc who was patient enough to teach an overzealous undergraduate. The following year, when I took a leave of absence from Berkeley to continue working in the O'Malley lab, I got a taste of what it meant to do independent research, and the amazing wonders of using science to answer questions about basic cancer biology. Thank you to Dr. Robert Tjian, who allowed me to join his lab when I returned to Berkeley. In the Tjian Lab, I had the fortune to work with a brilliant, meticulous, and thoughtful graduate student, Kevin Tsui, who showed me that it is possible to develop fundamentally new technologies to answer fundamental questions in biology. After college graduation, I was so fortunate to get a job in Jimmie Ye's lab at UCSF, and to learn alongside the lab of Alex Marson, where I learned the wonders of using two new and converging technologies to study primary human T cells: genome-wide CRISPR knockout screens with single-cell transcriptomics. During medical school, I had the fortune to work with Dr. Brunilda Balliu and Noah Zaitlen, statistical geneticists who introduced me to the brilliantly complex world of how statistics can be used to identify underlying molecular mechanisms of complex diseases.

During grad school, there are so many people to thank for both directly and indirectly helping me with the work I describe in this thesis. During medical school at UCLA, I was incredibly fortunate to be paired with David Dawson as my MSTP advisor. Ever since starting the UCLA MSTP program, and well into my PhD, Dave has always been kind, knowledgeable, and has gone above and beyond to help me in my career goals. He volunteered to introduce me to colleagues at UCLA, who have given us access to clinical tumor samples that Caltech

unfortunately lacks access to. I thank my committee at Caltech—Mikhail Shapiro, Rebecca Voorhees, and Viviana Gradinaru—who have asked me insightful questions and helped guide my scientific story.

To all the Elowitz lab members, past and present, thank you all for making this grad school journey so fun and intellectually stimulating (in mostly chronological order): Mark Budde for bringing me into the lab, Haley Larson for being there at the beginning of the project with me and helping with experiments, Shiyu Xia for teaching me the value of working fast and efficiently while having dedication to your craft and what you are most passionate about, Xiajong Gao, Lucy Chong, Mike Flynn, and all other “CHOMPers” for giving me the opportunity to work on such a great technology, Ali Ahmed Diaz for working with me and exploring the wonders of β -Catenin and Sortases. Huge, massive thank you to Lukas, for choosing to rotate with me and then becoming my partner in crime for the past two years—for being equally an intellectual sparring partner, conference travel buddy, friend outside of lab, and future startup partner. Thank you to Kevin Ho for joining our work in the past year—it was pure serendipity that Lukas and I decided, while at a conference in West Los Angeles, to reach out to the PCC program to see if they had any interested interns, and pure chance that the interview process just happened to be the week that we reached out. We wouldn't have been able to explore so many interesting questions and directions if it wasn't for the help of Kevin and how reliable and consistent he is. Thank you to Evan Zhang for showing me that Caltech undergraduate students are truly special and for doing excellent work both experimentally and analytically. And finally, thank you to all the Elowitz lab members who I have had the fortunate to learn from and befriend – Roni, Bo, Dhiraj, Dongyang, Duncan, Rongrong, Jan, Kaiwen, Evan, Jacob, Martin, Zibo, Felix, among many others.

Special big thank you to Leah for all the fun tennis lessons and even battles, for all the times we stayed behind in the tennis court parking lot exchanging stories, and for all the times in the TC room we talked about all the annoyances and joys of our lives. Leah and I never worked together, and I love that, because in her I feel like I have a friend and not a coworker.

To James, for whom the lab would truly not run without you—through all the never-ending issues with the Cytoflex, or the sorter, or the Olympus, or basically every possible device in the lab. Both intellectual discussions and random fun conversations with James always make the lab that much more fun to be in.

Thank you to Jo Leonardo for being such a kind and helpful lab administrator, and for keeping the lab running so smoothly during the first two years of my PhD. Thank you to Rui for stepping in seamlessly, never missing a beat, and continuing the amazing work and kindness that keep the lab running.

Massive thank you to our UT Southwestern collaborators: Stephen Moore, Daniel Siegwart, and Hao Zhu, who have taught me so much about the world of animal experiments, *in vivo* delivery, and how cancer biologists approach problems. Thank you for making working together so enjoyable and stimulating, and for helping us conceive and execute *in vivo* tumor experiments that we would otherwise have no idea how to do.

Finally, last but certainly not least, I want to thank the people in my life outside of science who have been here for me all along the way. To my mother Lily, father Scott, and sister Jennifer, thank you for supporting me throughout this journey even though I'm 30 years old and still in school. To my aunts, uncles, and all my relatives who spent time raising me in Canada, Taiwan, and Texas—thank you for instilling in me all the different values and traits that you all hold dear. To my new in-laws, Carole and Jack, thank you for raising a brilliant, kind, insightful, and sensitive daughter, without whom none of my life would have been remotely the same. And thank you for always supporting me, whether it is eagerly waiting for the results from a grant I applied for or flying out to Pasadena just for my graduation.

To my friends at Caltech: Hristos, Jacob, Roey, Gerbs, Ethan, Josh, Martin, Arun, Seymour. I truly cannot understate how much of an impact you all have had on me and my life forever. I never would have thought that I would be leaving grad school with a life-long friend group of brilliant and hilarious PhD students whose interests range from gravitational waves and theoretical physics, to biology, neuroscience, bioengineering, and chemistry. As we graduate

and go about our separate lives, I know for a fact that even when we're 50 years old, we will always be the same group of people that we have been for the past four years.

ABSTRACT

The fundamental challenge of cancer therapy is to specifically eliminate cancer cells while sparing healthy tissue. Targeted therapies represent a breakthrough towards this goal. However, their long-term efficacy is limited by resistance, which often occurs because targeted therapies do not kill cancer cells directly. Instead, they partially block the oncogenic signals that tumors use to drive uncontrolled growth, leaving many escape routes that allow tumors to adapt and develop resistance. **Chapter 1** introduces these ideas, starting with a definition of cancer, the mechanisms underlying the hallmarks of cancer, and the current approaches to “precision oncology” and fundamental limitations of these approaches. The end of chapter 1 will describe the emergence of a relatively nascent field combining cancer biology and synthetic biology. More specifically, engineered protein circuits have been envisioned as an alternative to targeted therapies. Rather than block oncogenic signals, circuits use engineered proteins to directly link oncogenic signals to cell death, potentially circumventing the resistance mechanisms that limit targeted therapies. However, it has remained unclear what circuit designs could operate effectively, and what advantages protein circuits could provide compared to existing small molecule inhibitors. In this thesis, we demonstrate proof-of-concept for engineered protein circuits by targeting the oncogene Ras, which drives roughly one in four human cancers. Our engineered protein circuits are composed of three components. **Chapter 2** describes the engineering of a protease-based sensor that responds to a broad spectrum of clinically relevant Ras mutations. **Chapter 3** chronicles the journey to engineering a protease-based signal amplifier, inspired by natural proteolytic cascades that provide signal amplification. **Chapter 4** describes our implementation of a full therapeutic circuit, where we couple Ras sensors, signal amplifier, and a protease-activatable cell death effector. The effector can trigger either non-inflammatory apoptosis or immunogenic pyroptosis, which has been shown to extend therapeutic effects beyond transfected cells. We demonstrate that, delivered as mRNA in lipid nanoparticles (LNPs), circuits accurately discriminated between Ras-mutant cancer and non-cancer cells, potently eliminated cells resistant to the state-of-the-art Ras-targeting drugs Sotorasib and RMC-7977 in vitro, and cleared induced aggressive, multifocal liver tumors in mice. These results establish a programmable mechanism for treating cancer and other human diseases.

PUBLISHED CONTENT AND CONTRIBUTIONS

Lu, A., Moeller, L.*, Moore, S.*, Xia, S., Ho, K., Zhang, E., Budde, M. W., Larson, H., Ahmed Diaz, A., Gu, B., Linton, J. M., Klock, L., Flynn, M. J., Gao, X. J., Siegwart, D. J., Zhu, H., & Elowitz, M. B. (2025). Engineered protein circuits for cancer therapy. In *bioRxiv* (p. 2025.04. 16.647665). <https://doi.org/10.1101/2025.04.16.647665>

A.L. conceived the project, designed the study, performed experiments, analyzed data, and wrote the manuscript.

Xia, S., **Lu, A. C.**, Tobin, V., Luo, K., Moeller, L., Shon, D. J., Du, R., Linton, J. M., Sui, M., Horns, F., & Elowitz, M. B. (2024). Synthetic protein circuits for programmable control of mammalian cell death. *Cell*, *187*(11), 2785–2800.e16. <https://doi.org/10.1016/j.cell.2024.03.031>

A.L. performed experiments, analyzed data, and participated in revision of manuscript.

Duan, M., Dev, I., **Lu, A.**, Ayrapetyan, G., You, M. Y., & Shapiro, M. G. (2024). SEMPER: Stoichiometric expression of mRNA polycistrons by eukaryotic ribosomes for compact, ratio-tunable multi-gene expression. *Cell Systems*, *15*(7), 597–609.e4. <https://doi.org/10.1016/j.cels.2024.06.001>

A.L. performed experiments and analyzed data.

Ma, Y., Budde, M. W., Mayalu, M. N., Zhu, J., **Lu, A. C.**, Murray, R. M., & Elowitz, M. B. (2022). Synthetic mammalian signaling circuits for robust cell population control. *Cell*, *185*(6), 967–979.e12. <https://doi.org/10.1016/j.cell.2022.01.026>

A.L. performed experiments.

TABLE OF CONTENTS

Acknowledgements	iv
Abstract.....	v
Published Content and Contributions	vi
Table of Contents	vii
List of Illustrations and/or Tables	viii
Chapter I: Introduction.....	1
1.1 What is cancer?	1
1.2 What are current therapeutic strategies for cancer?	4
1.3 How does the human body detect and eliminate nascent cancer?	6
1.4 How would a synthetic biologist treat cancer?.....	8
Chapter II: Engineering of mutant Ras sensors	18
2.1 Summary	18
2.2 Introduction	19
2.3 Results	20
2.3.1 Engineered sensors respond to diverse Ras mutations.....	20
2.3.2 Learnings from engineering synthetic sensor modules	25
2.4 Supplementary figures	28
2.5 Methods	33
2.5.2 Key resources table	39
Bibliography.....	48
Chapter III: Sensor optimization and signal amplification.....	52
3.1 Summary	52
3.2 Introduction	52
3.3 Results	53
3.3.1 Cis-protease regulation improves sensor sensitivity	53
3.3.2 Design of protease-activatable proteases.....	55
3.3.2 Signal amplification improves sensor sensitivity	58
3.4 Methods	60
3.4.2 Key resources table	63
Bibliography.....	67
Chapter IV: Rewiring of mutant Ras sensing to cell death	70
4.1 Summary	70
4.2 Introduction	70
4.3 Results	71
4.3.1 Circuits potently eliminate Ras-mutant cancer cells	71
4.3.2 Circuits do not respond to endogenous Ras signaling or perturb gene expression.....	74

4.3.3 Circuits prevent and treat induced liver tumors <i>in vivo</i>	75
4.3.4 Circuits kill drug-resistant cells	80
4.4 Supplementary figures	83
4.5 Methods	91
Bibliography	103
Chapter V: Conclusions	107
5.1 Discussions	107
5.2 Future directions.....	114
Bibliography	115

LIST OF ILLUSTRATIONS

<i>Number</i>	<i>Page</i>
2.1 Engineered protein circuits selectively target cancer cells (schematic).....	20
2.2 Engineered sensors specifically respond to mutant Ras.....	22
S2.1 Previous RAF1-based Ras sensor insufficiently discriminated mutant and wild-type Ras.	28
S2.2 Ras binder screen identifies Ras-mutant-specific sensors.....	29
S2.3 Ras expression dependency of individual sensor responses	31
S2.4 Characterization of Ras sensors v1 and v2.....	32
3.1 Cis protease regulation increases sensitivity	54
3.2 Design and characterization of amplifiers	57
3.3 Trans protease regulation increases sensitivity.....	59
4.1 Therapeutic circuits potently and selectively eliminate Ras-mutant cancer cells.....	73
4.2 Therapeutic circuits prevent and treat liver tumors <i>in vivo</i>	77
4.3 Circuits are less susceptible to intrinsic and acquired resistance compared to Ras-targeting drugs	83
S4.1 mRNA Delivery via LNP and treatment effects on transcriptome	85
S4.2 In vivo tumor prevention	87
S4.3 Quantification of effects in tumor prevention and mRNA-LNP treatment experiments	88
S4.4 Gross images of mouse livers after mRNA-LNP treatment.....	89
S4.5 Comparison of circuit and Ras inhibitors Sotorasib and RMC-7977 ...	90

Chapter 1

INTRODUCTION

1.1 What is cancer?

Cancer is a disease marked by uncontrolled proliferation of cells that eventually invade surrounding tissues and compromise organ function[1]. This disease process occurs through a set of common hallmarks such as sustained proliferative signaling, limitless replication, induction of angiogenesis, and activation of invasion and metastasis[2–4]. By acquiring these hallmarks, a tumor can expand, disseminate, and ultimately overwhelm the body’s normal homeostatic systems.

The somatic-mutation theory is one prevailing model of cancer initiation[5]. This theory states that oncogenic DNA mutations are the underlying causes of the cancer hallmarks and has guided much of the scientific understanding of cancer in the past decades. In particular, the advent and exponential improvement of DNA sequencing has made studying DNA mutations increasingly cost effective and accessible, ushering in an era of “precision oncology” based on genetics[6–9].

Yet, several observations contradict a purely genetic model of cancer initiation. For one, many aggressive tumors show no recurrent driver mutation even after exhaustive sequencing. For example, Posterior fossa group A (PFA) ependymomas are lethal pediatric brain tumors that seem to lack any recurrent DNA mutations or gene fusions[10]. If mutations are the drivers of cancer hallmarks, how did these aggressive tumors form?

Additionally, recent work on deep sequencing of healthy human tissue has revealed that canonical driver mutations are frequently found in healthy tissue. For example, human skin sequencing revealed 20-30% of epidermal cells contain mutations in classic drivers such as TP53 and NOTCH1, yet the same tissues remain histologically normal[11].

Finally, perhaps most interestingly, treatment resistance can emerge without any changes in the underlying genome. Single-cell RNA FISH and live-cell imaging revealed that even monoclonal, isogenic cultures of BRAF-mutant melanoma cells can display profound variability in drug resistance in response to a BRAF inhibitor vemurafenib[12]. This drug resistance can be predicted by the expression of a “pre-resistance” program in an ultra-rare population that preferentially survives drug treatment. Critically, this resistance population remains genetically identical to the parental population. This seminal work by Sydney Shaffer and Arjun Raj demonstrated that durable resistance is possible in an otherwise genetically uniform population, establishing a clear non-genetic pathway to therapeutic failure.

In a complementary well-known study, Sharma et al. used multiple drug-sensitive cancer cell lines (e.g. EGFR-mutant PC9 lung cancer cells) to study resistance to targeted therapy. They found that roughly 1/1000 cells survived weeks-long exposure to saturating concentrations of a kinase-inhibitor, giving rise to colonies they called “drug-tolerant persisters.” These survivors remained genetically identical to the parental population yet displayed more than 100-fold higher resistance to drug. Interestingly, these drug persistent states requires a distinct chromatin state maintained by a specific histone demethylase (KDM5A). Accordingly, co-treatment with a HDAC inhibitor selectively eliminated the persister pool. Additionally, when drug was removed from media (“drug holiday”), these cells rapidly reverted to original wild-type sensitivity, confirming that the tolerant phenotype was reversible and epigenetic rather than genetically encoded.

The Shaffer et al. paper showed that ultra-rare melanoma cells can pre-exist in a transcriptional program that predicts survival, whereas the Sharma et al. paper demonstrates that phenotypically similar persisters can also arise through stochastic entry into a chromatin-regulated state after therapy has begun. Together, these papers reveal that tumors can leverage both pre-existing and inducible epigenetic heterogeneity to escape targeted drugs without altering their genomes. This insight argues that durable responses will require strategies that couple oncogene inhibition with agents that prevent

entry into (or force exit from) these adaptive states, for example selective epigenetic modulators. Additionally, it strengthens a cell-state-centric view of cancer in which dynamic chromatin and transcriptional regulation are as critical as genotype.

These observations thus provoke the question: *why should cancer be considered only a genetic disease?*

Indeed, all cells in the human body arise from an isogenic cell population, yet develop into distinct phenotypes. The fundamental principle underlying this capability is that cells differ not in their genomes, but in the entire configuration of all cellular activities and states, such as transcriptomes, proteomes, protein localizations, post-translational modifications, and epigenetic marks.

Thus, an alternative, more holistic view of the causes of cancer can be described as: any changes to the cell, at the epigenetic, genetic, transcriptomic, and protein levels, that have the potential to move cells into pathological states that display the hallmarks of cancer. We will next explore the implications of this alternative way to think about cancer, and how it might guide us to better cancer therapeutics.

1.2: What are current therapeutic strategies for cancer?

The fundamental challenge of cancer therapy is to eliminate malignant cells while sparing healthy tissue. This principle underlies the development of targeted therapies, which aim to exploit cancer-specific molecular vulnerabilities to achieve selective cytotoxicity.

Several landmark therapies illustrate this targeted therapies paradigm. The development of trastuzumab by Dennis Slamon's work on HER2-amplified breast cancer established that tumors driven by specific oncogenic alterations could be treated with molecular precision[11,13]. In hematologic malignancies, the identification of the BCR-ABL fusion gene in chronic myeloid leukemia (CML) led to the development of imatinib, a selective kinase inhibitor that fundamentally altered the course of the blood cancers[11,13–16]. More recently, inhibitors of the Ras oncogene such as Sotorasib (KRAS G12C) and RMC-7977 (pan-RAS) by Revolution Medicines have achieved what was once considered impossible: direct pharmacological inhibition of a historically “undruggable” oncogene[17–20].

Despite these landmark successes, many other efforts to apply the targeted therapy paradigm have fallen short. Most approved targeted therapies are effective only in a narrow subset of patients, often provide limited survival benefit, and frequently encounter resistance within months of treatment initiation. For instance, while EGFR inhibitors can induce dramatic responses in EGFR-mutant non-small cell lung cancer (NSCLC), nearly all patients eventually relapse[21–23]. Similarly, BRAF inhibitors in melanoma, ALK inhibitors in NSCLC, and IDH1 inhibitors in glioma show initial promise, but rarely achieve durable remission[24,25]. Broadly speaking, the field of oncology continues to face sobering statistics: fewer than 10% of oncology drugs entering Phase I trials eventually receive FDA approval, and most patients with advanced solid tumors ultimately die of their disease[26,27].

To understand why targeted therapies have not lived up to their promise, it is helpful to revisit our definition of cancer from Chapter 1.1. A foundational assumption of the

targeted therapy paradigm is that the majority of malignant cells in a tumor share a common “driver” mutation. This assumption stems from the somatic mutation theory of cancer, but it is increasingly challenged by real-world tumor heterogeneity. For example, multi-region sequencing of renal cell carcinomas revealed that many mutations classified as “drivers” were only present in some tumor regions, and often absent in others[28,29]. In such cases, even a perfectly effective inhibitor of a given mutation would only eliminate a subset of tumor cells, leaving others untouched and able to repopulate the tumor.

The concept of “trunk” mutations offers a partial solution[30]. Trunk mutations are alterations that occur early in tumor evolution and are therefore shared by the majority of cancer cells in a given tumor. In hepatocellular carcinoma (HCC), for example, at least one trunk mutation, such as in TERT, TP53, or CTNNB1, was detected in over half of patients, defined as more than 90% of tumor regions within a patient harboring at least one of these mutations[31].

However, this leads to a second problem: many of these ubiquitous mutations are not actionable with current therapeutic strategies. TERT reactivation, while nearly universal in HCC, is difficult to target therapeutically[32]. Inhibiting TERT protein has delayed effects, since telomeres shorten gradually over many cell divisions[33]. Moreover, many cancer cells can activate alternative telomere maintenance mechanisms, and TERT also has non-canonical, telomere-independent functions that may support tumor growth and survival[33,34]. TP53 is a tumor suppressor, and restoring its function pharmacologically remains an unsolved challenge. CTNNB1 mutations activate the Wnt/ β -catenin pathway, a critical signaling axis in normal development and tissue homeostasis, making it hard to inhibit without systemic toxicity[35–37].

Thus, precision oncology’s reliance on inhibition of genetically defined targets narrows an already narrow therapeutic window. Not only is the search for shared mutations limited by tumor heterogeneity, but even when common mutations are found, they often reside in genes that are undruggable or risky to target.

Finally, therapeutic resistance remains a near-universal outcome. The prevailing explanation, that resistance emerges through additional DNA mutations, is supported by a mountain of sequencing data. Yet, this genetic model fails to account for resistance mechanisms that do not involve new mutations. As discussed in Chapter 1.1, genetically identical cells can adopt transcriptional states that predict drug tolerance in BRAF-mutant melanoma cells. These rare, pre-resistant states enable survival and regrowth even in the absence of any genomic change. Cancer, then, is not just a collection of mutant clones, but a dynamical system capable of shifting into distinct cell states such as epithelial-to-mesenchymal transition, drug-tolerant persister formation, or lineage plasticity.

1.3 How does the body detect and eliminate nascent cancer?

Given these limitations of targeted therapies, in particular: the failure of the somatic mutation theory to fully explain cancer, the non-lethal consequences of inhibiting many mutated genes, and the near-universal emergence of resistance, we can think about alternative modalities to treat this disease. Here, we will ask: how does the body itself deal with the threat of cancer? And are there any principles that might inspire us to build synthetic therapeutics?

The human body continuously forms and eliminates potentially cancerous cells. This intrinsic tumor suppression is largely carried out by robust surveillance systems, the most prominent of which is the p53 pathway[38–41]. Often called the “guardian of the genome,” p53 orchestrates a multi-layered defense program that detects abnormal cellular states and eliminates at-risk cells before they can become malignant[42,43].

In contrast to targeted therapies and precision oncology as is currently defined, the p53 surveillance system can be conceptualized as a sense-process-actuate circuit:

Sense: p53 does not detect DNA mutations directly. Rather, it senses a wide range of upstream stress signals associated with transformation risk. These include DNA damage, aberrant oncogene activation (such as Ras or Myc overexpression), hypoxia, and

ribosomal stress. In this way, it serves as a broad-spectrum detector of cellular danger[44,45].

Process: p53 does not respond in a binary fashion. Once activated, p53 integrates the strength, duration, and context of the input signals through a feedback-rich protein-level network[46].

Actuate: p53 does not merely inhibit pathways. It *actively* executes responses through direct induction of effector proteins. These include genes that trigger cell-cycle arrest (e.g., CDKN1A/p21), DNA repair (e.g., GADD45), senescence (via p16INK4a, among others), or apoptosis (e.g., BAX, PUMA, NOXA). In doing so, it commits damaged or stressed cells to irreversible fates that prevent malignant transformation[39,46].

This endogenous tumor-suppressive architecture, broad in sensing, nuanced in processing, and direct in action, raises a compelling question:

Can we design synthetic systems that mimic these principles to detect and eliminate cancer more effectively than current therapies?

1.4: How could a synthetic biologist treat cancer?

Over the past few decades, the field of synthetic biology has created a vast array of tools for the design of synthetic circuits at the genetic, transcriptional, or post-transcriptional level. Increasingly, these toolboxes are being applied in fields such as cell therapies/CAR-T cells and gene therapies to increase the specificity and fine tune the spatial and temporal resolution of therapeutic responses. Here, I will discuss some of the pioneering work in the synthetic biology field, spanning DNA, RNA, and protein level systems.

The vast majority of synthetic biology efforts to date have focused on regulating gene expression, in part because transcription factors and other DNA-binding proteins have been extensively studied and offer a well-developed foundation for building layered control systems. One such system uses modular gene circuits to selectively detect and respond to RAS oncogene driven signaling[47]. The first layer of specificity comes from a direct protein-level sensor: a fusion of the Ras-binding domain and cysteine-rich domain (RBD-CRD) from CRAF to engineered bacterial NarX kinases. In the presence of elevated RAS-GTP, a hallmark of oncogenic RAS activation, these fusion proteins bind to active RAS at the membrane and dimerize. This dimerization brings together complementary NarX variants, enabling transphosphorylation. The phosphorylated NarX then activates the humanized response regulator NarL, which binds to a synthetic promoter and drives expression of a chosen output gene. A second layer of specificity is introduced by placing circuit components (NarX, NarL) under the control of MAPK-responsive promoters. These transcriptional elements respond to sustained activation of downstream effectors in the RAS-MAPK pathway, such as ELK1, c-Fos, or SRF, ensuring that circuit activation requires not just the presence of RAS-GTP, but persistent oncogenic signaling. By combining these two inputs in an AND-gate configuration, the circuit discriminates sharply between mutant and wild-type RAS signaling, reducing off-target activity and achieving over 100-fold selectivity in mutant RAS contexts.

Synthetic Notch (synNotch) receptors are a modular platform that allows mammalian cells to programmably sense custom extracellular signals and trigger user-defined intracellular transcriptional responses[48,49]. By replacing both the extracellular recognition and intracellular transcriptional domains of the native Notch receptor, the authors created synthetic receptors that activate only upon specific cell-cell contact. These synNotch systems function across diverse cell types, including neurons and immune cells, and enable spatially precise control over processes like differentiation and epithelial-to-mesenchymal transition. Importantly, these synNotch receptors are orthogonal to each other. Multiple receptors can be expressed in the same cell without crosstalk, allowing for logic operations and signaling cascades.

Beyond the genetic level, circuits operating at the RNA level, particularly those involving miRNAs, also hold considerable promise, owing to the inherent programmability of RNA and the well-established role of endogenous miRNAs in disease. One example of RNA-level sensing is a synthetic “classifier” circuit that identifies HeLa cancer cells based on their endogenous microRNA expression patterns[50]. This system integrates multiple miRNA inputs and activates a therapeutic output only when the full input profile matches a pre-defined signature. Specifically, for miRNAs expected to be elevated, the circuit uses a double-inversion motif: the miRNA represses a repressor (LacI), thereby allowing output gene expression. For miRNAs expected to be low, complementary target sites in the output’s 3’ UTR ensure degradation in off-target cells. Together, these modules compute a logic function that tightly restricts actuation, such as expression of a pro-apoptotic gene, to the intended cancer cell type. This approach demonstrates how RNA-level circuits can classify complex cell states and trigger selective responses.

Finally, protein-level circuits remain the least explored, but they offer distinct advantages. Because they operate entirely in the post-translational space, they can respond to inputs on rapid timescales and interface directly with endogenous protein activities. Crucially, they avoid the need for exogenous DNA, reducing the risk of insertional mutagenesis and making them more compatible with transient or non-

integrating delivery strategies. As the field matures, such circuits may enable therapies that sense and directly act upon disease-relevant protein states in real time, bringing synthetic biology one step closer to mimicking the speed, specificity, and adaptability of natural cellular decision-making systems.

LOCKR (Latching Orthogonal Cage-Key protein Rationale) is an example of a protein-level sensing system that enables direct detection of endogenous signaling activity in living cells[51]. In this design, the sensing mechanism is entirely post-translational: a synthetic “cage” protein contains a “latch” domain embedded with a Ras-binding domain, which blocks interaction with a separate “key” protein under resting conditions. When Ras-GTP binds to the embedded RBD, it triggers a conformational change that opens the latch, allowing the key to bind the cage and reconstitute a split fluorescent or enzymatic readout. This architecture forms the basis of Ras-LOCKR-S, a FRET-based sensor that reports local Ras-GTP activity with high sensitivity and subcellular resolution. LOCKR systems thus demonstrate how de novo protein circuits can sense native molecular events with speed, tunability, and spatial precision unmatched by transcriptional approaches.

Rewiring of Aberrant Signaling to Effector Release (RASER) is another synthetic protein-level system. RASER detects hyperactive ErbB receptor activity and converts it into therapeutic responses[52]. The system is highly modular and programmable, enabling outputs such as apoptosis (through release of Bid protein) or CRISPR-based gene activation. Delivered by non-integrating viral vectors like AAV, RASER achieved selective ablation of ErbB-driven cancer cells *in vitro*. However, AAV is unlikely to be delivered to all cancer cells *in vivo*. To overcome these limitations, the system was recently updated to control replication of vesicular stomatitis virus (VSV), an RNA virus with strong cytotoxicity. In this new design, hyperactive ErbB signaling in cancer cells triggers protease-mediated release of an essential VSV replication protein, enabling selective viral propagation and tumor cell killing[53]. This engineered virus (HERV for hyperactive ErbB-restricted virotherapy) replicates only in phospho-ErbB positive cells, dramatically expanding within tumors while sparing normal tissue. In mouse models of

metastatic pancreatic and ovarian cancer, HERV extended survival and synergized with standard chemotherapy.

Together, these systems suggest that synthetic circuits could be a powerful way of detecting and treating disease. There are only a handful of papers in this area, which underscores how early the field still is and how many interesting directions remain unexplored. In this thesis, I will explore one implementation of synthetic circuits using engineered proteins to target Ras, the most common human oncogene. I will demonstrate principles for engineering such systems, share learnings along the way, and point to potential advantages these circuits may offer over traditional therapeutics.

CHAPTER 1 BIBLIOGRAPHY

1. Brown JS, Amend SR, Austin RH, Gatenby RA, Hammarlund EU, Pienta KJ. Updating the Definition of Cancer. *Mol Cancer Res.* 2023;21: 1142–1147. doi:10.1158/1541-7786.MCR-23-0411
2. Hanahan D, Weinberg RA. Hallmarks of cancer: the next generation. *Cell.* 2011;144: 646–674. doi:10.1016/j.cell.2011.02.013
3. Hanahan D, Weinberg RA. The hallmarks of cancer. *Cell.* 2000;100: 57–70. doi:10.1016/s0092-8674(00)81683-9
4. Hanahan D. Hallmarks of Cancer: New Dimensions. *Cancer Discov.* 2022;12: 31–46. doi:10.1158/2159-8290.CD-21-1059
5. Vaux DL. In defense of the somatic mutation theory of cancer. *Bioessays.* 2011;33: 341–343. doi:10.1002/bies.201100022
6. Eren K, Taktakoğlu N, Pirim I. DNA Sequencing Methods: From Past to Present. *Eurasian J Med.* 2022;54: 47–56. doi:10.5152/eurasianjmed.2022.22280
7. Kim S, Jeong S. Mutation Hotspots in the β -Catenin Gene: Lessons from the Human Cancer Genome Databases. *Mol Cells.* 2019;42: 8–16. doi:10.14348/molcells.2018.0436
8. Mateo J, Steuten L, Aftimos P, André F, Davies M, Garralda E, et al. Delivering precision oncology to patients with cancer. *Nat Med.* 2022;28: 658–665. doi:10.1038/s41591-022-01717-2
9. Wahida A, Buschhorn L, Fröhling S, Jost PJ, Schneeweiss A, Lichter P, et al. The coming decade in precision oncology: six riddles. *Nat Rev Cancer.* 2023;23: 43–54. doi:10.1038/s41568-022-00529-3
10. Okonechnikov K, Camgöz A, Chapman O, Wani S, Park DE, Hübner J-M, et al. 3D genome mapping identifies subgroup-specific chromosome conformations and tumor-dependency genes in ependymoma. *Nature Communications.* 2023;14: 1–16. doi:10.1038/s41467-023-38044-0
11. Martincorena I, Roshan A, Gerstung M, Ellis P, Van Loo P, McLaren S, et al. Tumor evolution. High burden and pervasive positive selection of somatic mutations in normal human skin. *Science.* 2015;348: 880–886. doi:10.1126/science.aaa6806

12. Shaffer SM, Dunagin MC, Torborg SR, Torre EA, Emert B, Krepler C, et al. Rare cell variability and drug-induced reprogramming as a mode of cancer drug resistance. *Nature*. 2017;546: 431–435. doi:10.1038/nature22794
13. Slamon DJ, Clark GM, Wong SG, Levin WJ, Ullrich A, McGuire WL. Human Breast Cancer: Correlation of Relapse and Survival with Amplification of the HER-2/neu Oncogene. *Science*. 1987 [cited 6 May 2025]. doi:10.1126/science.3798106
14. Hasanova A, Asadov C, Shirinova A, Aliyeva G, Alimirzoyeva Z. Role of genetic factors in imatinib resistance of chronic myeloid leukemia: P53, RB1, ASS1 gene deletions, and chromosome 8 hyperdiploidy. *Pathol Res Pract*. 2025;269: 155943. doi:10.1016/j.prp.2025.155943
15. Dhangar S, Shanmukhaiah C, Ghatanatti J, Sawant L, Maurya N, Vundinti BR. Comprehensive analysis of tyrosine kinase domain mutations and imatinib resistance in chronic myeloid leukemia patients. *Leuk Res*. 2025;152: 107679. doi:10.1016/j.leukres.2025.107679
16. Cavalleri A, Xhahysa B, Mutti S, Ferraro RM, Mazzoldi EL, Farina M, et al. Different In Vitro Models of Chronic Myeloid Leukemia Show Different Characteristics: Biological Replicates Are Not Biologically Equivalent. *Cell Biol Int*. 2025;49: 570–586. doi:10.1002/cbin.70007
17. Awad MM, Liu S, Rybkin II, Arbour KC, Dilly J, Zhu VW, et al. Acquired resistance to KRASG12C inhibition in cancer. *N Engl J Med*. 2021;384: 2382–2393. doi:10.1056/NEJMoa2105281
18. de Langen AJ, Johnson ML, Mazieres J, Dingemans A-MC, Mountzios G, Pless M, et al. Sotorasib versus docetaxel for previously treated non-small-cell lung cancer with KRASG12C mutation: a randomised, open-label, phase 3 trial. *Lancet*. 2023;401: 733–746. doi:10.1016/S0140-6736(23)00221-0
19. Liu J, Kang R, Tang D. The KRAS-G12C inhibitor: activity and resistance. *Cancer Gene Ther*. 2022;29: 875–878. doi:10.1038/s41417-021-00383-9
20. Holderfield M, Lee BJ, Jiang J, Tomlinson A, Seamon KJ, Mira A, et al. Concurrent inhibition of oncogenic and wild-type RAS-GTP for cancer therapy. *Nature*. 2024;629: 919–926. doi:10.1038/s41586-024-07205-6

21. Pao W, Chmielecki J. Rational, biologically based treatment of EGFR-mutant non-small-cell lung cancer. *Nat Rev Cancer*. 2010;10: 760–774. doi:10.1038/nrc2947
22. Koulouris A, Tsagkaris C, Corriero AC, Metro G, Mountzios G. Resistance to TKIs in EGFR-Mutated Non-Small Cell Lung Cancer: From Mechanisms to New Therapeutic Strategies. *Cancers (Basel)*. 2022;14. doi:10.3390/cancers14143337
23. Fu K, Xie F, Wang F, Fu L. Therapeutic strategies for EGFR-mutated non-small cell lung cancer patients with osimertinib resistance. *J Hematol Oncol*. 2022;15: 173. doi:10.1186/s13045-022-01391-4
24. Manzano JL, Layos L, Bugés C, de Los Llanos Gil M, Vila L, Martínez-Balibrea E, et al. Resistant mechanisms to BRAF inhibitors in melanoma. *Ann Transl Med*. 2016;4: 237. doi:10.21037/atm.2016.06.07
25. Bucheit AD, Davies MA. Emerging insights into resistance to BRAF inhibitors in melanoma. *Biochem Pharmacol*. 2014;87: 381–389. doi:10.1016/j.bcp.2013.11.013
26. DiMasi JA, Grabowski HG. Economics of new oncology drug development. *J Clin Oncol*. 2007;25: 209–216. doi:10.1200/JCO.2006.09.0803
27. Zhang SX, Fergusson D, Kimmelman J. Proportion of Patients in Phase I Oncology Trials Receiving Treatments That Are Ultimately Approved. *J Natl Cancer Inst*. 2020;112: 886–892. doi:10.1093/jnci/djaa044
28. D’Avella C, Abbosh P, Pal SK, Geynisman DM. Mutations in renal cell carcinoma. *Urol Oncol*. 2020;38: 763–773. doi:10.1016/j.urolonc.2018.10.027
29. Hsieh JJ, Purdue MP, Signoretti S, Swanton C, Albiges L, Schmidinger M, et al. Renal cell carcinoma. *Nat Rev Dis Primers*. 2017;3: 17009. doi:10.1038/nrdp.2017.9
30. Zhou Z, Wu S, Lai J, Shi Y, Qiu C, Chen Z, et al. Identification of trunk mutations in gastric carcinoma: a case study. *BMC Medical Genomics*. 2017;10: 1–8. doi:10.1186/s12920-017-0285-y
31. Trunk mutational events present minimal intra- and inter-tumoral heterogeneity in hepatocellular carcinoma. *Journal of Hepatology*. 2017;67: 1222–1231. doi:10.1016/j.jhep.2017.08.013

32. Yang L, Li N, Wang M, Zhang Y-H, Yan L-D, Zhou W, et al. Tumorigenic effect of and its potential therapeutic target in NSCLC (Review). *Oncol Rep.* 2021;46. doi:10.3892/or.2021.8133
33. Dratwa M, Wysoczańska B, Łacina P, Kubik T, Bogunia-Kubik K. TERT-Regulation and Roles in Cancer Formation. *Front Immunol.* 2020;11: 589929. doi:10.3389/fimmu.2020.589929
34. Reyes-Uribe P, Adrianzen-Ruesta MP, Deng Z, Echevarria-Vargas I, Mender I, Saheb S, et al. Exploiting TERT dependency as a therapeutic strategy for NRAS-mutant melanoma. *Oncogene.* 2018;37: 4058–4072. doi:10.1038/s41388-018-0247-7
35. AmeliMojarad M, AmeliMojarad M, Cui X, Shariati P. Pan-cancer analysis of CTNNB1 with potential as a therapeutic target for human tumorigenesis. *Inform Med Unlocked.* 2023;42: 101331. doi:10.1016/j.imu.2023.101331
36. Zaman GJR, de Roos JADM, Libouban MAA, Prinsen MBW, de Man J, Buijsman RC, et al. TTK Inhibitors as a Targeted Therapy for (-catenin) Mutant Cancers. *Mol Cancer Ther.* 2017;16: 2609–2617. doi:10.1158/1535-7163.MCT-17-0342
37. van Schie EH, van Amerongen R. Aberrant WNT/CTNNB1 Signaling as a Therapeutic Target in Human Breast Cancer: Weighing the Evidence. *Front Cell Dev Biol.* 2020;8: 25. doi:10.3389/fcell.2020.00025
38. Lane DP. Cancer. p53, guardian of the genome. *Nature.* 1992;358: 15–16. doi:10.1038/358015a0
39. Feroz W, Sheikh AMA. Exploring the multiple roles of guardian of the genome: P53. *Egypt J Med Hum Genet.* 2020;21: 1–23. doi:10.1186/s43042-020-00089-x
40. Sigal A, Rotter V. Oncogenic mutations of the p53 tumor suppressor: the demons of the guardian of the genome. *Cancer Res.* 2000;60: 6788–6793. Available: <https://www.ncbi.nlm.nih.gov/pubmed/11156366>
41. Zambetti GP. *The p53 Tumor Suppressor Pathway and Cancer.* Springer Science & Business Media; 2007. Available: <https://play.google.com/store/books/details?id=CrLoAfnJsIwC>
42. Hainaut P, Wiman KG. *25 Years of p53 Research.* Springer Science & Business Media; 2007. Available: <https://play.google.com/store/books/details?id=tH4te5w-3BUC>

43. Haupt Y, Blandino G. Human Tumor-Derived p53 Mutants: A Growing Family of Oncoproteins. Frontiers Media SA; 2016. Available:
https://books.google.com/books/about/Human_Tumor_Derived_p53_Mutants_A_Growin.html?hl=&id=qEMxDwAAQBAJ
44. Melillo G. Hypoxia and Cancer: Biological Implications and Therapeutic Opportunities. Springer Science & Business Media; 2013. Available:
<https://play.google.com/store/books/details?id=iRIJAgAAQBAJ>
45. Lozano G, Levine AJ. The P53 Protein: From Cell Regulation to Cancer. 2016. Available:
https://books.google.com/books/about/The_P53_Protein.html?hl=&id=oNmXjgEACAAJ
46. Liu Y, Su Z, Tavana O, Gu W. Understanding the complexity of p53 in a new era of tumor suppression. *Cancer Cell*. 2024;42: 946–967. doi:10.1016/j.ccell.2024.04.009
47. Senn G, Nissen L, Benenson Y. Synthetic gene circuits that selectively target RAS-driven cancers. *bioRxiv*. 2024. doi:10.1101/2024.11.11.622942
48. Morsut L, Roybal KT, Xiong X, Gordley RM, Coyle SM, Thomson M, et al. Engineering Customized Cell Sensing and Response Behaviors Using Synthetic Notch Receptors. *Cell*. 2016;164: 780–791. doi:10.1016/j.cell.2016.01.012
49. Ruffo E, Butchy AA, Tivon Y, So V, Kvorjak M, Parikh A, et al. Post-translational covalent assembly of CAR and synNotch receptors for programmable antigen targeting. *Nat Commun*. 2023;14: 2463. doi:10.1038/s41467-023-37863-5
50. Xie Z, Wroblewska L, Prochazka L, Weiss R, Benenson Y. Multi-input RNAi-based logic circuit for identification of specific cancer cells. *Science*. 2011;333: 1307–1311. doi:10.1126/science.1205527
51. Zhang JZ, Nguyen WH, Greenwood N, Rose JC, Ong S-E, Maly DJ, et al. Computationally designed sensors detect endogenous Ras activity and signaling effectors at subcellular resolution. *Nat Biotechnol*. 2024. doi:10.1038/s41587-023-02107-w
52. Chung HK, Zou X, Bajar BT, Brand VR, Huo Y, Alcludia JF, et al. A compact synthetic pathway rewires cancer signaling to therapeutic effector release. *Science (New York, NY)*. 2019;364: eaat6982. doi:10.1126/science.aat6982

53. Zou X, Zhao C, Beier KT, Kang C-Y, Lin MZ. Rewiring oncogenic signaling to RNA vector replication for the treatment of metastatic cancer. bioRxivorg. 2025.
doi:10.1101/2024.12.30.630713

Chapter 2

DESIGN OF SYNTHETIC MUTANT RAS SENSORS

2.1 Summary

The fundamental challenge of cancer therapy is to specifically eliminate cancer cells while sparing healthy tissue. Targeted therapies represent a breakthrough towards this goal. However, their long-term efficacy is limited by resistance, which often occurs because targeted therapies do not kill cancer cells directly. Instead, they partially block the oncogenic signals that tumors use to drive uncontrolled growth, leaving many escape routes that allow tumors to adapt and develop resistance.

Engineered protein circuits have been envisioned as an alternative to targeted therapies. Rather than block oncogenic signals, circuits use engineered proteins to directly link oncogenic signals to cell death, potentially circumventing the resistance mechanisms that limit targeted therapies.

In the following chapters, I demonstrate proof-of-concept for engineered protein circuits by targeting the oncogene Ras, which drives roughly one in four human cancers. The engineered protein circuits are composed of a protease-based sensor that responds to a broad spectrum of clinically relevant Ras mutations and a protease-activatable cell death effector. The effector can trigger either non-inflammatory apoptosis or immunogenic pyroptosis, which has been shown to extend therapeutic effects beyond transfected cells. Delivered as mRNA in lipid nanoparticles (LNPs), circuits accurately discriminated between Ras-mutant cancer and non-cancer cells, potently eliminated cells resistant to the state-of-the-art Ras-targeting drugs Sotorasib and RMC-7977 *in vitro*, and cleared induced aggressive, multifocal liver tumors in mice.

In this chapter, I will start by describing the engineering process of the Ras sensor, and conclude with learnings from the process.

2.2 Introduction

Therapeutic circuits comprise sets of engineered proteins that can be expressed in cells to sense disease-specific signals and conditionally trigger cell death or other responses (**Fig. 2.1**). In the context of cancer, they have the potential to offer higher efficacy and less opportunity for resistance than targeted therapies [1,2], greater molecular specificity than chemotherapies [3,4], and an expanded ability to sense intracellular proteins compared to CAR-T cells [5,6] and antibody-drug conjugates [7,8]. While aspects of the therapeutic circuit paradigm have been explored [2,9–21], fundamental questions have remained: Can engineered proteins sensitively and specifically detect mutant oncogenes in cancer cells? Can therapeutic circuits treat tumors *in vivo*? And, how do therapeutic circuits compare to targeted small molecule drugs in terms of treatment efficacy and resistance?

Here, we describe the design, optimization, and characterization of protease-based therapeutic circuits that selectively kill Ras-mutant cancer cells. Proteases represent ideal building blocks for therapeutic circuits. They are modular, engineerable and can directly interface with endogenous pathways [22–24]. Previous work from the Elowitz lab demonstrated a synthetic protein circuit platform (CHOMP: Circuits of Hacked Orthogonal Modular Proteases) in human cells in which multiple engineered plant viral proteases function as composable circuit components that can regulate one another[9,14]. This system enables construction of diverse protein-level functions from a limited number of components. In particular, they showed that split proteases can be conditionally reconstituted with protein-protein interactions as a powerful platform for classifying disease at the protein level. Work from other labs have similarly exploited the combination of modular protein domains to achieve related functions[14].

Using the CHOMP system as a foundation, we engineer a set of synthetic protein circuits to sense the oncogene Ras. We target Ras because Ras mutations drive roughly one in four human cancers, yet durable and effective Ras-targeting therapies remain limited [23,25,26].

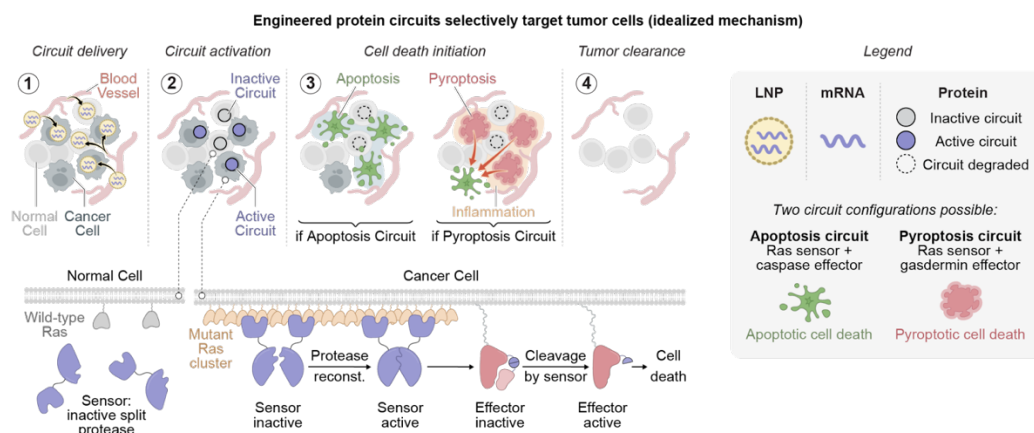


Fig. 2.1. Engineered protein circuits selectively target cancer cells (schematic).

This schematic illustration represents idealized therapeutic circuit behavior. (1) Therapeutic circuits composed of sensor and effector modules can be delivered to cells as mRNA in lipid nanoparticles (LNPs). (2) Sensors activate selectively upon binding mutant Ras clusters. More specifically, Ras clustering co-recruits complementary split protease sensor halves to the cell membrane, leading to protease reconstitution (lower panel). (3) Active sensors trigger cell-death effectors and initiate apoptotic (left) or pyroptotic (right) cell death in Ras-mutant cells. Pyroptosis could further stimulate the immune system to kill non-transfected cells (arrows). (4) Circuits eliminate Ras-driven tumors without harming healthy tissue.

2.3 Results

2.3.1 Engineered sensors specifically respond to diverse Ras mutations

An ideal Ras sensor should strongly activate to diverse oncogenic Ras mutants, but not to wild-type Ras. A previous sensing mechanism used Ras binding domains attached to complementary halves of a split Tobacco Etch Virus (TEV) protease [10,12]. Ras activation could then recruit split sensor proteins to Ras clusters, leading to protease reconstitution (**Fig. 2.1**). In its initial design (*v1*), the sensor used the natural Ras-binding

domain of RAF1. Despite responding to overexpressed Ras in HEK293 cells, this *vI* sensor poorly discriminated mutant and wild-type Ras variants, due to limited specificity and undesired sensor multimerization (**Fig. S2.1**).

We hypothesized that more specific and higher-affinity Ras binding domains could improve sensor function. To identify domains that would enable broad-spectrum mutant Ras sensing, we constructed a comprehensive library of human, *de novo* designed, and synthetic Ras binders. Specifically, we compiled a set of candidate human Ras binders by selecting proteins known to associate with KRAS, co-folding them with KRAS using AlphaFold3, and filtering for domains with high-confidence KRAS binding interfaces (**Methods**). We also used RFdiffusion to design sensor variants that incorporate *de novo* Ras binders (**Methods**). Finally, we incorporated previously described Ras-binding monobodies [27], designed ankyrin repeat proteins (DARPs) [28,29], synthetic proteins [30], and nanobodies [31]. To screen this library, each of these Ras binding domains was fused with complementary split TEVP domains and co-expressed with a panel of Ras variants as well as a fluorescent protease reporter in HEK293 cells [32] (**Fig. 2.2, Methods**). The reporter used a cleavage-activated IFP to measure protease activity and a GFP to track reporter expression, with the IFP/GFP ratio serving as normalized reporter readout. In the assay, additional fluorescent proteins were co-transfected to enable quantitative flow cytometry scanning of a broad, multi-dimensional expression space for each Ras mutant and candidate sensor (**Fig 2.2, Fig S2.2**).

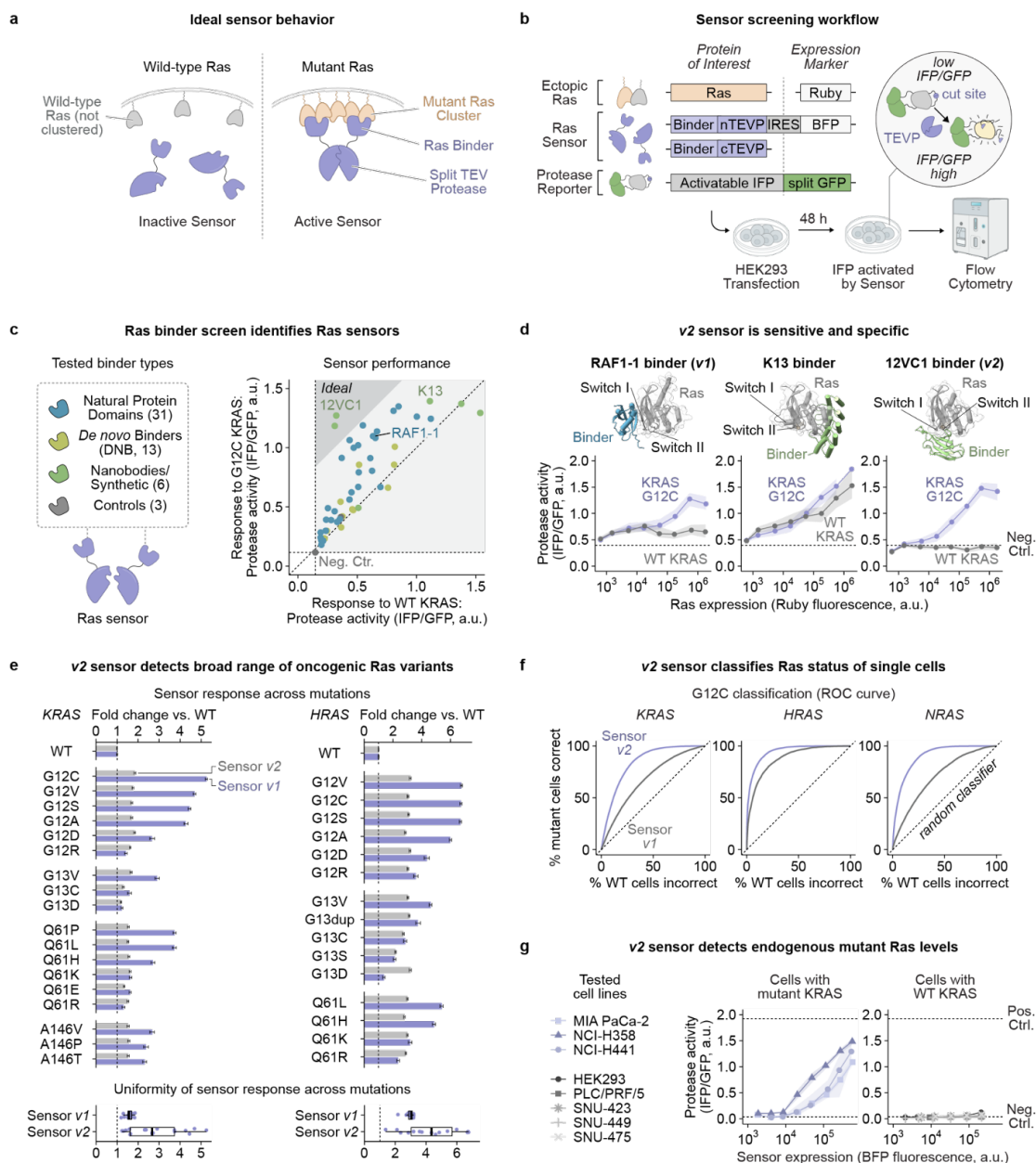


Fig. 2.2. Engineered sensors specifically respond to mutant Ras. (A) An ideal sensor should reconstitute a split protease effector in response to mutant but not wild-type Ras. **(B)** To screen for sensitive and specific Ras sensors, HEK293 cells were transiently transfected with ectopic Ras variants (marked by mRuby3), candidate sensors (marked by mTagBFP2, labeled BFP), and a protease-activatable fluorescent reporter (IFP/GFP

ratio denotes reporter activation). This setup enabled quantitative analysis of sensor performance across a multi-dimensional space of sensor and Ras expression levels. **(C)** The responses of candidate Ras sensors were characterized against mutant (KRAS^{G12C}) and wild-type Ras (KRAS^{WT}). Data points represent median reporter activation in high Ras expression regimes (**Methods**). Sensors are color-coded by the type of Ras binding domain (legend). Horizontal and vertical dotted lines denote reporter activation in the absence of a sensor (negative control). **(D)** Sensor *v2* (12VC1-based) maintains high sensitivity to mutant Ras across a broad range of ectopic Ras expression levels, with minimal background activation in wild-type Ras-expressing cells. Data points represent median reporter activation (**Methods**). Negative control line represents the activity of a sensor containing GSGSGS peptides as binders. Structures depict binders in complex with KRAS (RAF1-1: structure generated by AlphaFold3, K13: structure from PDB entry 6H46 [28], 12VC1: structure from PDB entry 7L0G [31]). **(E)** *Top*: *v2* (purple) exhibits enhanced sensitivity to a wide range of oncogenic KRAS (left) and HRAS (right) mutations compared to *v1* (gray). Bars show the fold-change sensor activation in response to mutant relative to wild-type Ras after gating for high Ras expression (**Methods**). *Bottom*: *v1* exhibited more uniform response to diverse Ras mutations compared to *v2*. Data points correspond to the fold-change sensor activation to mutant relative to wild-type Ras. Boxplots show median (center line), quartiles (box), and 1.5x interquartile range (line). Dotted line corresponds to equal responses to mutant and wild-type Ras. **(F)** At the single-cell level, the *v2* sensor discriminated between mutant and wild-type Ras-expressing cells. Receiver operating characteristic (ROC) analysis was performed by varying the protease reporter threshold, generating a confusion matrix, and plotting the true positive rate (Ras-mutant cells above reporter threshold) against the false positive rate (wild-type Ras cells above reporter threshold) at matched Ras expression levels. Dotted line represents the performance of a random classifier. **(G)** *v2* sensor detects endogenous mutant Ras levels. Sensors and fluorescent protease reporter were transiently transfected into cancer cell lines with endogenous levels of Ras and analyzed by flow cytometry. The human cancer cell lines MIA PaCa-2 (KRAS^{G12C}),

NCI-H358 (KRAS^{G12C}), and NCI-H441 (KRAS^{G12V}) express mutant Ras, while HEK293, PLC/PRF/5, SNU-423, SNU-449, and SNU-475 express wild-type KRAS. Negative control line represents the activity of a sensor containing GSGSGS peptides as binders. Positive control line represents a sensor containing the P3/P4 coiled-coiled domains as binders. Error bars and shaded error regions in panels **D**, **E**, and **G** were computed as bootstrap 95% confidence intervals of the median (**Methods**). (**C** to **F**) Computed in cells with intermediate sensor expression levels.

Candidate sensors varied in their responses to mutant (KRAS^{G12C}) and wild-type (KRAS^{WT}) Ras. Among the *de novo* designed binders, a small subset exhibited weak discrimination of mutant over wild-type Ras, providing a basis for potential further optimization (**fig. S2.3**). Sensors based on the synthetic monobody NS1 or the DARPins K13 and K19 were strongly Ras-responsive but did not discriminate between wild-type and mutant Ras variants (**Fig. 2.2C-D**). By contrast, sensors based on the previously described 12VC synthetic monobody (12VC1 and 12VC3) achieved sensitive and specific discrimination of mutant and wild-type Ras (**Fig. 2.2C-D**). This likely reflects the monobody selection process, which combined positive selection for KRAS^{G12C} binding with negative-selection against wild-type KRAS. Further, the 12VC1 sensor, henceforth referred to as *v2*, exhibited a sensor expression-dependent response across a broad range of Ras expression levels (**Fig. 2.2D**, **fig. S2.4**).

The *v2* sensor detected a broad spectrum of clinically relevant oncogenic Ras variants. Following a similar experimental procedure as described above (**Methods**), we analyzed the response of *v2* to a panel of 46 prevalent KRAS, HRAS, and NRAS mutations from the TCGA database [33,34]. At matched Ras expression levels, the *v2* sensor strongly responded to most KRAS, HRAS, and NRAS mutants (**Fig. 2.2E**, **fig. S2.4A**). The prevalent G12 mutations G12C, G12V, G12S, and G12A induced strong responses (**Fig. 2.2E**). Notably, the *v2* sensor produced sufficient discrimination of wild-type and mutant

Ras-expressing cells to enable accurate classification at the single-cell level (**Fig. 2.2F**, **fig. S2.4C**).

To evaluate *v2* sensor activity at physiologic Ras expression levels, we transfected human cancer cell lines with the sensor and a protease reporter. The sensor strongly responded in cell lines with mutant Ras, including MIA PaCa-2 (KRAS^{G12C}), NCI-H358 (KRAS^{G12C}), and NCI-H441 (KRAS^{G12V}; **Fig. 2.2G**). By contrast, it showed minimal response in cancer cell lines with wild-type Ras, including PLC/PRF/5, SNU-423, SNU-449, SNU-475. Taken together, these results indicate that the *v2* sensor can sensitively and specifically respond to diverse, clinically-relevant Ras mutants expressed at endogenous levels in human cells.

2.3.2 Learnings from engineering sensor

In our screen, we tested three categories of Ras binding domains: natural Ras binding domains, *de novo* designed Ras binders, and synthetic binding proteins such as monobodies. Here, I will discuss some of our learnings from the engineering process, beyond what we did to get the sensor to work as intended. *Are there principles or heuristics that could be generalized in the future?*

Among natural Ras-binding domains, we observed a wide distribution of Ras binding activities, both toward wildtype and mutant Ras. This variability makes sense, as different natural Ras interacting proteins have different biological contexts, constraints, and evolutionary pressures that shape their interactions with Ras. But in general, natural Ras binding domains certainly were more sensitive to mutant than wild-type Ras. This finding also makes sense, since activating Ras mutations evolved precisely because they enhance downstream signaling and proliferative advantage.

But then why are natural Ras binding domains not the highest scoring category in our screen? Well, natural Ras-binding proteins (such as RAF or PI3K) evolved under constraints presumably unrelated to mutant selectivity. Additionally, these domains utilize flexible loops or shallow binding surfaces that can accommodate multiple Ras

isoforms. Indeed, natural binding domains aren't usually the absolute strongest binders, much like most natural enzymes aren't the fastest possible catalysts. As we know, evolutionary fitness is not just about maximizing every single property. Further, these natural binding domains are “modules” of larger proteins. Their evolutionary pressures extend beyond simply high-affinity binding, as they must also induce specific conformational changes necessary to propagate downstream signaling cascades. For instance, RAF binding to Ras not only stabilizes the complex, but also must induce conformational shifts in RAF itself, triggering kinase activation and downstream signaling. Thus, natural Ras-binding domains represent solutions to a multi-objective evolutionary optimization, balancing affinity, specificity, and downstream signaling properties.

On the other hand, *de novo* designed binders were generally less sensitive and specific than the other two binder categories. Granted, we tested only a small number of these binders, but I think the general pattern should hold and perhaps reveals a helpful heuristic. Specifically, when confronted with a new binder or enzyme-design problem, one could consider whether a natural counterpart already exists. If a natural protein domain has evolved to carry out the task reasonably well, it is likely more efficient to start engineering efforts from there, as evolution has presumably already somehow traversed the complex fitness landscape. However, when the desired behavior is completely novel, lacking known natural analogs or evolutionary templates, then *de novo* design methods offer a powerful and increasingly effective alternative, precisely because they can explore structural solutions that natural evolution has never encountered.

Finally, synthetic binding domains were, in general, the most sensitive and most specific category of Ras-binding proteins in our screen. This result is perhaps not surprising, given that library-based methods typically begin with extremely large diversities (often 10^9 to 10^{11} variants) and are subjected to relatively simple selection pressures such as binding affinity. Synthetic screening methods thus enable convergence on solutions that are purely optimized for binding, unconstrained by the multifunctional or regulatory demands that shape natural protein evolution. Here, I will take some time to discuss the

top-performing Ras binder from our screen, the monobody 12VC1, and highlight some structural and conceptual lessons from its design.

12VC1 is a monobody specific to Ras G12C and G12V. Monobodies are a class of synthetic binding proteins that adopt a β -sandwich fold, composed of two antiparallel β -sheets. This structure creates distinct surfaces: the top or tip region formed by three surface-exposed loops (resembling “fingers” sticking up), and the sides formed by the β -sheet faces themselves (resembling the “palm”).

Traditional monobody libraries typically mutate the tip loops (the “fingers”), mimicking the way antibodies achieve specificity via their complementarity-determining regions (CDR). These loops typically insert into clefts or pockets on the target protein. However, this approach inherently restricts what kind of specificity can be achieved by binding, since it favors targets with concave or pocketed surfaces and limits access to flat or convex targets (imagine trying to grip a basketball using only your fingertips).

In contrast, side-and-loop monobody libraries diversify not just the loops, but also selected residues along one β -sheet face (the “palm”). This larger and continuous interface can thus offer several structural advantages: increased overall surface area at the interface for better affinity and specificity, and expanded range of target protein surfaces. Using positive selection for KRAS G12C and negative selection against wild-type KRAS, this side-and-loop monobody library yielded 12VC1. Structural analysis revealed an extensive and shape-matched interface between 12VC1 and KRAS G12C, explaining the exquisite specificity for mutant Ras. Together, this suggests that rationally combining rigid scaffold elements with deliberate, structural surface complementarity significantly expands the possibilities of binding interactions, surpassing even nature’s optimized protein domains

2.4 Supplementary Figures

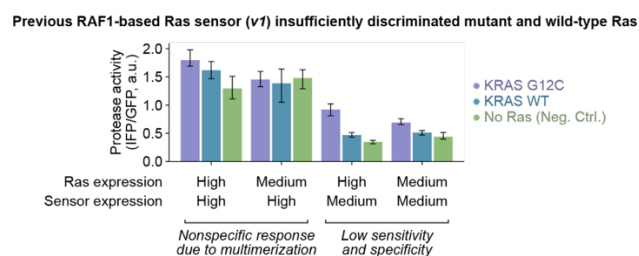


Fig. S2.1. Previous RAF1-based Ras sensor (v1) insufficiently discriminated mutant and wild-type Ras. When highly expressed (co-transfected mTagBFP2 between 10^5 - 10^6 a.u.), the v1 sensor activates in a non-specific fashion due to sensor multimerization. In a medium sensor expression regime (co-transfected mTagBFP2 between 10^4 - 10^5 a.u.), the v1 sensor shows low sensitivity and specificity. Sensor performance was evaluated following the experimental workflow outlined in **Fig. 2B**. High Ras expression corresponds to mRuby3 fluorescence (co-transfected with ectopic Ras) of $10^{5.5}$ - $10^{6.5}$ a.u.; medium Ras expression to $10^{4.5}$ - $10^{5.5}$ a.u. Bar plots represent median sensor protease activities; error bars denote 95% confidence intervals calculated by bootstrapping (1,000 iterations).

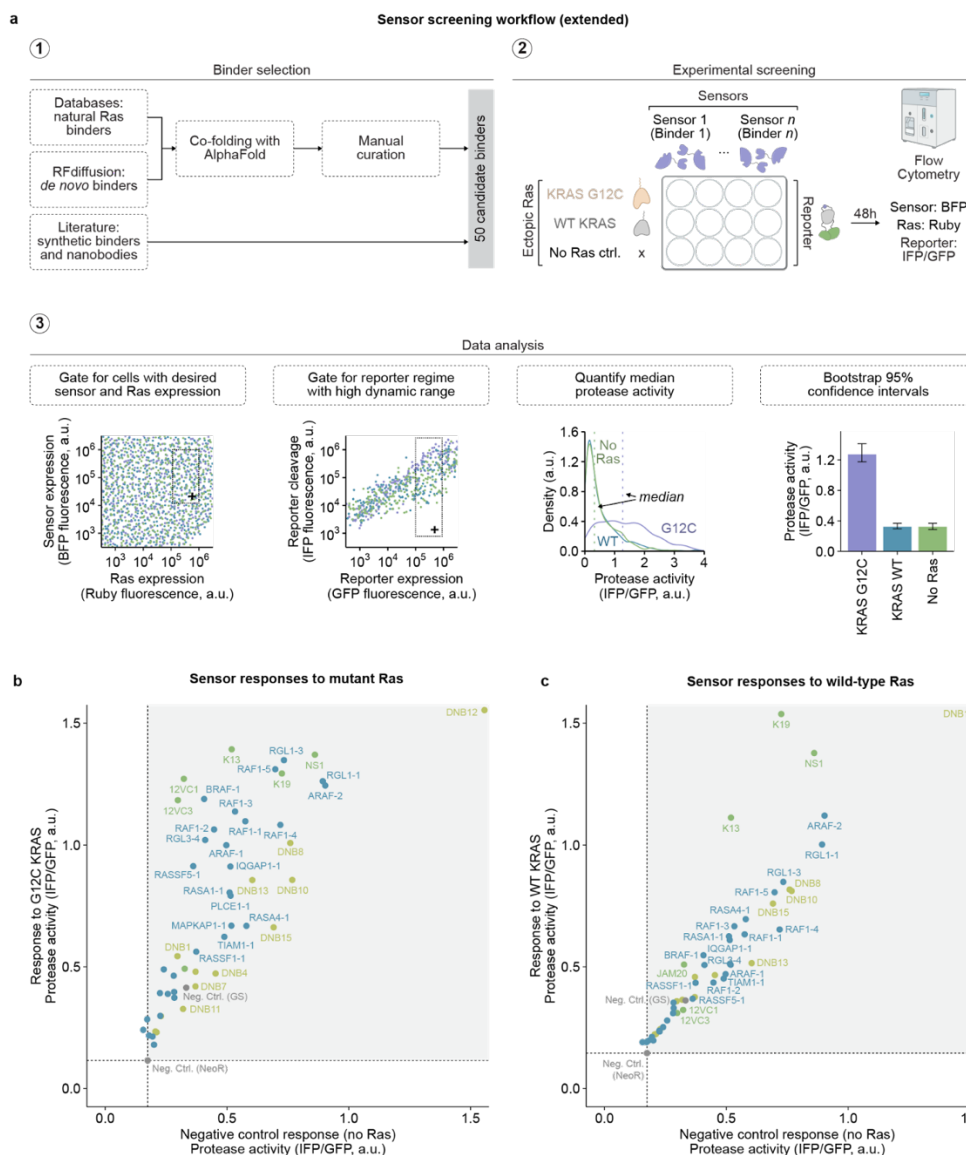


Fig. S2.2. Ras binder screen identifies Ras-mutant-specific sensors. (A) Workflow used for sensor screening and quantitative analysis of flow cytometry data. After generation of binder library and experimental screening by flow cytometry, sensor activation was determined as follows: cells that received the sensor (as marked by mTagBFP2 fluorescence between 10^4 - 10^6 a.u.; in the following referred to as median sensor expression) and expressed high levels of ectopic Ras (as marked by mRuby3

fluorescence between 10^5 - 10^6 a.u.) were selected. Further, we gated for cells with protease reporter expression between 10^5 - 10^6 a.u. (as marked by reporter GFP fluorescence), corresponding to the regime with the highest reporter dynamic range. Finally, median protease activity was calculated as the fraction of activated protease reporter proteins (IFP/GFP). Confidence estimates were obtained by bootstrapping.

(B) Library screen enables characterization of sensor activity against mutant KRAS^{G12C} compared to a no Ras control. Data points represent median reporter activation in high Ras and medium sensor expression regime. Sensors are color-coded by the category of Ras binding domain. Text denotes binding domain used for each sensor. Negative control line denotes reporter activation in the absence of a sensor.

(C) Library screen enables characterization of sensor activity against wild-type KRAS compared to a no Ras control. Data points represent median reporter activation in high Ras and medium sensor expression regime. Sensors are color-coded by the category of Ras binding domain. Text denotes binding domain used for each sensor. Negative control line denotes reporter activation in the absence of a sensor.

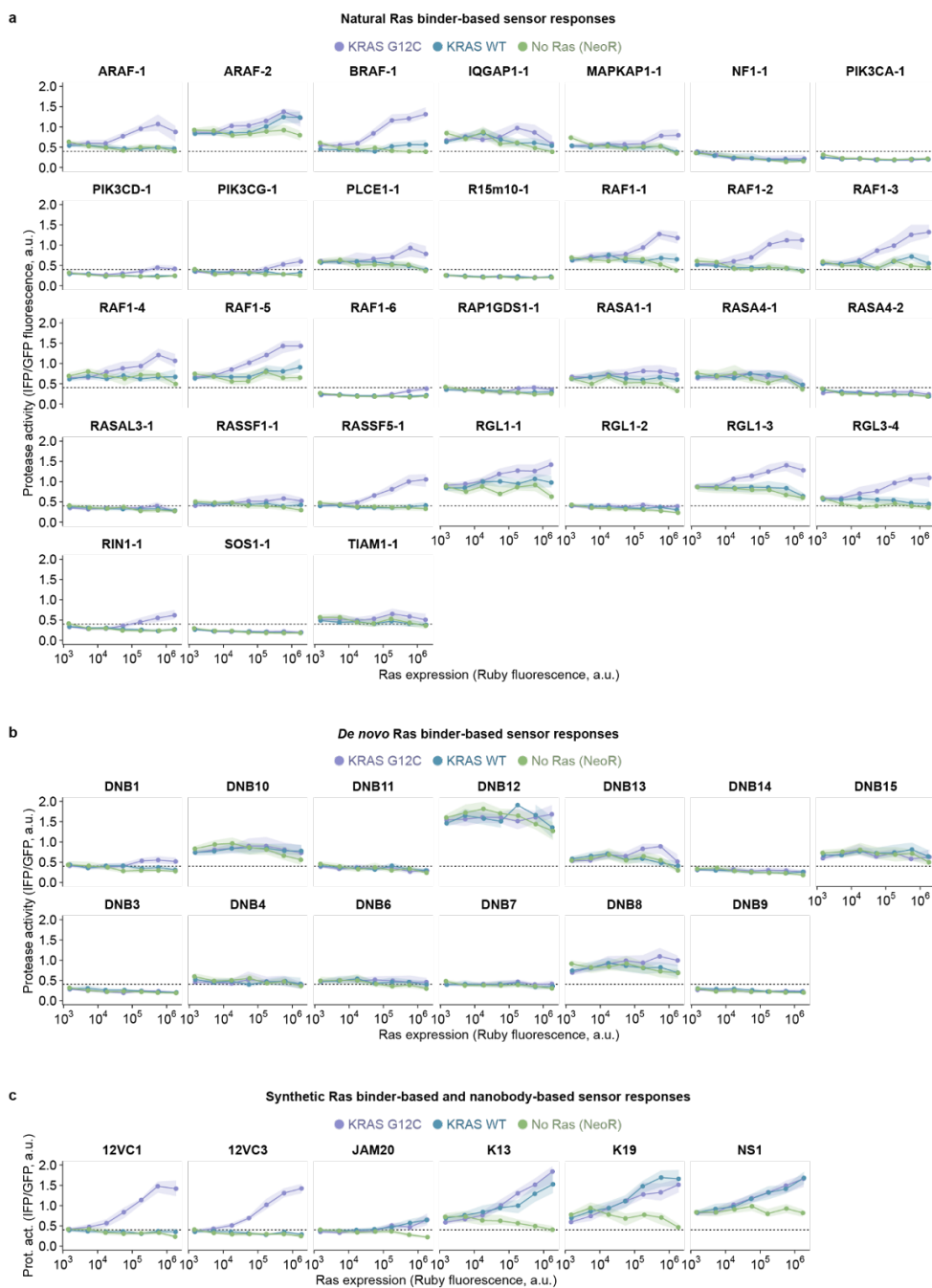


Fig. S2.3. Ras expression dependency of individual sensor responses. (A) Sensor responses of natural Ras binder-based sensors. **(B)** Responses of sensors incorporating *de novo* Ras binders (DNB). **(C)** Responses of sensors utilizing

previously published synthetic Ras binders, nanobodies, or monobodies. (A-C) Headings specify binding domains used for each sensor module. Data points represent median reporter activation in medium sensor expression regime. Negative control line represents the activity of a sensor containing GSGSGS peptides as binders. Shaded areas depict 95% confidence intervals from bootstrapping (1,000 iterations).

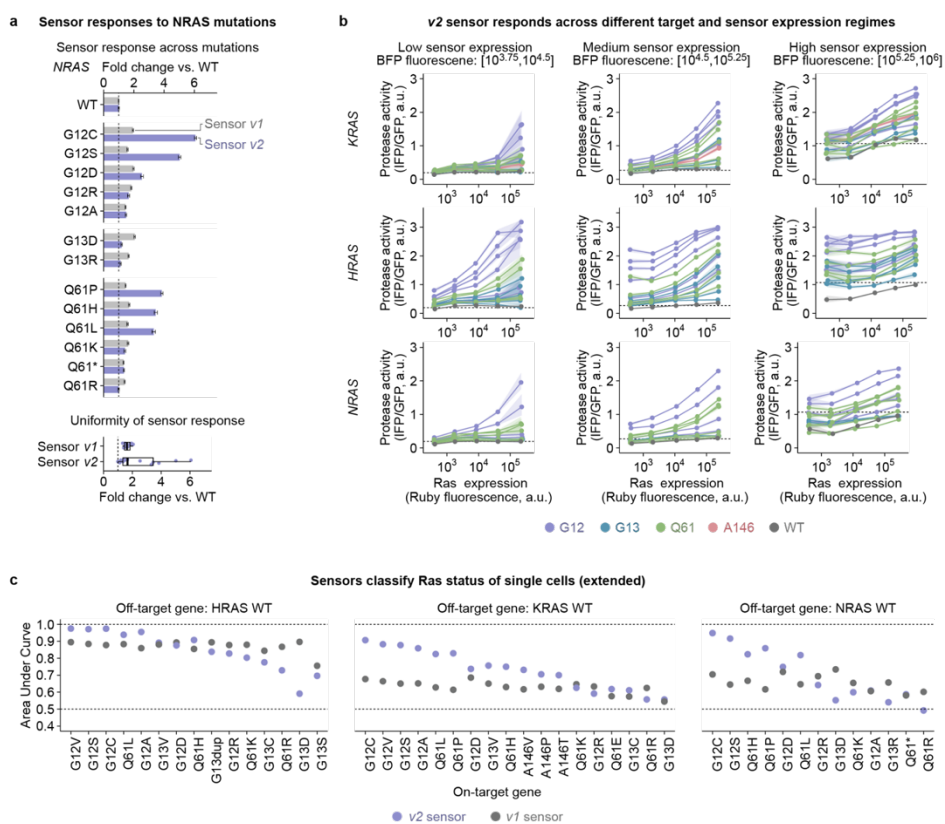


Fig. S2.4. Characterization of Ras sensors v1 and v2. (A) Comparison of sensor v1 and v2 responses across a broad spectrum of NRAS oncogenic mutations. *Top*: Bars show the fold-change sensor activation in response to mutant relative to wild-type Ras after gating for high Ras and intermediate sensor

expression. *Bottom*: *v1* exhibited more uniform response to diverse Ras mutations compared to *v2*. Data points correspond to the fold-change sensor activation to mutant relative to wild-type Ras. Boxplots show median (center line), quartiles (box), and 1.5x interquartile range (line). Dotted line corresponds to equal responses to mutant and wild-type Ras. **(B)** Sensor *v2* is sensitive to a range of KRAS, HRAS, and NRAS oncogenic mutations at different sensor and Ras expression levels. Data points represent median reporter activation. Negative control line represents the activity of a sensor containing GSGSGS peptides as binders. Shaded areas depict 95% confidence intervals from bootstrapping (1,000 iterations). **(C)** Sensors can classify the Ras mutational status of single cells. Area under curve values are obtained by ROC analysis (**Methods**).

2.5 Methods

Plasmid construction

Plasmids were generated via Gibson Assembly (NEBuilder HiFi DNA Assembly Master Mix; New England BioLabs) or KLD cloning (T4 Polynucleotide Kinase, T4 DNA Ligase, DpnI, T4 DNA Ligase Buffer; Thermo Scientific). Gene fragments were sourced from Twist Bioscience or Integrated DNA Technologies (IDT), or PCR-amplified from existing laboratory plasmid constructs. IDT synthesized all PCR primers. Plasmids were purified (QIAprep Spin Miniprep Kit or Qiacube machine; Qiagen), normalized (Thermo Scientific NanoDrop 8000), and sequence-verified (Plasmidsaurus or Genewiz) prior to experimental use.

Tissue culture and cell lines

Most cell lines were obtained from ATCC and cultured under standard conditions (37°C, 5% CO₂, humidified Eppendorf CellXpert C170i incubator). Adherent cells were maintained in Dulbecco's Modified Eagle Media (DMEM; Thermo Fisher) supplemented with 10% fetal bovine serum (FBS; Avantor), penicillin (1 unit/ml), streptomycin (1

µg/ml), glutamine (2 mM), sodium pyruvate (1 mM), and 1X Minimal Essential Media Non-Essential Amino Acids (all Thermo Fisher). HEK293FT cells were cultured for up to 20 passages, and human cancer cell lines for up to 15 passages, maintaining 10%-90% confluency. Cells were passaged using 0.25% Trypsin-EDTA (Thermo Fisher). Viable cell numbers for seeding densities were determined using Trypan Blue (Invitrogen) and the Countess 3 automated cell counter (Thermo Fisher). Cells were routinely confirmed mycoplasma-free (MycoStrip kit; InvivoGen). Cell lines with stably integrated fluorescent proteins used for microscopy were purchased from FenicsBIO.

Transient transfection

Transient transfections were performed utilizing FuGENE HD (Promega), Lipofectamine 3000 (Thermo Fisher), or LNPs (described below) as transfection agents. Unless otherwise noted, we seeded 10k cells (96-well plate), 200k cells (24-well plate) for FuGENE or LNP transfections, and 275k cells (24-well plate) for Lipofectamine transfections. Cells were reverse-transfected immediately after seeding following manufacturer instructions. For FuGENE transfections, we incubated 1 µg plasmid DNA with 6 µl transfection reagent. For FuGENE transfections, 200k cells were transfected with up to 566 ng of DNA. For Lipofectamine transfections, 1.5 µl Lipofectamine 3000 and 1.5 µl reagent P3000 were used with a total of 500 ng DNA to transfect an equivalent of 275k cells. The total amount of plasmid DNA applied in each transfection was scaled according to seeding densities.

Flow cytometry

Cells were collected two days post-transient transfection for flow cytometry, filtered through a 40-µm cell strainer, and analyzed by flow cytometry (CytoFLEX S flow cytometer, Beckman Coulter). Unless otherwise noted, we used FITC-A channel (GFP of iTEVP reporter[32]; excitation 488 nm, emission 525/40 nm; gain of 1), ECD-A channel (mRuby3; excitation 561 nm, emission 610/20 nm; gain of 1), PB450-A channel (mTagBFP2; excitation 405 nm, emission 450/45 nm; gain of 1), and APC-A700-A channel (IFP of iTEVP reporter; excitation 638 nm, emission 712/25; gain of 100). Live cells and singlets were gated using FlowJo (version 10.10, BD Biosciences). iTEVP reporter activation was assessed by calculating the IFP (activation) to GFP (reporter

expression) ratio for cells with GFP expression between 10^5 and 10^6 a.u., corresponding to the reporter expression regime with maximal dynamic range. As the reporter construct was always transfected as a separate polytransfection mix, selecting cells with high reporter expression did not bias subsequent analysis steps, *i.e.*, the expression distribution of other constructs (*e.g.*, reporter or ectopic Ras) remained unaffected.

Computational identification of Ras binding domains

To identify candidate Ras binding domains, we first extracted human proteins known to physically associate with KRAS from the STRING database [35] (physical subnetwork, medium confidence). All proteins passing these filters were co-folded with wild-type KRAS-4B and GTP using AlphaFold3 (AlphaFold Server) [36]. Binders predicted to interact with the CAAX domain of KRAS-4B were manually removed. To identify candidate binders for experimental characterization, we filtered for binders with high-confidence Ras interactions (interface PAE score < 10 and interface pLDDT score > 75) and manually extracted Ras-interacting domains from the full-length proteins. For the proteins ARAF, RAF1, RGL1, and RASA4 we generated multiple candidate binder versions corresponding to different truncations or domains of the full-length protein. We also mutated sequence regions known to act as nuclear localization signals (NLS). Furthermore, we used RFdiffusion [37] (*Base_ckpt* and *Complex_beta_ckpt* model with default parameters; no hotspot residue selection) to *de novo* design Ras binders between 50 and 100 amino acids in length. Briefly, target structures (KRAS, HRAS, NRAS including GTP or analog nucleotide as ligand) were obtained from the Protein Data Bank (PDB) [38]. PDB assemblies were filtered and processed to provide a single Ras domain as input for RFdiffusion. Sequence design was performed with ProteinMPNN-FastRelax (*dl_binder_design* pipeline) [39,40]. After co-folding candidate binders with their corresponding target using AlphaFold2 [41] (*dl_binder_design* pipeline), binders were filtered for high-confidence Ras interactions (interface PAE score < 10 and interface pLDDT score > 80). Binders with high likelihood of dimerization in the absence of Ras were removed (co-folding of binder homodimers with AlphaFold3). In parallel, we compiled a list of synthetic Ras-binding domains such as monobodies [27], DARPins

[28,29], synthetic proteins [30], and nanobodies [31] from the available literature. All sequences were codon-optimized for expression in human cells (Genscript).

Sensor screening

To evaluate the sensitivity and specificity of candidate Ras sensors, we reverse transfected HEK293FT cells (275k seeding density) with three separate plasmid mixes encoding (1) binder-cTEVP (120 ng), binder-nTEVP-IRES-mTagBFP2 (150 ng); (2) wild-type or mutant Ras (15 ng), mRuby3 (45 ng); and (3) iTEVP reporter fused to a CAAX membrane tether (170 ng). Transfections were performed with Lipofectamine 3000 according to the manufacturer's instructions. To characterize the binders, we gated for medium sensor (mTagBFP2 expression between 10^4 and 10^6 a.u.) and high Ras expression (mRuby3 expression between 10^5 and 10^6 a.u.). To analyze sensor responses to varying amounts of Ras, we gated for medium sensor expression (mTagBFP2 expression between 10^4 and 10^6 a.u.) and binned Ras expression as shown in plots. All plots show median reporter activation for the corresponding gate or bin. Confidence estimates for sensor screening experiments were obtained by bootstrapping (95% confidence intervals; 1,000 bootstrap iterations).

Sensor targeting scope characterization

To evaluate the targeting scope of Ras sensors, we tested the sensor performance against a list of Ras variants compiled by selecting all KRAS, HRAS, and NRAS variants from the TCGA pan-cancer database (accessed via the cbiportal server) that are present in at least 10 cancer patients [33,34]. Analog to our sensor screening procedure, we reverse transfected HEK293FT cells (200k seeding density) with three separate plasmid mixes encoding (1) binder-cTEVP (133 ng), binder-nTEVP-IRES-mTagBFP2 (180 ng); (2) wild-type or mutant Ras (13 ng), mRuby3 (40 ng); and (3) iTEVP reporter fused to a CAAX membrane tether (200 ng). Transfections were performed with FuGENE HD according to the manufacturer's instructions. To calculate the fold-change of the response to mutant vs. wild-type Ras, we gated for medium sensor (mTagBFP2 expression between 10^4 and $10^{5.5}$ a.u.) and high Ras expression (mRuby3 expression between 10^5 and 10^6 a.u.) and divided the median activation to a given mutant Ras variant to the median activation to the

corresponding wild-type Ras isoform. Confidence estimates were obtained by bootstrapping (95% confidence intervals; 1,000 bootstrap iterations).

Single-cell classification performance of sensors

To evaluate the ability of our sensors to discriminate between wild-type (WT) and mutant Ras proteins at the single-cell level, we conducted receiver operating characteristic (ROC) curve analysis. First, we selected all cells with medium sensor (mTagBFP2 expression between 10^4 and $10^{5.5}$ a.u.) and high Ras expression (mRuby3 expression between 10^5 and 10^6 a.u.). Next, for each sensor, we compared normalized reporter activation between cells expressing mutant Ras variants and those expressing the corresponding wild-type proteins. Normalized activation was calculated as the ratio of the iTEVP activation signal to the iTEVP expression level (IFP/GFP). ROC curves were generated for each sensor by setting thresholds across the range of observed normalized reporter values. At each threshold, we classified cells into true positives (mutant cells above threshold), false positives (wild-type cells above threshold), true negatives (wild-type cells below threshold), and false negatives (mutant cells below threshold). The true positive rate (sensitivity) and false positive rate (1 - specificity) were calculated accordingly. The area under the ROC curve (AUC) was determined using the trapezoidal rule, providing a quantitative measure of each sensor's discriminatory performance. Higher AUC values indicated better sensor performance in distinguishing mutant from wild-type Ras proteins.

Sensor characterization in human cancer cell lines

To characterize the performance of sensors in human cancer cell lines, we reverse transfected 250k cancer cells in a 24 well plate with two separate plasmid mixes encoding (1) binder-cTEVP (100 ng), binder-nTEVP-IRES-mTagBFP2 (135 ng); and (2) iTEVP reporter fused to a CAAX membrane tether (150 ng). After 48h, cells were analyzed by flow cytometry. Median sensor activation was calculated as the ratio of the iTEVP activation signal to the iTEVP expression level (IFP/GFP). Confidence estimates were obtained by bootstrapping (95% confidence intervals; 1,000 bootstrap iterations). We used the same setup to characterize single-protein sensors. Median reporter activity was

calculated after gating for all sensor-transfected cells (mTagBFP2 expression between $10^{3.5}$ and 10^6 a.u.).

Software

The following software was used in this study:

Data collection: AlphaFold 3 (AlphaFold Server), Colabfold (v1.5.2), RFDiffusion (v1.1.0), ProteinMPNN-FastRelax (dl_binder_design v1.0.0), MetaMorph (version 6.2.6)

Data analysis: PyMol (version 2.5.4), ChimeraX (version 1.7.1), FlowJo (version 10.10.0), SnapGene (version 8.0.2), Geneious (version 2023.0.4), Bases2Fastq (Element Biosciences, <https://github.com/ElemBio/bases2fastq-dx>), NimbusImage, conda (v4.14.0), python (v3.12.3), bioconductor-biomart (v2.58.0), bioconductor-biostings (v2.70.1), bioconductor-deseq2 (v1.42.0), cairo (v1.18.0), imagemagick (v7.1.1_33), ipykernel (v6.29.5), ipython (v8.26.0), jupyter_server (v2.14.2), jupyterlab (v4.2.1), r-base (v4.3.3), r-cowplot (v1.1.3), r-dplyr (v1.1.4), r-essentials (v4.3), r-ggplot2 (v3.5.1), r-ggpubr (v0.6.0), r-ggrepel (v0.9.5), r-jsonlite (v1.8.8), r-magick (v2.8.3), r-colorbrewer (v1.1_3), r-tidyverse (v2.0.0), pandas (v2.2.3), matplotlib (v3.10.1), numpy (v2.2.4), scipy (v1.15.2), scikit-learn (v1.6.1), opencv-python (v4.7.0.72), scikit-image (v0.20.0), pillow (v9.5.0)

2.5.2 Key Resources Table

Reagent / Resource	Source	Identifier
Bacterial strains		
Stable Competent E. coli (High Efficiency)	NEB	C3040H
Reagents		
Dulbecco's Modified Eagle Medium	ThermoFisher Scientific	11960-069
Fetal bovine serum	Avantor	97068-085
Penicillin-Streptomycin-Glutamine	ThermoFisher Scientific	10378016
Sodium pyruvate	ThermoFisher Scientific	11360070
Minimal Essential Medium Non-Essential Amino Acids	ThermoFisher Scientific	11140050
Trypsin-EDTA (0.25%)	ThermoFisher Scientific	25200056
Dulbecco's Phosphate Buffered Saline	ThermoFisher Scientific	14040117
Opti-MEM I Reduced Serum Medium	ThermoFisher Scientific	31985070
Lipofectamine 3000	ThermoFisher Scientific	L3000008
LB Broth with agar (Lennox)	Sigma Aldrich	L2897-250G
Cell lines		
HEK293	ATCC	CRL-1573
MIA PaCa-2	ATCC	CRL-1420
NCI-H358	ATCC	CRL-5807
NCI-H441	ATCC	HTB-174
HepG2	ATCC	HB-8065

PLC/PRF/5	ATCC	CRL-8024
SNU-387	ATCC	CRL-2237
SNU-423	ATCC	CRL-2238
SNU-449	ATCC	CRL-2234
SNU-398	ATCC	CRL-2233
SNU-475	ATCC	CRL-2236
SW1573	ATCC	CRL-2170
Panc1	ATCC	CRL-1469
Recombinant DNA		
Plasmid for Ectopic Overexpression of HRAS G12A	This study	pLM0155
Plasmid for Ectopic Overexpression of HRAS G12C	This study	pLM0156
Plasmid for Ectopic Overexpression of HRAS G12D	This study	pLM0157
Plasmid for Ectopic Overexpression of HRAS G12R	This study	pLM0158
Plasmid for Ectopic Overexpression of HRAS G12S	This study	pLM0159
Plasmid for Ectopic Overexpression of HRAS G12V	This study	pLM0160
Plasmid for Ectopic Overexpression of HRAS G13C	This study	pLM0161
Plasmid for Ectopic Overexpression of HRAS G13D	This study	pLM0162
Plasmid for Ectopic Overexpression of HRAS G13dup	This study	pLM0163
Plasmid for Ectopic Overexpression of HRAS G13R	This study	pLM0164
Plasmid for Ectopic Overexpression of HRAS G13S	This study	pLM0165

Plasmid for Ectopic Overexpression of HRAS G13V	This study	pLM0166
Plasmid for Ectopic Overexpression of HRAS Q61H	This study	pLM0167
Plasmid for Ectopic Overexpression of HRAS Q61K	This study	pLM0168
Plasmid for Ectopic Overexpression of HRAS Q61L	This study	pLM0169
Plasmid for Ectopic Overexpression of HRAS Q61R	This study	pLM0170
Plasmid for Ectopic Overexpression of KRAS-4B A146P	This study	pLM0171
Plasmid for Ectopic Overexpression of KRAS-4B A146T	This study	pLM0172
Plasmid for Ectopic Overexpression of KRAS-4B A146V	This study	pLM0173
Plasmid for Ectopic Overexpression of KRAS-4B G12A	This study	pLM0174
Plasmid for Ectopic Overexpression of KRAS-4B G12C	This study	pLM0175
Plasmid for Ectopic Overexpression of KRAS-4B G12D	This study	pLM0176
Plasmid for Ectopic Overexpression of KRAS-4B G12R	This study	pLM0177
Plasmid for Ectopic Overexpression of KRAS-4B G12S	This study	pLM0178
Plasmid for Ectopic Overexpression of KRAS-4B G12V	This study	pLM0179
Plasmid for Ectopic Overexpression of KRAS-4B G13C	This study	pLM0180
Plasmid for Ectopic Overexpression of KRAS-4B G13D	This study	pLM0181

Plasmid for Ectopic Overexpression of KRAS-4B G13V	This study	pLM0182
Plasmid for Ectopic Overexpression of KRAS-4B Q61E	This study	pLM0183
Plasmid for Ectopic Overexpression of KRAS-4B Q61H	This study	pLM0184
Plasmid for Ectopic Overexpression of KRAS-4B Q61K	This study	pLM0185
Plasmid for Ectopic Overexpression of KRAS-4B Q61L	This study	pLM0186
Plasmid for Ectopic Overexpression of KRAS-4B Q61P	This study	pLM0187
Plasmid for Ectopic Overexpression of KRAS-4B Q61R	This study	pLM0188
Plasmid for Ectopic Overexpression of NRAS G12A	This study	pLM0189
Plasmid for Ectopic Overexpression of NRAS G12C	This study	pLM0190
Plasmid for Ectopic Overexpression of NRAS G12D	This study	pLM0191
Plasmid for Ectopic Overexpression of NRAS G12R	This study	pLM0192
Plasmid for Ectopic Overexpression of NRAS G12S	This study	pLM0193
Plasmid for Ectopic Overexpression of NRAS G12V	This study	pLM0194
Plasmid for Ectopic Overexpression of NRAS G13D	This study	pLM0195
Plasmid for Ectopic Overexpression of NRAS G13R	This study	pLM0196
Plasmid for Ectopic Overexpression of NRAS Q61*	This study	pLM0197

Plasmid for Ectopic Overexpression of NRAS Q61H	This study	pLM0198
Plasmid for Ectopic Overexpression of NRAS Q61K	This study	pLM0199
Plasmid for Ectopic Overexpression of NRAS Q61L	This study	pLM0200
Plasmid for Ectopic Overexpression of NRAS Q61P	This study	pLM0201
Plasmid for Ectopic Overexpression of NRAS Q61R	This study	pLM0202
Plasmid for Ectopic Overexpression of HRAS WT	This study	pAL0109
Plasmid for Ectopic Overexpression of KRAS-4B WT	This study	pAL0106
Plasmid for Ectopic Overexpression of NRAS WT	This study	pAL0111
Plasmid for iTEVP-CAAX reporter	This study	pAL0031
Plasmid for mRuby3	This study	pZAG0744
Plasmid for neomycin resistance gene	This study	pZAG0530
Plasmid to express 12VC1-nTEVP-tevs-dcTEVP-IRES-BFP	This study	P-0215
Plasmid to express 12VC1-nTEVP-tevD-dcTEVP-IRES-BFP	This study	P-0216
Plasmid to express 12VC1-nTEVP-tevs-DHFR-IRES-BFP	This study	P-0218
Plasmid to express 12VC1-nTEVP-tevs-dcTEVP-3xNLS-IRES-BFP	This study	P-0219
Plasmid to express 12VC1-nTEVP-tevD-dcTEVP-3xNLS-IRES-BFP	This study	P-0220
Plasmid to express 12VC1-cTEVP-tevs-dnTEVP	This study	P-0222
Plasmid to express 12VC1-cTEVP-tevD-dnTEVP	This study	P-0223

Plasmid to express 12VC1-cTEVP-tevs-DHFR	This study	P-0225
Plasmid to express 12VC1-nTEVP-tevs-3xNLS-IRES-BFP	This study	P-0393
Plasmid to express P4-nTEVP-IRES-BFP	This study	pLM104
Plasmid to express P3-cTEVP	This study	pLM107
Plasmid to express GSGSG-nTEVP-IRES-BFP	This study	PTC-01
Plasmid to express CRAF-nTEVP-IRES-BFP	This study	PTC-02
Plasmid to express HRAS-peptide-CRAF-nTEVP-IRES-BFP	This study	PTC-03
Plasmid to express NS1-nTEVP-IRES-BFP	This study	PTC-04
Plasmid to express JAM20-nTEVP-IRES-BFP	This study	PTC-05
Plasmid to express K13-nTEVP-IRES-BFP	This study	PTC-06
Plasmid to express K19-nTEVP-IRES-BFP	This study	PTC-07
Plasmid to express RA_RASSF1-nTEVP-IRES-BFP	This study	PTC-08
Plasmid to express RA_RASSF6-nTEVP-IRES-BFP	This study	PTC-09
Plasmid to express R15m10-nTEVP-IRES-BFP	This study	PTC-10
Plasmid to express 12VC1-nTEVP-IRES-BFP	This study	PTC-11
Plasmid to express 12VC3-nTEVP-IRES-BFP	This study	PTC-12
Plasmid to express GSGSG-cTEVP-WT	This study	PTC-13
Plasmid to express CRAF-cTEVP-WT	This study	PTC-14
Plasmid to express HRAS-peptide-CRAF-cTEVP-WT	This study	PTC-15
Plasmid to express NS1-cTEVP-WT	This study	PTC-16
Plasmid to express JAM20-cTEVP-WT	This study	PTC-17
Plasmid to express K13-cTEVP-WT	This study	PTC-18
Plasmid to express K19-cTEVP-WT	This study	PTC-19
Plasmid to express RA_RASSF1-cTEVP-WT	This study	PTC-20

Plasmid to express RA_RASSF6-cTEVP-WT	This study	PTC-21
Plasmid to express R15m10-cTEVP-WT	This study	PTC-22
Plasmid to express 12VC1-cTEVP-WT	This study	PTC-23
Plasmid to express 12VC3-cTEVP-WT	This study	PTC-24
Plasmid to express GSGSG-nTEVP-WT-IRES-BFP	This study	PTC-25
Plasmid to express GSGSG-nTEVP-T30A-IRES-BFP	This study	PTC-26
Plasmid to express GSGSG-nHyperTEV60-IRES-BFP	This study	PTC-27
Plasmid to express GSGSG-cTEVP-WT	This study	PTC-28
Plasmid to express GSGSG-cTEVP Δ	This study	PTC-29
Plasmid to express GSGSG-cTEVP Δ -I138T-S153N-T180A (uTEV3)	This study	PTC-30
Plasmid to express GSGSG-cHyperTEV60	This study	PTC-31
Plasmid to express CRAF-RBD-nTEVP-WT-IRES-BFP	This study	PTC-32
Plasmid to express CRAF-RBD-nTEVP-T30A-IRES-BFP	This study	PTC-33
Plasmid to express CRAF-RBD-nHyperTEV60-IRES-BFP	This study	PTC-34
Plasmid to express CRAF-RBD-cTEVP-WT	This study	PTC-35
Plasmid to express CRAF-RBD-cTEVP Δ	This study	PTC-36
Plasmid to express CRAF-RBD-cTEVP Δ -I138T-S153N-T180A (uTEV3)	This study	PTC-37
Plasmid to express CRAF-RBD-cHyperTEV60	This study	PTC-38
Plasmid to express GRB2-IRES-mRuby3	This study	PTC-42
Plasmid to express 12VC1-nTEVP-T30A-IRES-BFP	This study	PTC-44
Plasmid to express 12VC1-cTEVP Δ	This study	PTC-45

Plasmid to express 12VC1-cTEVP Δ -I138T-S153N-T180A (uTEV3)	This study	PTC-46
Plasmid to express CRAF _{x2} -nTEVP-WT-IRES-BFP	This study	PTC-47
Plasmid to express CRAF _{x3} -nTEVP-WT-IRES-BFP	This study	PTC-48
Plasmid to express 12VC1 _{x2} -nTEVP-WT-IRES-BFP	This study	PTC-49
Plasmid to express 12VC1 _{x3} -nTEVP-WT-IRES-BFP	This study	PTC-50
Plasmid to express pHRAS-WT-CRAF-nTEVP-WT-IRES-BFP	This study	PTC-51
Plasmid to express pHRAS-G12V-CRAF-nTEVP-WT-IRES-BFP	This study	PTC-52
Plasmid to express pHRAS-WT-12VC1-nTEVP-WT-IRES-BFP	This study	PTC-53
Plasmid to express pHRAS-G12V-12VC1-nTEVP-WT-IRES-BFP	This study	PTC-54
Plasmid to express CRAF _{x2} -cTEVP-WT	This study	PTC-55
Plasmid to express CRAF _{x3} -cTEVP-WT	This study	PTC-56
Plasmid to express 12VC1 _{x2} -cTEVP-WT	This study	PTC-57
Plasmid to express 12VC1 _{x3} -cTEVP-WT	This study	PTC-58
Plasmid to express pHRAS-WT-CRAF-cTEVP-WT	This study	PTC-59
Plasmid to express pHRAS-G12V-CRAF-cTEVP-WT	This study	PTC-60
Plasmid to express pHRAS-WT-12VC1-cTEVP-WT	This study	PTC-61
Plasmid to express pHRAS-G12V-12VC1-cTEVP-WT	This study	PTC-62
deadTEVP_mTagBFP2	This study	pZAG0559
TEVP_mTagBFP2	This study	pZAG0560

CHAPTER 2 BIBLIOGRAPHY

1. Perurena N, Cichowski K. Finding the sweet spot: Targeting RAS in tumors while sparing normal tissue. *Cancer Cell*. 2024;42: 943–945. doi:10.1016/j.ccell.2024.05.020
2. Zou X, Zhao C, Beier KT, Kang C-Y, Lin MZ. Rewiring oncogenic signaling to RNA vector replication for the treatment of metastatic cancer. *bioRxiv.org*. 2025. doi:10.1101/2024.12.30.630713
3. Behranvand N, Nasri F, Zolfaghari Emameh R, Khani P, Hosseini A, Garssen J, et al. Chemotherapy: a double-edged sword in cancer treatment. *Cancer Immunology, Immunotherapy*. 2021;71: 507–526. doi:10.1007/s00262-021-03013-3
4. van den Boogaard WMC, Komninos DSJ, Vermeij WP. Chemotherapy side-effects: Not all DNA damage is equal. *Cancers (Basel)*. 2022;14: 627. doi:10.3390/cancers14030627
5. June CH, O'Connor RS, Kawalekar OU, Ghassemi S, Milone MC. CAR T cell immunotherapy for human cancer. *Science*. 2018;359: 1361–1365. doi:10.1126/science.aar6711
6. Sterner RC, Sterner RM. CAR-T cell therapy: current limitations and potential strategies. *Blood Cancer J*. 2021;11: 69. doi:10.1038/s41408-021-00459-7
7. Chau CH, Steeg PS, Figg WD. Antibody-drug conjugates for cancer. *Lancet*. 2019;394: 793–804. doi:10.1016/S0140-6736(19)31774-X
8. Beck A, Goetsch L, Dumontet C, Corvaia N. Strategies and challenges for the next generation of antibody-drug conjugates. *Nat Rev Drug Discov*. 2017;16: 315–337. doi:10.1038/nrd.2016.268
9. Gao XJ, Chong LS, Kim MS, Elowitz MB. Programmable protein circuits in living cells. *Science*. 2018 [cited 18 Mar 2025]. doi:10.1126/science.aat5062
10. Vlahos AE, Kang J, Aldrete CA, Zhu R, Chong LS, Elowitz MB, et al. Protease-controlled secretion and display of intercellular signals. *Nat Commun*. 2022;13: 912. doi:10.1038/s41467-022-28623-y
11. Chung HK, Zou X, Bajar BT, Brand VR, Huo Y, Alcudia JF, et al. A compact synthetic pathway rewires cancer signaling to therapeutic effector release. *Science (New York, NY)*. 2019;364: eaat6982. doi:10.1126/science.aat6982

12. Xia S, Lu AC, Tobin V, Luo K, Moeller L, Shon DJ, et al. Synthetic protein circuits for programmable control of mammalian cell death. *Cell*. 2024;187: 2785–2800.e16. doi:10.1016/j.cell.2024.03.031
13. Orehek S, Ramuta TŽ, Lainšček D, Malenšek Š, Šala M, Benčina M, et al. Cytokine-armed pyroptosis induces antitumor immunity against diverse types of tumors. *Nat Commun*. 2024;15: 10801. doi:10.1038/s41467-024-55083-3
14. Fink T, Lonžarić J, Praznik A, Plaper T, Merljak E, Leben K, et al. Design of fast proteolysis-based signaling and logic circuits in mammalian cells. *Nature chemical biology*. 2019;15. doi:10.1038/s41589-018-0181-6
15. Langan RA, Boyken SE, Ng AH, Samson JA, Dods G, Westbrook AM, et al. De novo design of bioactive protein switches. *Nature*. 2019;572: 205–210. doi:10.1038/s41586-019-1432-8
16. Zhang JZ, Nguyen WH, Greenwood N, Rose JC, Ong S-E, Maly DJ, et al. Computationally designed sensors detect endogenous Ras activity and signaling effectors at subcellular resolution. *Nat Biotechnol*. 2024. doi:10.1038/s41587-023-02107-w
17. Chen Z, Linton JM, Xia S, Fan X, Yu D, Wang J, et al. A synthetic protein-level neural network in mammalian cells. *Science*. 2024;386: 1243–1250. doi:10.1126/science.add8468
18. Chen Z, Elowitz MB. Programmable protein circuit design. *Cell*. 2021;184: 2284–2301. doi:10.1016/j.cell.2021.03.007
19. Plaper T, Merljak E, Fink T, Satler T, Ljubetič A, Lainšček D, et al. Designed allosteric protein logic. *Cell Discov*. 2024;10: 8. doi:10.1038/s41421-023-00635-y
20. Gao XJ, Chong LS, Ince MH, Kim MS, Elowitz MB. Engineering multiple levels of specificity in an RNA viral vector. *bioRxiv*. bioRxiv; 2020. p. 2020.05.27.119909. doi:10.1101/2020.05.27.119909
21. Kitada T, DiAndreth B, Teague B, Weiss R. Programming gene and engineered-cell therapies with synthetic biology. *Science*. 2018;359. doi:10.1126/science.aad1067
22. Punekar SR, Velcheti V, Neel BG, Wong K-K. The current state of the art and future trends in RAS-targeted cancer therapies. *Nature Reviews Clinical Oncology*. 2022;19: 637–655. doi:10.1038/s41571-022-00671-9

23. Prior IA, Hood FE, Hartley JL. The frequency of Ras mutations in cancer. *Cancer Res.* 2020;80: 2969–2974. doi:10.1158/0008-5472.CAN-19-3682
24. Wasko UN, Jiang J, Dalton TC, Curiel-Garcia A, Edwards AC, Wang Y, et al. Tumour-selective activity of RAS-GTP inhibition in pancreatic cancer. *Nature.* 2024;629: 927–936. doi:10.1038/s41586-024-07379-z
25. Puneekar SR, Velcheti V, Neel BG, Wong K-K. The current state of the art and future trends in RAS-targeted cancer therapies. *Nature Reviews Clinical Oncology.* 2022;19: 637–655. doi:10.1038/s41571-022-00671-9
26. Wasko UN, Jiang J, Dalton TC, Curiel-Garcia A, Edwards AC, Wang Y, et al. Tumour-selective activity of RAS-GTP inhibition in pancreatic cancer. *Nature.* 2024;629: 927–936. doi:10.1038/s41586-024-07379-z
27. Spencer-Smith R, Koide A, Zhou Y, Eguchi RR, Sha F, Gajwani P, et al. Inhibition of RAS function through targeting an allosteric regulatory site. *Nat Chem Biol.* 2017;13: 62–68. doi:10.1038/nchembio.2231
28. Bery N, Legg S, Debreczeni J, Breed J, Embrey K, Stubbs C, et al. KRAS-specific inhibition using a DARPin binding to a site in the allosteric lobe. *Nat Commun.* 2019;10: 2607. doi:10.1038/s41467-019-10419-2
29. Guillard S, Kolasinska-Zwierz P, Debreczeni J, Breed J, Zhang J, Bery N, et al. Structural and functional characterization of a DARPin which inhibits Ras nucleotide exchange. *Nat Commun.* 2017;8: 16111. doi:10.1038/ncomms16111
30. Wallon L, Khan I, Teng KW, Koide A, Zuberi M, Li J, et al. Inhibition of RAS-driven signaling and tumorigenesis with a pan-RAS monobody targeting the Switch I/II pocket. *Proc Natl Acad Sci U S A.* 2022;119: e2204481119. doi:10.1073/pnas.2204481119
31. Teng KW, Tsai ST, Hattori T, Fedele C, Koide A, Yang C, et al. Selective and noncovalent targeting of RAS mutants for inhibition and degradation. *Nat Commun.* 2021;12: 2656. doi:10.1038/s41467-021-22969-5
32. To T-L, Piggott BJ, Makhijani K, Yu D, Jan YN, Shu X. Rationally designed fluorogenic protease reporter visualizes spatiotemporal dynamics of apoptosis in vivo. *Proc Natl Acad Sci U S A.* 2015;112: 3338–3343. doi:10.1073/pnas.1502857112

33. Cerami E, Gao J, Dogrusoz U, Gross BE, Sumer SO, Aksoy BA, et al. The cBio cancer genomics portal: an open platform for exploring multidimensional cancer genomics data. *Cancer Discov.* 2012;2: 401–404. doi:10.1158/2159-8290.CD-12-0095
34. Sanchez-Vega F, Mina M, Armenia J, Chatila WK, Luna A, La KC, et al. Oncogenic Signaling Pathways in The Cancer Genome Atlas. *Cell.* 2018;173: 321–337.e10. doi:10.1016/j.cell.2018.03.035
35. von Mering C, Huynen M, Jaeggi D, Schmidt S, Bork P, Snel B. STRING: a database of predicted functional associations between proteins. *Nucleic Acids Res.* 2003;31: 258–261. doi:10.1093/nar/gkg034
36. Abramson J, Adler J, Dunger J, Evans R, Green T, Pritzel A, et al. Accurate structure prediction of biomolecular interactions with AlphaFold 3. *Nature.* 2024;630: 493–500. doi:10.1038/s41586-024-07487-w
37. Watson JL, Juergens D, Bennett NR, Trippe BL, Yim J, Eisenach HE, et al. De novo design of protein structure and function with RFDiffusion. *Nature.* 2023; 1–3. doi:10.1038/s41586-023-06415-8
38. Berman HM, Westbrook J, Feng Z, Gilliland G, Bhat TN, Weissig H, et al. The Protein Data Bank. *Nucleic Acids Res.* 2000;28: 235–242. doi:10.1093/nar/28.1.235
39. Dauparas J, Anishchenko I, Bennett N, Bai H, Ragotte RJ, Milles LF, et al. Robust deep learning-based protein sequence design using ProteinMPNN. *Science.* 2022;378: 49–56. doi:10.1126/science.add2187
40. Bennett NR, Coventry B, Goreshnik I, Huang B, Allen A, Vafeados D, et al. Improving de novo protein binder design with deep learning. *Nat Commun.* 2023;14: 2625. doi:10.1038/s41467-023-38328-5
41. Jumper J, Evans R, Pritzel A, Green T, Figurnov M, Ronneberger O, et al. Highly accurate protein structure prediction with AlphaFold. *Nature.* 2021;596: 583–589. doi:10.1038/s41586-021-03819-2

Chapter 3

SENSOR OPTIMIZATION AND SIGNAL AMPLIFICATION

3.1 Summary

In vivo gene delivery is less efficient than *in vitro* transfection[1]. To enable effective function under *in vivo* conditions, we optimized our circuit to maintain sensitivity at lower expression levels. This required sensor designs that remain robust despite limited protein abundance. We therefore focused on simplifying, optimizing, and amplifying mutant-specific Ras sensing. In many cases, we took inspiration from natural mechanisms of protein regulation. First, we compressed the two-gene sensor into a single-gene construct using a viral polyprotein-inspired architecture. Next, we took inspiration from natural proteolytic signaling cascades and engineered a protease-activatable protease capable of amplifying input signals. Finally, we introduced mutations identified through directed evolution to enhance protease catalytic efficiency. Together, these improvements establish a set of protease-based sensors and amplifiers that perform effectively at low expression levels and can support the construction of sensitive sense-and-kill circuits.

3.2 Introduction

Gene delivery *in vivo* is much less efficient than *in vitro* transfection. Most cells express low levels of the circuit *in vivo*, and this limits how well synthetic systems can work in realistic settings. Indeed, circuits that depend on high expression or precise stoichiometry often fail when only a small amount of protein is made. To solve this, sensors need to function reliably even at very low expression [1].

Proteases are a good starting point. They amplify signals by turning over many substrates per input, and they can easily be re-targeted using short recognition motifs. Protease

cascades, found in systems like coagulation, can amplify signals even more by linking one protease to the activation of another[2–4]. These features make proteases useful for building sensors that work when expression is limited.

Circuit size is another key limitation. Many delivery vectors, including viral and non-viral systems, have restricted payload capacity. Encoding all components in a single open reading frame is one way to address this constraint. Approaches such as self-cleaving 2A peptides[5] or viral polyprotein architectures enable co-expression of multiple proteins from a single transcript while maintaining defined stoichiometry. These compact designs are more compatible with in vivo delivery. However, each approach presents specific tradeoffs, including differences in cleavage/skipping efficiency, and thereby expression balance.

3.3 Results

3.3.1 Sensor optimization improves sensitivity

We first redesigned the two-protein sensor as a single gene construct (**Fig. 3.1A**). First, we tried incorporating a T2A-P2A ribosomal skipping sequence. However, this modification degraded sensor performance (**Fig. 3.1B**). This is consistent with known limitations of 2A sequences, where ribosomal “skipping” is not always efficient. While reported cleavage efficiencies for P2A and T2A peptides vary drastically, incomplete cleavage can lead to fusion proteins that impair function[5]. In addition, ribosomes can occasionally fall off after the 2A site, resulting in unequal expression of downstream components.

As an alternative, we turned to a viral polyprotein-inspired design, in which the sensor protease cleaves itself post-translationally to release both functional halves of the sensor. This approach mirrors natural systems such as the poliovirus polyprotein[5–7], which encodes structural and enzymatic proteins as a single open reading frame that is cleaved by the viral 3C protease [35]. Similar strategies are seen across picornaviruses, flaviviruses,

and retroviruses, many of which rely on precise intramolecular cleavage for viral maturation[8–10]. Notably, these viral proteases are clinically relevant drug targets, with inhibitors developed for hepatitis C virus (e.g., NS3/4A protease inhibitors[11]) and HIV (e.g., protease inhibitors like darunavir[11–13]), reflecting their central role in polyprotein processing. Borrowing from this concept, in our system a polyprotein containing both Ras sensor protein halves post-translationally cleaves itself into the two sensor components. We found that these self-cleaving designs increased maximal activation.

Finally, incorporating TEV protease mutations [14,15] further enhanced sensitivity (**Fig. 3.1B**). These mutations, derived from a directed evolution campaign, yielded a TEV variant (u3) with improved catalytic efficiency. The evolved protease maintains the core specificity of wild-type TEV but cleaves more rapidly and robustly. Based on these results, we adopted the self-cleaving sensor v2-s for subsequent experiments.

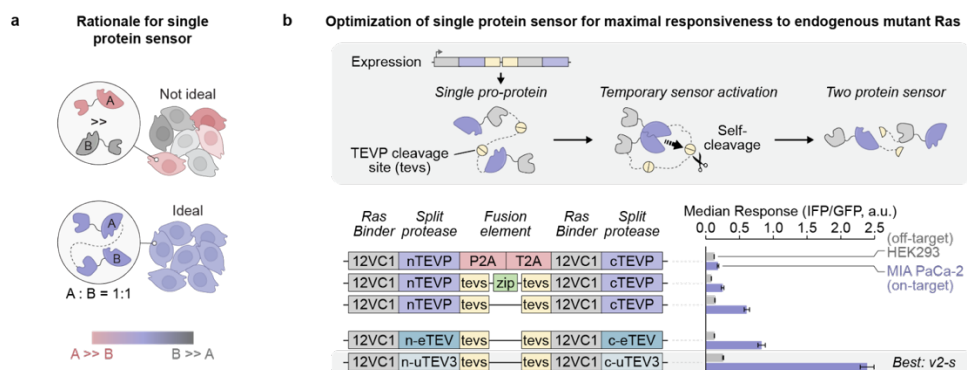


Fig. 3.1. Cis protease regulation increases sensitivity. (A) Single-protein sensor designs facilitate 1:1 stoichiometry between sensor components to improve sensor performance. **(B)** Sensor v2-s improves mutant Ras discrimination through “self-cleaving” mechanism (cis regulation) inspired by natural viral mechanisms. Some sensor designs incorporated mutant TEV protease variants (eTEV, uTEV3) with

elevated catalytic efficiencies [14,15]. Median sensor responses (IFP/GFP ratio) were measured in on-target (KRAS^{G12C}-expressing MIA PaCa-2) and off-target (wild-type KRAS-expressing HEK293) cells.

3.3.2 Design of protease-activatable proteases

We also explored signal amplification as a complementary approach to enhance sensor performance. Inspired by amplifying proteolytic cascades in cell death pathways [16,17], we engineered synthetic protease-activatable proteases (**Fig. 3.2**) using the tobacco vein mottling virus protease (TVMVP), which is orthogonal to the TEV protease.

We designed a panel of candidate protease-activatable proteases based on diverse natural and synthetic protein activation mechanisms. All constructs were expressed in HEK293 cells via transient transfection for characterization.

Candidates 1-3: To emulate autoinhibition-based activation mechanisms observed in proteins such as WASP, SNARE, and ERM, we designed constructs in which a non-cleavable, synthetic autoinhibitory peptide was tethered to the active site of TVMV protease (TVMVP) [18]. The tether included a cleavage site for an orthogonal protease (TEVP), enabling activation through proteolytic removal of the inhibitory domain. Constructs were tested with and without co-expression of the activating TEVP protease. To modulate inhibitory dynamics, we generated a series of variants with progressively shortened linkers between the autoinhibitory peptide and TVMVP.

Candidates 4-7: To improve autoinhibition, we developed a tethering strategy in which the autoinhibitory peptide was anchored at both termini via two TEVP cleavage sites. We circularly permuted the TVMVP sequence and rejoined the new termini using antiparallel leucine zippers to stabilize the conformation. To optimize access of TEVP to its cleavage sites, we also varied the length of the linker flanking the autoinhibitory domain.

Candidates 8-10: We next explored strain-based inhibition, drawing inspiration from previous studies where circular permutation introduces conformational strain that disrupts protein function (*e.g.*, CRISPR) [19]. We engineered circularly permuted variants of TVMVP in which the old termini were joined by short linkers, embedding the TEVP cleavage site to allow strain release upon protease input. Additional constructs included deletions of disordered residues at the native termini to increase the distance between ends and enhance strain potential.

Candidates 11-13: To sterically inhibit the TVMVP active site, we fused bulky *de novo* designed heterodimers to the protease, positioned to occlude the catalytic cleft [20]. These heterodimeric blocking domains were flanked by TEVP cleavage sites to enable conditional displacement and activation.

Candidates 14-18: We adopted a protease caging strategy using split TVMVP [20–22]. One protease half was caged by fusion to a catalytically inactive TVMVP fragment via designed coiled coils. The coiled coil associated with the inactive half was flanked by TEVP cleavage sites, enabling conditional release. Additional constructs extended this strategy by caging both protease halves with inactive TVMVP fragments, each released via TEVP cleavage. To enable protease activation through strand displacement, we substituted the coiled coils with lower-affinity, sequence-matched variants previously reported to allow displacement by higher-affinity interactors. These designs were intended to facilitate TEVP-dependent exchange of inhibitory domains with active TVMVP halves.

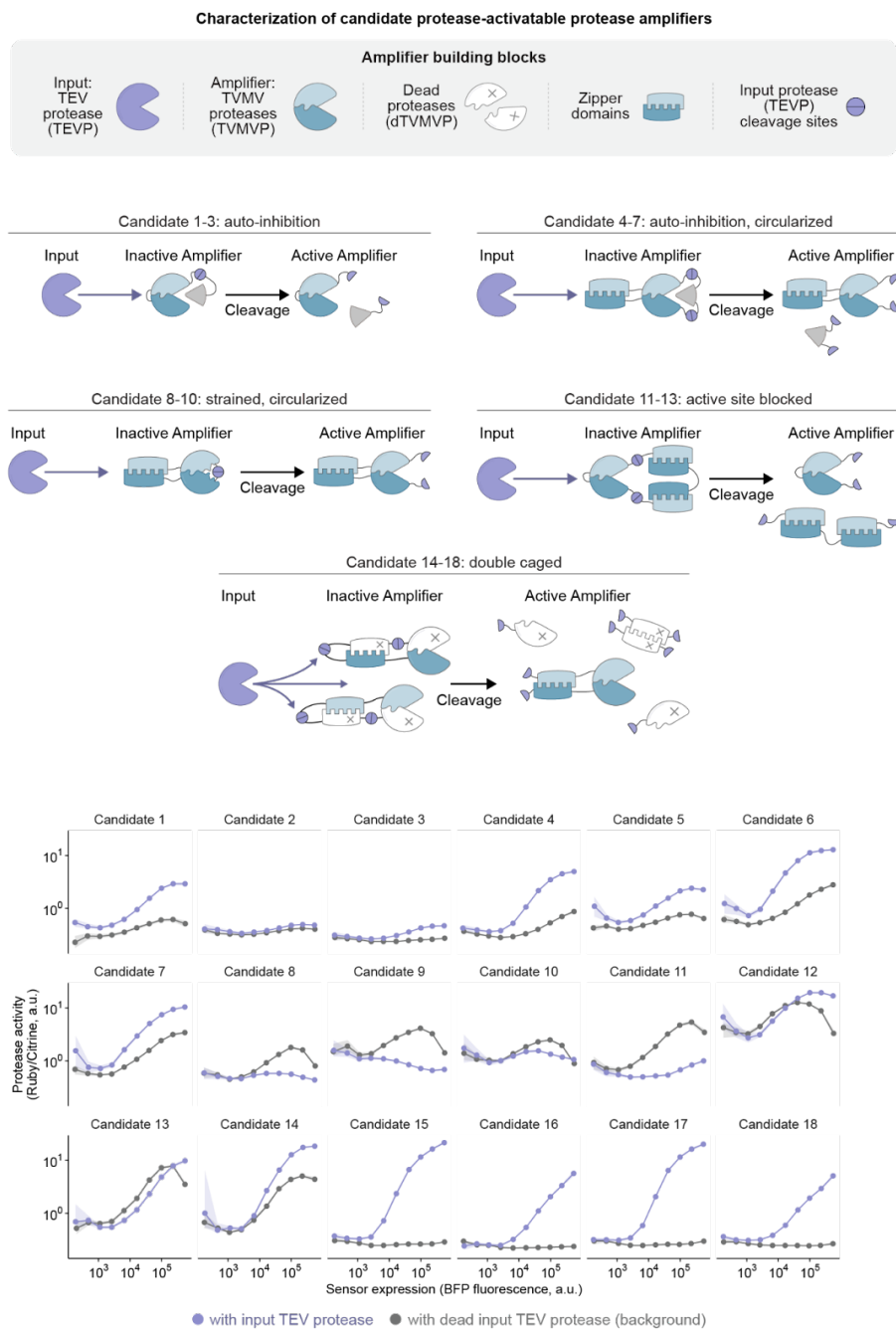


Fig. 3.2. Design and characterization of amplifiers. Schematic overview of rationally designed candidate constructs built from modular components,

including split TVMVP, catalytically inactive TVMVP, coiled-coil zipper domains, and input protease cleavage sites. Design details are provided in **Methods**. Most candidates showed TEVP-inducible activation with varying levels of background activity. Candidates 15-18, which employed a double-caged TVMVP architecture, achieved low background and high activation.

3.3.3 Signal amplification improves sensitivity

In the best design (Candidate 17), split TVMVP halves were fused to caging domains consisting of catalytically dead complementary protease halves, which could be removed through TEVP cleavage (**Fig. 3.3A**). Once cleaved by TEVP, active TVMVP halves can reconstitute via attached coiled-coiled domains (**Methods**). This double-caged system amplified input signals compared to a constitutive TEVP alone, while maintaining minimal background activity in the absence of input TEVP signals (**Fig. 3.3B**). Together, these results establish optimized sensors and amplifiers for downstream *in vivo* applications.

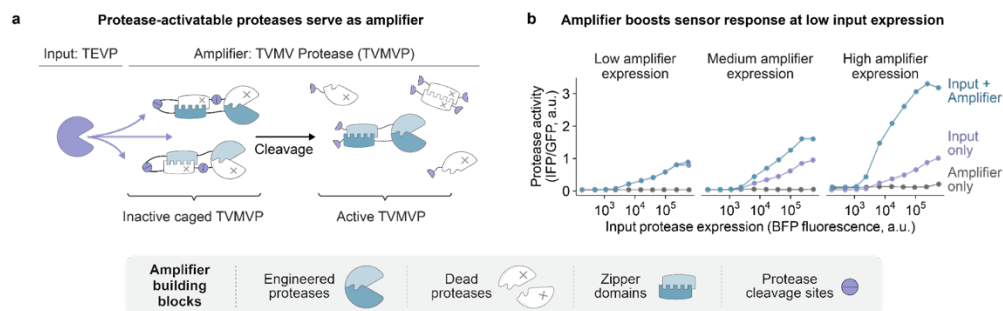


Fig. 3.3. Trans protease regulation increases sensitivity. (A) Amplifier proteases (TVMVP) can be activated by TEVP cleavage. In this design, both halves of split TVMVP are fused to their complementary, catalytically dead halves and held together by a weak coiled-coil interaction, thus intramolecularly caging and inhibiting TVMVP activity. Cleavage by TEVP removes the inactive fragments, allowing the active halves to displace the weak interaction with a stronger coiled-coil pair, reconstituting TVMV protease. **(B)** Protease amplifier increases output compared to non-amplified circuits when expressed at different levels (individual plots). Response curves are shown across low (gating for co-transfected Ruby between 10^3 - 10^4 a.u.), medium (10^4 - 10^5 a.u.), and high (10^5 - 10^6 a.u.) amplifier expression bins.

3.4 Methods

Plasmid construction

Plasmids were generated via Gibson Assembly (NEBuilder HiFi DNA Assembly Master Mix; New England BioLabs) or KLD cloning (T4 Polynucleotide Kinase, T4 DNA Ligase, DpnI, T4 DNA Ligase Buffer; Thermo Scientific). Gene fragments were sourced from Twist Bioscience or Integrated DNA Technologies (IDT), or PCR-amplified from existing laboratory plasmid constructs. IDT synthesized all PCR primers. Plasmids were purified (QIAprep Spin Miniprep Kit or Qiacube machine; Qiagen), normalized (Thermo Scientific NanoDrop 8000), and sequence-verified (Plasmidsaurus or Genewiz) prior to experimental use.

Tissue culture and cell lines

Most cell lines were obtained from ATCC and cultured under standard conditions (37°C, 5% CO₂, humidified Eppendorf CellXpert C170i incubator). Adherent cells were maintained in Dulbecco's Modified Eagle Media (DMEM; Thermo Fisher) supplemented with 10% fetal bovine serum (FBS; Avantor), penicillin (1 unit/ml), streptomycin (1 µg/ml), glutamine (2 mM), sodium pyruvate (1 mM), and 1X Minimal Essential Media Non-Essential Amino Acids (all Thermo Fisher). HEK293FT cells were cultured for up to 20 passages, and human cancer cell lines for up to 15 passages, maintaining 10%-90% confluency. Cells were passaged using 0.25% Trypsin-EDTA (Thermo Fisher). Viable cell numbers for seeding densities were determined using Trypan Blue (Invitrogen) and the Countess 3 automated cell counter (Thermo Fisher). Cells were routinely confirmed mycoplasma-free (MycoStrip kit; InvivoGen).

Transient transfection

Transient transfections were performed utilizing FuGENE HD (Promega), Lipofectamine 3000 (Thermo Fisher), or LNPs (described below) as transfection agents. Unless otherwise noted, we seeded 10k cells (96-well plate), 200k cells (24-well plate) for FuGENE or LNP

transfections, and 275k cells (24-well plate) for Lipofectamine transfections. Cells were reverse-transfected immediately after seeding following manufacturer instructions. For FuGENE transfections, we incubated 1 μ g plasmid DNA with 6 μ l transfection reagent. For FuGENE transfections, 200k cells were transfected with up to 566 ng of DNA. For Lipofectamine transfections, 1.5 μ l Lipofectamine 3000 and 1.5 μ l reagent P3000 were used with a total of 500 ng DNA to transfect an equivalent of 275k cells. The total amount of plasmid DNA applied in each transfection was scaled according to seeding densities.

Flow cytometry

Cells were collected two days post-transient transfection for flow cytometry, filtered through a 40- μ m cell strainer, and analyzed by flow cytometry (CytoFLEX S flow cytometer, Beckman Coulter). Unless otherwise noted, we used FITC-A channel (GFP of iTEVP reporter[23]; excitation 488 nm, emission 525/40 nm; gain of 1), ECD-A channel (mRuby3; excitation 561 nm, emission 610/20 nm; gain of 1), PB450-A channel (mTagBFP2; excitation 405 nm, emission 450/45 nm; gain of 1), and APC-A700-A channel (IFP of iTEVP reporter; excitation 638 nm, emission 712/25; gain of 100). Live cells and singlets were gated using FlowJo (version 10.10, BD Biosciences). iTEVP reporter activation was assessed by calculating the IFP (activation) to GFP (reporter expression) ratio for cells with GFP expression between 10^5 and 10^6 a.u., corresponding to the reporter expression regime with maximal dynamic range. As the reporter construct was always transfected as a separate polytransfection mix, selecting cells with high reporter expression did not bias subsequent analysis steps, *i.e.*, the expression distribution of other constructs (*e.g.*, reporter or ectopic Ras) remained unaffected.

Amplifier characterization in human cancer cell lines

To characterize the performance of sensors in human cancer cell lines, we reverse transfected 250k cancer cells in a 24 well plate with two separate plasmid mixes encoding (1) binder-cTEVP (100 ng), binder-nTEVP-IRES-mTagBFP2 (135 ng); and (2) iTEVP reporter fused to a CAAX membrane tether (150 ng). After 48h, cells were analyzed by

flow cytometry. Median sensor activation was calculated as the ratio of the iTEVP activation signal to the iTEVP expression level (IFP/GFP). Confidence estimates were obtained by bootstrapping (95% confidence intervals; 1,000 bootstrap iterations). We used the same setup to characterize single-protein sensors. Median reporter activity was calculated after gating for all sensor-transfected cells (mTagBFP2 expression between $10^{3.5}$ and 10^6 a.u.).

Software

The following software was used in this study:

Data collection: AlphaFold 3 (AlphaFold Server), Colabfold (v1.5.2), RFDiffusion (v1.1.0), ProteinMPNN-FastRelax (dl_binder_design v1.0.0), MetaMorph (version 6.2.6)

Data analysis: PyMol (version 2.5.4), ChimeraX (version 1.7.1), FlowJo (version 10.10.0), SnapGene (version 8.0.2), Geneious (version 2023.0.4), Bases2Fastq (Element Biosciences, <https://github.com/ElementBio/bases2fastq-dx>), NimbusImage, conda (v4.14.0), python (v3.12.3), bioconductor-biomart (v2.58.0), bioconductor-biostings (v2.70.1), bioconductor-deseq2 (v1.42.0), cairo (v1.18.0), imagemagick (v7.1.1_33), ipykernel (v6.29.5), ipython (v8.26.0), jupyter_server (v2.14.2), jupyterlab (v4.2.1), r-base (v4.3.3), r-cowplot (v1.1.3), r-dplyr (v1.1.4), r-essentials (v4.3), r-ggplot2 (v3.5.1), r-ggpubr (v0.6.0), r-ggrepel (v0.9.5), r-jsonlite (v1.8.8), r-magick (v2.8.3), r-colorbrewer (v1.1_3), r-tidyverse (v2.0.0), pandas (v2.2.3), matplotlib (v3.10.1), numpy (v2.2.4), scipy (v1.15.2), scikit-learn (v1.6.1), opencv-python (v4.7.0.72), scikit-image (v0.20.0), pillow (v9.5.0)

3.4.2 Key Resources Table

Reagent / Resource	Source	Identifier
Bacterial strains		
Stable Competent E. coli (High Efficiency)	NEB	C3040H
Reagents		
Dulbecco's Modified Eagle Medium	ThermoFisher Scientific	11960-069
Fetal bovine serum	Avantor	97068-085
Penicillin-Streptomycin-Glutamine	ThermoFisher Scientific	10378016
Sodium pyruvate	ThermoFisher Scientific	11360070
Minimal Essential Medium Non-Essential Amino Acids	ThermoFisher Scientific	11140050
Trypsin-EDTA (0.25%)	ThermoFisher Scientific	25200056
Dulbecco's Phosphate Buffered Saline	ThermoFisher Scientific	14040117
Opti-MEM I Reduced Serum Medium	ThermoFisher Scientific	31985070
Lipofectamine 3000	ThermoFisher Scientific	L3000008
LB Broth with agar (Lennox)	Sigma Aldrich	L2897-250G

Cell lines		
HEK293	ATCC	CRL-1573
MIA PaCa-2	ATCC	CRL-1420
Recombinant DNA		
Plasmid for iTEVP-CAAX reporter	This study	pAL0031
Plasmid for mRuby3	This study	pZAG0744
Plasmid for neomycin resistance gene	This study	pZAG0530
12VC1-nTEVP-P2A-T2A-12VC1-cTEVP	This study	pAL0376
12VC1-nTEVP-tevs-GSGSG-tevs-12VC1-cTEVP	This study	pAL0377
12VC1-nTEVP-tevs-NZp-tevs-12VC1-cTEVP	This study	pAL0378
IVT_deadTVMVP_T2A_halo	This study	pZAG0550
IVT_TVMVP_T2A_halo	This study	pZAG0551
IVT_SPOC_P3-AP4ms_T2A_AP3ms-P4_P2A_halo	This study	pZAG0553
IVT230_nTVMVP-DHD37A-tevs-DHD15B-tevs-cTVMVPmut-T2A-nTVMVPmut-tevs-15A-tevs-37B-cTVMVP	This study	pZAG0457
IVT230_nTVMVP-P3-tevs-AP4ms-tevs-cTVMVPmut	This study	pZAG0468
IVT230_nTVMVPmut-tevs-P3ms-tevs-AP4-cTVMVP	This study	pZAG0470
IVT230_nTVMVP-P3-tevs-AP4ms-tevs-cTVMVPmut	This study	pZAG0468
IVT230_nTVMVPmut-tevs-P3ms-tevs-AP4-cTVMVP-I40D	This study	pZAG0471

IVT230_nTVMVP-P3-tevs-AP4ms-tevs-cTVMVPmut-I40D	This study	pZAG0469
IVT230_nTVMVPmut-tevs-P3ms-tevs-AP4-cTVMVP	This study	pZAG0470
IVT230_nTVMVP-P3-tevs-AP4ms-tevs-cTVMVPmut-I40D	This study	pZAG0469
IVT230_nTVMVPmut-tevs-P3ms-tevs-AP4-cTVMVP-I40D	This study	pZAG0471
P4_cTVMVP	This study	pZAG0504
cTVMVPmut_AP4_tevs_P3_nTVMVP	This study	pZAG0505
TVMVP_tevs_noninhibAI	This study	pZAG0148
TVMVP --- tevs --- AI (v1.1)	This study	pZAG0149
TVMVP --- tevs --- AI with custom linker around tevs #1 (v1.2)	This study	pZAG0150
TVMVP --- tevs --- AI with custom linker around tevs #2 (v1.3)	This study	pZAG0151
circular_perm_C-TVMVP_tevs_AI_tevs_N-TVMVP_2-AAlinker	This study	pZAG0152
circular_perm_C-TVMVP_tevs_AI_tevs_N-TVMVP_4-AAlinker	This study	pZAG0153
circular_perm_C-TVMVP_tevs_AI_tevs_N-TVMVP_8-AAlinker	This study	pZAG0154
cir-perm-AI-amp_CZp_20AAlinker_cTVMVP_tevs_AI_G_tevs_G_nTVMVP_20AAlinker_NZp	This study	pZAG0169
cir-perm-AI-amp_CZp_20AAlinker_cTVMVP_tevs_AI_G_tevs_G_nTVMVP-delSKA_20AAlinker_NZp	This study	pZAG0170
CZp_20linkr_cTVMVP_tevs_nTVMVP_20linkr_NZp	This study	pZAG0508

CZp_20linkr_cTVMVP_tevs_nTVMVP_20linkr_NZp_dUP4	This study	pZAG0510
CZp_20linkr_cTVMVP_tevs_nTVMVP_20linkr_NZp_dDW4	This study	pZAG0514
CZp_20linkr_cTVMVP_tevs_37A_tevs_37B_tevs_nTVMVP_20linkr_NZp	This study	pZAG0526
CZp_20linkr_cTVMVP_15A_tevs_15B___37B_tevs_37A_nTVMVP_20linkr_NZp	This study	pZAG0527
CZp_20linkr_cTVMVP_37B_tevs_15B___15A_tevs_37A_nTVMVP_20linkr_NZp	This study	pZAG0528
deadTEVP_mTagBFP2	This study	pZAG0559
TEVP_mTagBFP2	This study	pZAG0560

CHAPTER 3 BIBLIOGRAPHY

1. Krzysztoń R, Wan Y, Petreczky J, Balázsi G. Gene-circuit therapy on the horizon: synthetic biology tools for engineered therapeutics. *Acta Biochim Pol.* 2021;68: 377–383. doi:10.18388/abp.2020_5744
2. Riewald M, Ruf W. Science review: role of coagulation protease cascades in sepsis. *Crit Care.* 2003;7: 123–129. doi:10.1186/cc1825
3. Page MJ, Macgillivray RTA, Di Cera E. Determinants of specificity in coagulation proteases. *J Thromb Haemost.* 2005;3: 2401–2408. doi:10.1111/j.1538-7836.2005.01456.x
4. Patthy L. Evolution of the proteases of blood coagulation and fibrinolysis by assembly from modules. *Cell.* 1985;41: 657–663. doi:10.1016/s0092-8674(85)80046-5
5. Liu Z, Chen O, Wall JBJ, Zheng M, Zhou Y, Wang L, et al. Systematic comparison of 2A peptides for cloning multi-genes in a polycistronic vector. *Sci Rep.* 2017;7: 2193. doi:10.1038/s41598-017-02460-2
6. Campagnola G, Peersen O. Co-folding and RNA activation of poliovirus 3C polyprotein precursors. *J Biol Chem.* 2023;299: 105258. doi:10.1016/j.jbc.2023.105258
7. Zimina A, Viktorova EG, Moghimi S, Nchoutmboube J, Belov GA. Interaction of Poliovirus Capsid Proteins with the Cellular Autophagy Pathway. *Viruses.* 2021;13. doi:10.3390/v13081587
8. Li Z, Ma Y, Nan X, Dong H, Tang J, Yin S, et al. Production of virus-like particles of FMDV by 3C protease cleaving precursor polyprotein P1 in vitro. *Appl Microbiol Biotechnol.* 2024;108: 542. doi:10.1007/s00253-024-13376-z
9. Wong HH, Crudgington DRK, Siu L, Sanyal S. Flaviviruses induce ER-specific remodelling of protein synthesis. *PLoS Pathog.* 2024;20: e1012766. doi:10.1371/journal.ppat.1012766
10. The Flaviviruses: Structure, Replication and Evolution. Elsevier; 2003. Available: <https://play.google.com/store/books/details?id=Xgfrv4aksVUC>
11. Andi B, Kumaran D, Kreitler DF, Soares AS, Keereetaweep J, Jakoncic J, et al. Hepatitis C virus NS3/4A inhibitors and other drug-like compounds as covalent binders of SARS-CoV-2 main protease. *Sci Rep.* 2022;12: 12197. doi:10.1038/s41598-022-15930-z

12. Sengar MS, Rahate K, Verma M. Darunavir: A Versatile Protease Inhibitor against Microbial Infections. *Curr Drug Discov Technol*. 2025. doi:10.2174/0115701638336144250331174407
13. Kan J-Y, Chang Y-J, Lai H-C, Lin H-H, Chiu S-W, Hung P-Y, et al. Darunavir inhibits dengue virus replication by targeting the hydrophobic pocket of the envelope protein. *Biochem Pharmacol*. 2025;235: 116839. doi:10.1016/j.bcp.2025.116839
14. Denard CA, Paresi C, Yaghi R, McGinnis N, Bennett Z, Yi L, et al. YESS 2.0, a Tunable Platform for Enzyme Evolution, Yields Highly Active TEV Protease Variants. *ACS Synth Biol*. 2021;10: 63–71. doi:10.1021/acssynbio.0c00452
15. Sanchez MI, Ting AY. Directed evolution improves the catalytic efficiency of TEV protease. *Nat Methods*. 2020;17: 167–174. doi:10.1038/s41592-019-0665-7
16. McIlwain DR, Berger T, Mak TW. Caspase functions in cell death and disease. *Cold Spring Harb Perspect Biol*. 2013;5: a008656. doi:10.1101/cshperspect.a008656
17. Kumar S. Caspase function in programmed cell death. *Cell Death Differ*. 2007;14: 32–43. doi:10.1038/sj.cdd.4402060
18. Stein V, Alexandrov K. Protease-based synthetic sensing and signal amplification. *Proc Natl Acad Sci U S A*. 2014;111: 15934–15939. doi:10.1073/pnas.1405220111
19. Oakes BL, Fellmann C, Rishi H, Taylor KL, Ren SM, Nadler DC, et al. CRISPR-Cas9 circular permutants as programmable scaffolds for genome modification. *Cell*. 2019;176: 254–267.e16. doi:10.1016/j.cell.2018.11.052
20. Chen Z, Boyken SE, Jia M, Busch F, Flores-Solis D, Bick MJ, et al. Programmable design of orthogonal protein heterodimers. *Nature*. 2018;565: 106. doi:10.1038/s41586-018-0802-y
21. Fink T, Lonžarić J, Praznik A, Plaper T, Merljak E, Leben K, et al. Design of fast proteolysis-based signaling and logic circuits in mammalian cells. *Nature chemical biology*. 2019;15. doi:10.1038/s41589-018-0181-6
22. Vlahos AE, Kang J, Aldrete CA, Zhu R, Chong LS, Elowitz MB, et al. Protease-controlled secretion and display of intercellular signals. *Nat Commun*. 2022;13: 912. doi:10.1038/s41467-022-28623-y

23. To T-L, Piggott BJ, Makhijani K, Yu D, Jan YN, Shu X. Rationally designed fluorogenic protease reporter visualizes spatiotemporal dynamics of apoptosis in vivo. *Proc Natl Acad Sci U S A*. 2015;112: 3338–3343. doi:10.1073/pnas.1502857112

Chapter 4

SENSE-AMPLIFY-KILL CIRCUITS

4.1 Summary

We finally have all the components necessary to ask: can sense-amplify-kill therapeutic circuits detect mutant Ras and specifically trigger cell death?

Here, we engineered synthetic protein circuits that couple Ras sensing to apoptosis or pyroptosis and deliver them as mRNAs encapsulated in lipid nanoparticles (LNPs). These circuits selectively eliminated Ras-mutant human cancer cells *in vitro* while sparing wild-type cells, and induced minimal gene expression changes compared to targeted drugs. In mouse models of liver cancer, therapeutic circuits prevented tumor formation and eliminated established tumors when delivered systemically. Circuits also outperformed small-molecule Ras inhibitors in eliminating drug-resistant and non-Ras-addicted cancer cells, and were less prone to acquired resistance in a Ras mutant cell line MIA PaCa2. Together, these findings demonstrate that therapeutic circuits can provide a potent, selective, and durable strategy for targeting Ras-driven cancers.

4.2 Introduction

Ras mutations are among the most common and consequential genetic alterations in human cancer[1–4]. Oncogenic variants in KRAS, NRAS, and HRAS drive a wide range of solid tumors, including nearly all pancreatic cancers[5,6], over 40% of colorectal cancers[4,7–10], and a significant fraction of non-small cell lung (NSCLC) cancers[10–12]. These mutations confer persistent activation of the Ras small GTPase protein, locking cells into proliferative and survival programs. Despite the clear clinical importance of Ras as a target, most Ras-driven cancers remain untreatable by existing precision medicines[10,13–16]. Pancreatic ductal adenocarcinoma (PDAC), for example, is almost universally Ras-mutant and carries a 5-year survival rate of less than 10%.

More effective strategies for selectively eliminating Ras-mutant cells are urgently needed.

Therapeutic strategies for Ras have largely focused on designing small molecules to inhibit Ras activity or its downstream effectors. These include covalent inhibitors that bind mutant KRAS^{G12C}, as well as pan-Ras and MAPK pathway inhibitors currently under development[10,11,17,18]. While some of these agents have achieved clinical approval, their therapeutic benefit has been modest. Tumor responses are often partial, resistance emerges rapidly, and healthy tissues with physiologic Ras signaling can be affected, leading to toxicity. Furthermore, many Ras-mutant tumors are not “addicted” to Ras signaling in the same way that, for example, BCR-ABL-driven leukemias are addicted to ABL kinase activity[19]. In these contexts, targeting Ras often fails to induce durable cell killing. These limitations highlight the need to move beyond inhibition and toward more direct, programmable strategies that convert Ras activity into a clear and irreversible therapeutic response.

Here, with both a suite of sensor and signal amplifiers in hand, we will complete the modality for targeting Ras-mutant cancer: programmable protein circuits that detect oncogenic Ras signaling and directly trigger cell death. Rather than modulating downstream pathways, these circuits couple intracellular Ras sensing to precise effector outputs, such as apoptosis or pyroptosis. Delivered using lipid nanoparticles (LNPs), this approach allows for efficient and transient expression of therapeutic circuits inside of living cells.

4.3 Results

4.3.1 Circuits potently and selectively eliminate Ras-mutant cancer cells

To enable selective cancer cell killing in response to mutant Ras sensing, a complete therapeutic circuit must (1) be efficiently delivered to both healthy and cancer cells, and (2) couple Ras sensors to tightly controlled effectors of cell death. We confirmed that an

existing LNP formulation [20,21] could efficiently deliver *in vitro* transcribed mRNA to human cells in culture, and that protein expression levels are quantitatively tunable by LNP concentrations (**fig. S4.1A-B, Methods**).

We first couple mutant Ras sensors to effectors of apoptosis, a precise and tightly regulated mode of cell death. Specifically, we separately encapsulated mRNAs encoding the $v2-s$ sensor and a TEVP-activatable, membrane-localized caspase-3 effector (Casp-3) that conditionally triggers apoptosis (**Fig. 4.1A**). We delivered different concentrations of the two mRNA-LNP components to human cancer cell lines and analyzed cell viability 3-5 days post-treatment. Both the sensor and the effector were well tolerated across a wide dosage regime when delivered individually (**Fig. 4.1B-C**). Strikingly, co-delivery of the sensor and caspase effector induced potent, near-complete, and dose-dependent killing in Ras-mutant cancer cell lines, while sparing Ras wild-type cells (**Fig. 4.1B-C**). These results demonstrate that therapeutic circuits can selectively kill human Ras-mutant cancer cells.

To broaden the effects of therapeutic circuits beyond transfected cells, we also coupled Ras sensing to effectors of pyroptosis, an immunogenic form of cell death. Indeed, current mRNA delivery methods cannot penetrate all tumor cells *in vivo*. While partial tumor clearance may offer some therapeutic benefit, extending circuit-mediated killing to non-transfected cancer cells would be advantageous. Unlike apoptosis, pyroptosis releases inflammatory cytokines that can recruit the immune system, inducing non-cell autonomous tumor clearance even when triggered in a minority of cancer cells [22,23]. To test conditional activation of pyroptosis, we co-delivered the $v2-s$ Ras sensor with a cleavage activatable gasdermin, the natural cell death effector of the pyroptosis program. As above, these components induced negligible background cell death when delivered alone, but potently and selectively eliminated Ras-mutant human cancer cells when co-delivered as a complete therapeutic circuit (**Fig. 4.1B**). Together, these results show that therapeutic circuits delivered as mRNA in LNPs can effectively target Ras-mutant cancer cells with two complementary cell death programs.

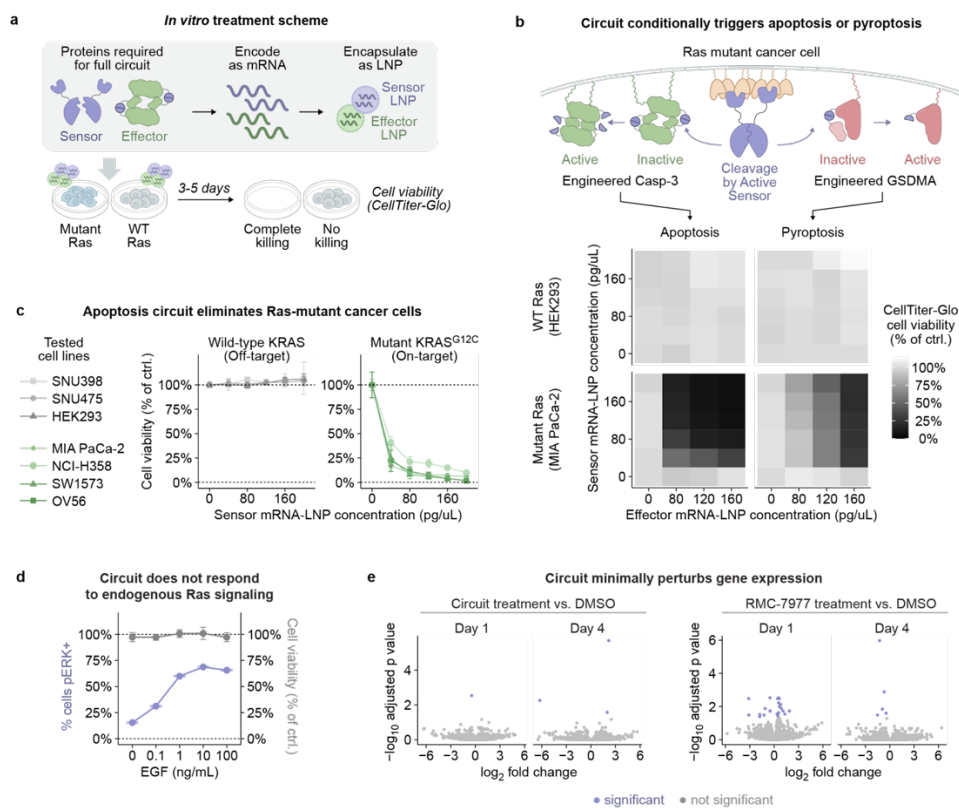


Fig. 4.1. Therapeutic circuits potently and selectively eliminate Ras-mutant cancer cells. (A) *In vitro* treatment scheme for therapeutic circuits. mRNA-encoded sensors and effectors were encapsulated in lipid nanoparticles (LNPs) and delivered to cancer cells. Cell viability was measured 3-5 days post-treatment using CellTiter-Glo. (B) Engineered sensor *v2-s* conditionally activates apoptosis (via engineered Casp-3) or pyroptosis (via engineered Gasdermin A, GSDMA) effectors in cells harboring mutant Ras. Heatmaps show selective killing of mutant Ras-expressing (MIA PaCa-2) vs. wild-type (HEK293) cells across different sensor and effector mRNA-LNP concentrations ($n = 3$ replicates, mean cell viability depicted). (C) Circuit composed of sensor *v2-s* and engineered Casp-3 selectively eliminates cancer cells harboring mutant

Ras (MIA PaCa-2, NCI-H358, SW1573, OV56; all KRAS^{G12C}), but spares wild-type Ras-expressing control cell lines (SNU398, SNU475, HEK293; all KRAS^{WT}). Viability expressed as luminescence normalized to no sensor controls; error bars represent mean \pm sd ($n=3$ replicates). **(D)** Circuit responsiveness to endogenous Ras signaling induced by EGF stimulation. Ras activation was quantified as the percentage of pERK-positive cells measured by antibody staining and flow cytometry. Error bars for pERK measurements represent 95% confidence intervals derived from bootstrapping (1,000 iterations). Cell viability was assayed with CellTiter-Glo; error bars represent mean \pm sd ($n=2$ replicates). **(E)** RNA-seq on HEK293 cells treated with RMC-7977 or circuit at day 1 or day 4 post-treatment.

4.3.2 Circuits do not respond to endogenous Ras signaling or perturb gene expression

A potential safety concern is off-target activation of circuits in wild-type cells engaged in normal Ras signaling. To test for such effects, we transfected mRNA-LNP circuits in HEK293 cells with or without Ras stimulation by epidermal growth factor (EGF). EGF treatment rapidly induced activation of the RAS-MEK-ERK pathway [24], with ERK phosphorylation detectable within 15 minutes, as expected [25] (**Fig. 4.1D**). Nevertheless, the transfected cells exhibited no detectable cell death, even at saturating EGF concentrations. This ability to discriminate between wild-type and mutant Ras signaling may reflect a difference in Ras activation dynamics, with cancer cells exhibiting more sustained Ras activity than wild-type cells, where activation may be adaptive or oscillatory [24,26,27]. These results demonstrate a safety feature of the sense-kill circuits and help explain their mutant specificity.

Another potential safety concern is that transient expression of circuit components could potentially perturb cell states. Using RNA-seq, we analyzed the gene expression profile of

HEK293 cells following treatment with either the mRNA-LNP circuit or the Ras targeting inhibitors Sotorasib and RMC-7977. 24h after treatment, the mRNA-LNP circuit yielded only one differentially expressed gene (Benjamini-Hochberg-adjusted $p < 0.05$; **Fig. 4.1E**, **fig. S4.1C**). By contrast, RMC-7977 and Sotorasib differentially regulated 24 and 6 genes, respectively. In particular, RMC-7977 downregulated known transcriptional targets of the RAS-MAPK pathway such as DUSP6 ($p = 0.0041$) or ETV5 ($p = 0.003$), consistent with previous results [28] and its role as a pan-Ras signaling inhibitor, while the circuit did not significantly affect these genes. By 4 days post-treatment, gene expression in all three conditions had largely returned to baseline. These results suggest that mRNA-LNP circuits minimally perturb healthy cells.

4.3.3 Circuits prevent and treat induced liver tumors *in vivo*

Having demonstrated specific targeting in cell culture, we next asked whether therapeutic circuits could function *in vivo*. The liver represents an ideal context to test circuits *in vivo* for two reasons. First, existing LNP formulations can efficiently transfect the liver [20,29,30]. Second, the liver is the primary metastatic site for many Ras-driven cancers with high unmet clinical need [7–9], as well as the primary site for Ras-driven cholangiocarcinomas [31].

Liver tumors develop in complex microenvironments, with vasculature, immune cells, and extracellular matrix influencing cancer growth. To recapitulate these features, we used an established autochthonous liver cancer model in immunocompetent mice. In this model, hydrodynamic tail vein injection (HDT) is used to transfect hepatocytes with DNA encoding the oncogenic *NRAS*^{G12V} Ras variant, an shRNA targeting TP53 (shTP53), and the Sleeping Beauty (SB100) transposase for stable genomic integration and sustained expression. The model generates aggressive and multifocal liver cancers that advance to late-stage disease within five weeks after induction [32–34].

Using this model, we first asked whether circuits could function *in vivo*, independently of potential delivery limitations. To address this question, DNA-encoded circuits were co-administered with the tumor-inducing agents to allow tumor initiation and circuit expression to occur largely in the same liver cells (**Fig. 4.2A**). We used circuits that incorporated the *vI* sensor, as experiments were conducted before the improved sensor variants were developed, and the apoptosis cell death effector, as tumor induction was largely restricted to circuit-expressing cells. Further, we included circuit variants with or without the amplifier. In one mouse cohort, we let tumors develop for five weeks, terminated the experiment, and measured total surface tumor areas and liver-to-body weight ratios, a standard measure of tumor burden in hydrodynamic liver tumor models (**Fig. 4.2A, Methods**). In a separate mouse cohort, we tracked survival to determine the durability of tumor suppression (**Fig. 4.2A, Methods**).

Mice that received no treatment showed robust, multifocal tumor formation (**Fig. 4.2B, fig. S4.2**). Co-delivery of the sensor and cell death effector significantly, but incompletely, reduced tumor burden, as assessed by total surface tumor area ($p = 4.1 \times 10^{-3}$) and liver-to-body weight ratios ($p = 2.8 \times 10^{-3}$; **Fig. 4.2B, fig. S4.2, fig. S4.3A-B**). The same condition extended median survival from 42 days (in untreated animals) to 59 days ($p = 7 \times 10^{-4}$), but did not eliminate tumor development (**Fig. 4.2B**). Remarkably, inclusion of the amplifier module transformed this partial response into near-complete tumor suppression. Mice that received the complete sense-amplify-kill circuit showed no detectable surface tumors and exhibited liver-to-body weight ratios comparable to those of healthy animals (**Fig. 4.2B, fig. S4.2, fig. S4.3A-B**). In the parallel cohort, all mice treated with the sense-amplify-kill circuit survived beyond 145 days, at which time the experiment was terminated (**Fig. 4.2B**, $p = 1 \times 10^{-4}$ for comparison to untreated). Overall, these results demonstrated that co-delivered therapeutic circuits can prevent the formation of induced mouse liver tumors *in vivo*.

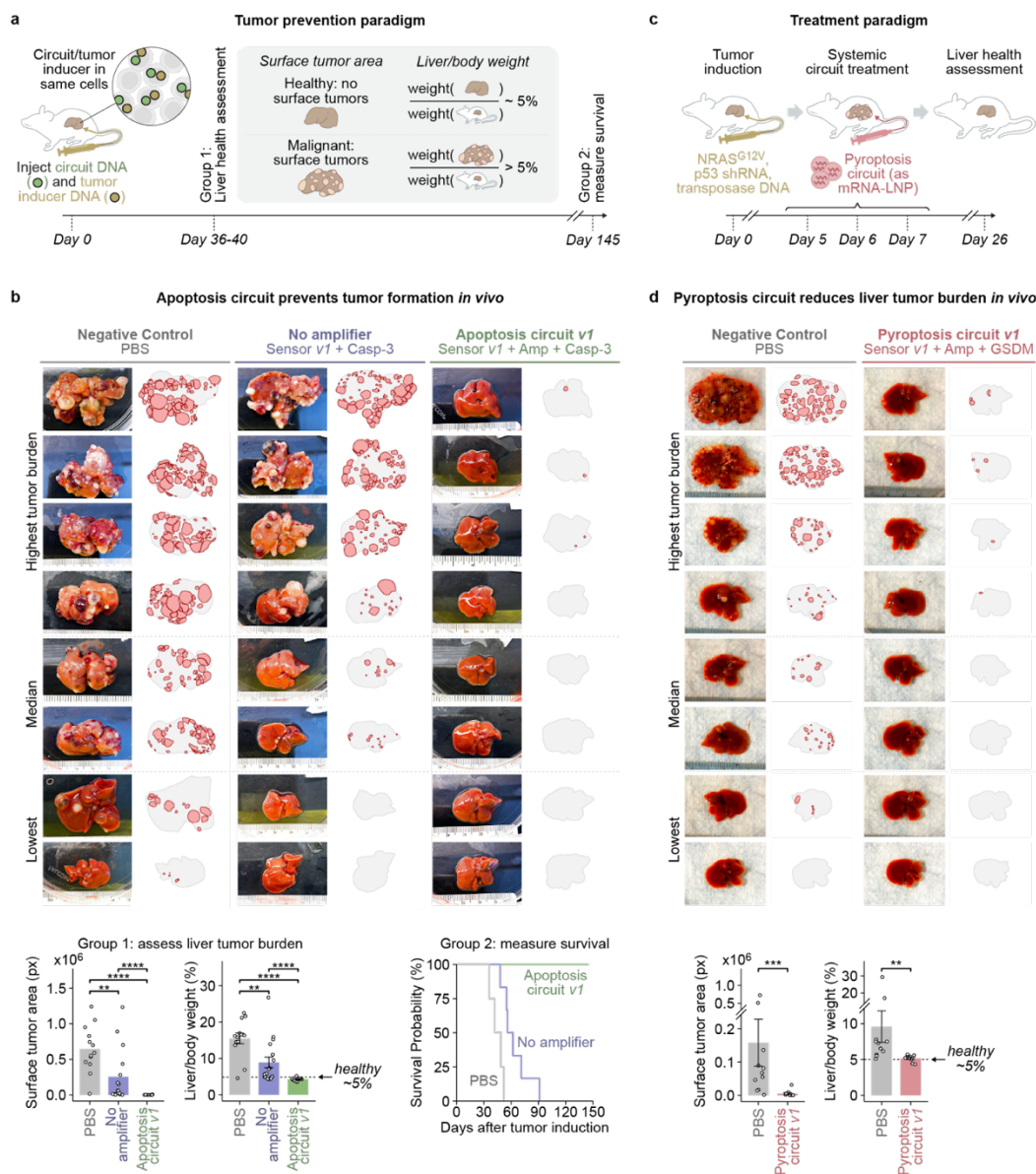


Fig. 4.2. Therapeutic circuits prevent and treat liver tumors *in vivo*. (A) Circuit composed of v1 sensor, amplifier, and engineered Casp-3 prevents tumor formation *in vivo*. Tumors were generated by co-administration of plasmids encoding NRAS^{G12V}, TP53 shRNA, and a sleeping beauty transposase via hydrodynamic tail

vein injection (HDT). Liver tumor burden was quantified using two independent metrics: (1) surface tumor area, manually annotated following blinded evaluation, and (2) liver-to-body weight ratio, a standard quantitative measure in hydrodynamic liver tumor models. **(B) Top:** mouse livers ($n = 13-16$ female mice per condition) extracted 36-40 days after tumor induction. Liver images and manually annotated surface tumor nodules (red) are displayed side-by-side. *Bottom left:* quantification of total surface tumor area (blinded manual annotation of tumor nodules). Bars depict mean tumor surface area (px) \pm se (error bars). Individual data points denote accumulated surface tumor area of individual animals from anterior and posterior views. Adjusted p value = 4.1×10^{-3} for PBS vs. no amplifier; 3.2×10^{-6} for PBS vs. full circuit; 3.2×10^{-6} for no amplifier vs. full circuit (pairwise Mann-Whitney U tests with Benjamini-Hochberg (BH) correction). *Bottom middle:* bars depict mean liver/body weight ratio (%) \pm se (error bars). Data points denote liver/body weight ratio of individual animals. Adjusted p value = 2.8×10^{-3} for PBS vs. no amplifier; 3.5×10^{-7} for PBS vs. full circuit; 1.5×10^{-5} for no amplifier vs. full circuit (pairwise Mann-Whitney U tests with BH correction). *Bottom right:* overall survival depicted as Kaplan-Meier curves (group 2; $n = 7-10$ male mice per condition). Median survival 42 days for PBS; 59 days for no amplifier; 145 days (termination of experiment) for full circuit. P value = 7×10^{-4} (***) for PBS vs. no amplifier; 1×10^{-4} (****) for PBS vs. full circuit; 1×10^{-4} (****) for no amplifier vs. full circuit (log-rank test, all p values significant after Bonferri correction). **(C)** *In vivo* treatment scheme for therapeutic circuits. mRNA-encoded sensors and effectors were encapsulated in lipid nanoparticles (LNPs) and intravenously administered on days 5, 6, and 7 following tumor induction. On day 26, mice were sacrificed and livers were collected for evaluation of tumor burden. **(D)** Systemic intravenous delivery of pyroptosis circuit νI (νI sensor, amplifier, sensor-activatable gasdermin D; GSDMD) induced robust anti-tumor activity ($n = 10-11$ female mice per condition). P value = 0.00055 when comparing distribution of surface tumor areas between PBS and circuit νI ; 0.00078 when comparing distribution of liver/body weight ratios (Mann-Whitney U test). Bars depict mean \pm se (error bars).

Individual data points denote mean surface tumor area (px) and liver/body weight ratios (%), respectively.

We next considered a more challenging treatment scenario (**Fig. 4.2C**). Rather than co-delivering circuits with tumor-initiating agents, we initiated tumor formation (day 0) using the same procedure as above, and then allowed tumors to develop for five days before systemically administering the therapeutic circuits as mRNA-LNP in three doses, on days 5, 6, and 7. On day 25, we sacrificed mice and harvested livers for further analysis. In this case, because the circuits are unlikely to be delivered to the majority of cancer cells, we replaced the apoptosis effector with the pyroptosis effector as output. Thus, the circuits in this experiment consisted of the *vI* sensor, amplifier, and gasdermin pyroptosis effector.

Compared to PBS-treated mice, circuit-treated animals showed near-complete tumor clearance (**Fig. 4.2D**, **fig. S4.3C-D**, **fig. S4.4**). In fact, the livers of circuit-treated animals were almost completely free of surface tumor nodules (p value = 0.00055 compared to the negative control group). The treated animals also exhibited liver-to-body weight ratios comparable to those of healthy animals (p value = 0.00078 compared to negative control group). Thus, circuits delivered systemically using mRNA-LNPs are capable of eliminating previously initiated Ras-driven mouse liver tumors. This result was particularly striking given that this multifocal cancer model is known to be challenging to treat [34], and that this result was obtained using the less optimized sensor.

4.3.4 Circuits kill drug-resistant cells

Both intrinsic and acquired resistance can limit the efficacy of Ras inhibitors (**Fig. 4.3A**) [17,18]. Intrinsic resistance can be assayed by the initial response of Ras-mutant cells to treatment [15]. In contrast, acquired resistance arises when initially sensitive cells adapt over time, either by losing Ras dependency or by activating compensatory pathways to circumvent Ras inhibition [10,15,17]. It can be observed through the gradual emergence of resistant cells after extended treatment [16]. We reasoned that therapeutic circuits, by directly rewiring mutant Ras sensing to cell death, could provide fewer opportunities for both types of resistance (**Fig. 4.3A**). To test this hypothesis, we directly compared the performance of the mRNA-LNP-delivered apoptosis circuit ($v2$ -s sensor, caspase effector) to two clinically relevant small-molecule Ras inhibitors: Sotorasib, an approved KRAS^{G12C} inhibitor [18,35], and RMC-7977, a pan-Ras inhibitor with a related molecule currently under clinical evaluation [28,36].

To assay for intrinsic resistance, we compared the responses of KRAS^{G12C}-mutant MIA PaCa-2 cells to either circuit or drugs. Sotorasib and RMC-7977 reduced cell viability in a dose-dependent manner by up to $74.8 \pm 0.5\%$ or $86.8 \pm 0.3\%$, respectively, but neither drug achieved complete cell elimination, even at saturating concentrations (**Fig. 4.3B**). In contrast, the circuit achieved near complete elimination of all cells ($97.1 \pm 0.1\%$, **Fig. 4.3B**). Also, while the potency of the drugs declined rapidly with increasing cell plating density, circuit potency remained constant (**fig. S4.5A**).

In a complementary experiment, we used microscopy to compare drug and circuit effects on co-cultured target (MIA PaCa-2) and non-target (Ras wild-type HEK293) cells, engineered to stably express GFP and mRuby3 markers, respectively. Five days after treatment, the chemotherapeutic agent Paclitaxel produced potent but incomplete and non-specific clearance of both cell types (**Fig. 4.3C**). Sotorasib and RMC-7977 disproportionately reduced the size of the Ras-mutant cell population, but failed to eliminate them entirely, leaving behind visible colonies of Ras-mutant cells (**Fig. 4.3C**). By contrast, the circuit completely cleared Ras-mutant, but not wild-type Ras cells (**Fig.**

4.3C). Together, these results suggest that circuits can be more potent and specific than targeted therapies and chemotherapy.

Notably, circuits were effective against Ras mutant cells regardless of whether they exhibited oncogene addiction (**Fig. 4.3D**). We tested three Ras-mutant cell lines that do not exhibit Ras addiction: SW1573 (lung, KRAS^{G12C}), OV56 (ovary, KRAS^{G12C}), and PANC-1 (pancreas, KRAS^{G12D}). While these cells exhibited weak responses to drugs, they remained fully sensitive to the circuit (**Fig. 4.3D**). The circuits also produced durable effects. We analyzed the response of non-Ras addicted SW1573 cells to a single dose of drug or circuit over 1 week of continuous culture. The circuit, but not the drugs, durably eliminated these cells and prevented their recovery within this period (**fig. S4.5B**).

Acquired resistance limits the clinical efficacy of targeted therapies such as Sotorasib [17,18]. To quantitatively compare the susceptibility of MIA PaCa-2 cells to acquired resistance under Sotorasib or circuit treatment, we performed three rounds of five-day selection at the EC₇₀ of each treatment. We then challenged cells with another round of the same respective treatment to assess resistance (**Fig. 4.3E**). Consistent with preclinical models and patient outcomes, Ras mutant MIA PaCa-2 cells rapidly acquired resistance, requiring 30-fold higher drug concentrations to reach the same cell killing efficiency (EC₃₀) post-selection compared to pre-selection (**Fig. 4.3E**). In contrast, circuit selection increased circuit EC₃₀ by only 1.3-fold. Moreover, Sotorasib's maximum killing efficiency dropped from ~75% in pre-selection cells to ~50% in post-selection cells, whereas the circuit maintained over 98% maximum efficiency post-selection (**Fig. 4.3E**). These results indicate that MIA PaCa-2 cells are less susceptible to acquired resistance to the circuit compared to Sotorasib.

Finally, given the clinical challenge of Sotorasib resistance, we wondered whether cells with acquired Sotorasib resistance (generated above) would also exhibit resistance to the circuit, or *vice versa* (**Fig. 4.3E**). Interestingly, Sotorasib-resistant cells required 2.5-fold lower concentrations of circuit mRNA-LNP to achieve the same killing efficiency (EC₃₀) as non-resistant cells (**Fig. 4.3E**). We reasoned that this effect could be related to the known

resistance mechanisms of increased Ras expression (or amplification), either of which could increase sensitivity to the circuit. To test this hypothesis, we transiently overexpressed KRAS^{G12C} in MIA PaCa-2 cells and treated these cells with either Sotorasib or the circuit. Indeed, transient KRAS^{G12C} overexpression slightly increased resistance to Sotorasib but enhanced sensitivity to the circuit (**fig. S4.5C**). Together, these results highlight a fundamental difference in the resistance profile of drug and circuit-based therapies and suggest that future therapeutic circuits could help treat patients resistant to Ras-inhibiting drugs.

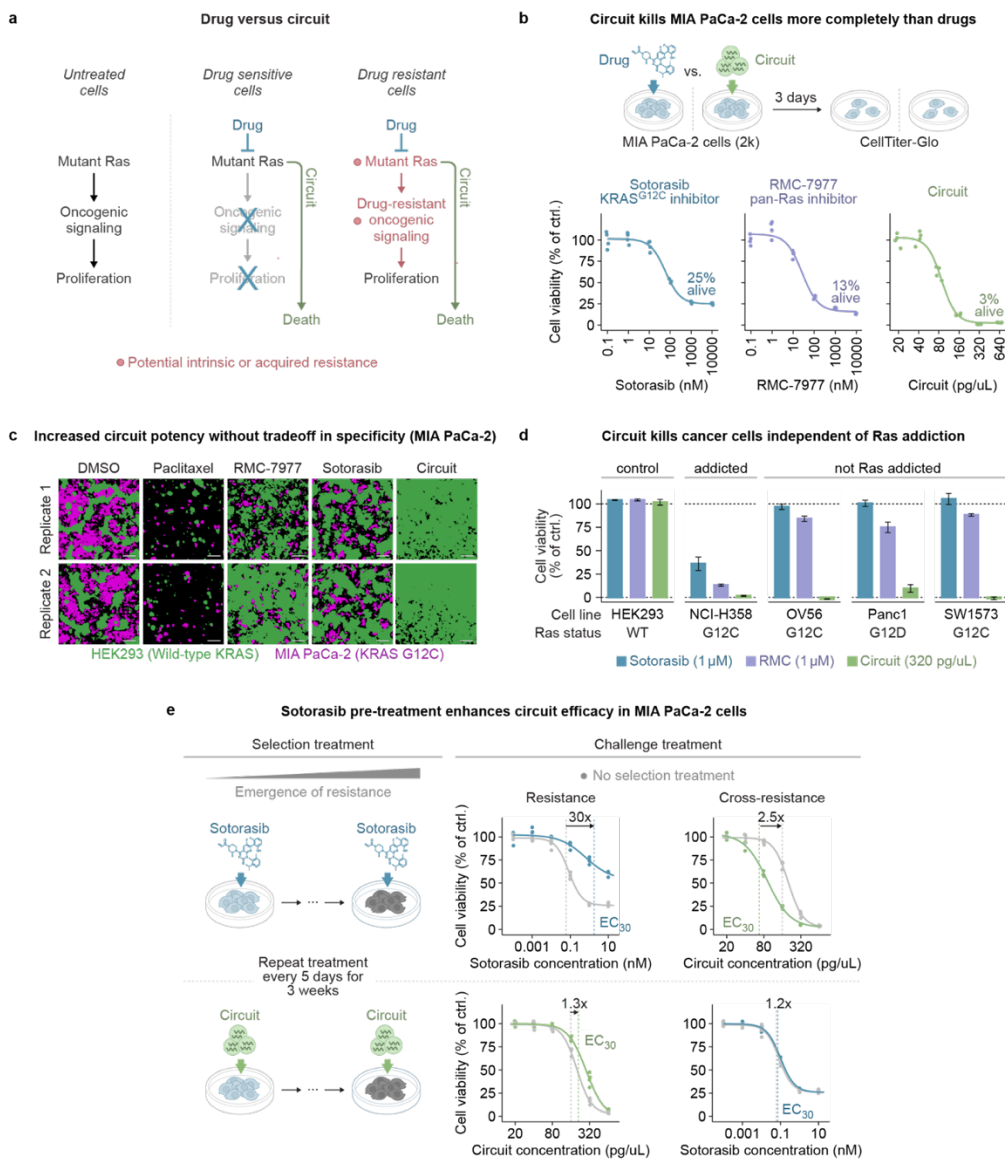


Fig. 4.3. Circuits are less susceptible to intrinsic and acquired resistance compared to Ras-targeting drugs. (A) Circuits can directly induce cancer cell death, potentially minimizing susceptibility to resistance mechanisms that limit targeted therapies. Circuits used in this Fig. were composed of sensor $v2-s$ and Casp-3. If not specified otherwise, circuit concentrations denote accumulated

amounts of sensor $v2-s$ and Casp-3 added at a 1:1 ratio. **(B)** Dose-response curves for Ras inhibitors (Sotorasib, RMC-7977) and circuit. Viability measured after 3 days (CellTiter-Glo, mean \pm sd, $n = 3-4$). Curves were fitted with a four-parameter log-logistic model (**Methods**). **(C)** Co-culture of MIA PaCa-2 (KRAS^{G12C}) and HEK293 (wild-type KRAS) cells stably expressing GFP and mRuby3, respectively. Cells were treated with saturating concentrations of Paclitaxel (30 μ M), RMC-7977 (1 μ M), Sotorasib (1 μ M), or the therapeutic circuit (150 pg/ μ L Casp-3 and 100 pg/ μ L sensor $v2-s$). Fluorescence images were acquired on day 5. Scale bar, 200 μ m. **(D)** Efficacy comparison between circuits and Ras inhibitors in cell lines that differ in Ras addiction. Dashed lines represent 0% and 100% cell viability, respectively. **(E)** Repeated exposure to Sotorasib or the therapeutic circuit alters subsequent treatment responsiveness in MIA PaCa-2 cells. Cells were treated every 5 days for 3 weeks, then challenged with both Sotorasib and circuit components. Changes in EC₃₀ values reflect acquired resistance or sensitization. Data are presented as fold-change in EC₃₀ (mean \pm sd, $n = 4$ replicates). The sum-of-squares F-test was used to determine if selection treatment yields significantly altered dose-response curves from cells that did not undergo selection treatment: p value ≈ 0 , F value = 141 for Sotorasib selection and challenge treatment; p value = 5×10^{-14} , F value = 43 for circuit selection and challenge treatment; p value ≈ 0 , F value = 235 for Sotorasib selection and circuit challenge treatment; p value = 0.11, F value = 2 for circuit selection and Sotorasib challenge treatment.

4.4 Supplementary Figures

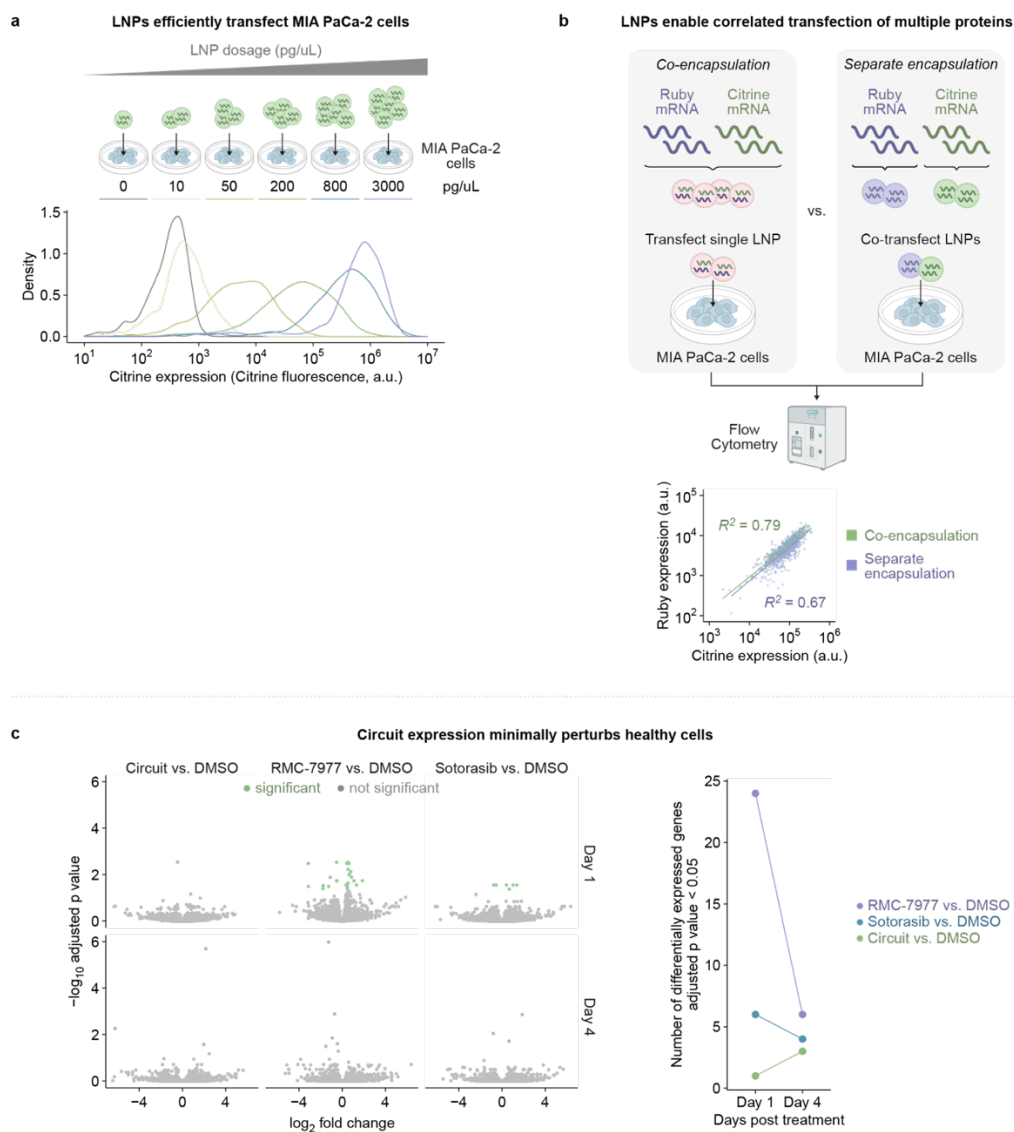


Fig. S4.1. mRNA Delivery via LNP and treatment effects on transcriptome. (A) LNPs enable titratable, near-complete transfection of MIA PaCa-2 cells with Citrine

mRNA (as measured by flow cytometry). **(B)** LNPs enable correlated transfection of multiple proteins. Co-encapsulation of mRuby3 and Citrine mRNAs in a single LNP results (administration of 300 pg/uL mRNA-LNP per well) in comparable correlation between the two proteins ($R^2 = 0.79$) compared to co-transfection of separately LNP-encapsulated mRuby3 and Citrine mRNAs ($R^2 = 0.67$, administration of 150 pg/uL mRNA-LNP per mRNA; as measured by flow cytometry). R^2 denotes squared correlation coefficient. **(C)** Volcano plot of bulk RNA-sequencing from HEK293 cells treated with drugs and circuit for 1 or 4 days. RMC-7977 induced more differential gene expression than Sotorasib or the circuit at day 1. By day 4, transcriptomic profiles largely returned to baseline.

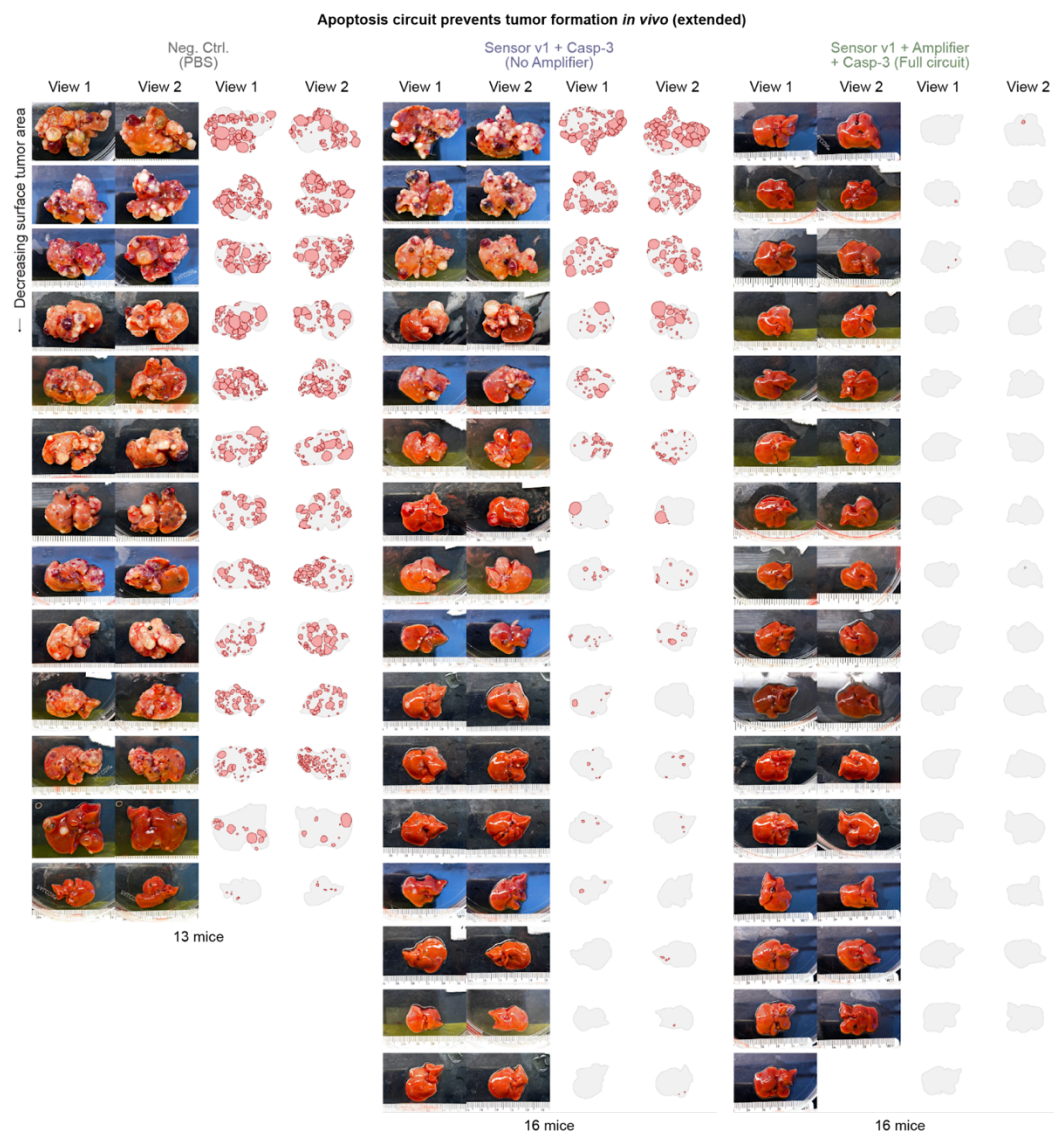


Fig. S4.2. *In vivo* tumor prevention. *In vivo* co-delivery of tumor inducing agents and circuits for evaluation of tumor prevention. Hydrodynamic tail vein injection was used to efficiently transfect hepatocytes in mice. Tumor-inducing agents were co-delivered with circuit plasmid DNA. Mice receiving no circuit developed multifocal, aggressive liver tumors. Inclusion of Sensor *v1* and Casp-3 provided partial inhibition of tumor initiation. The full circuit, including the amplifier module, completely

blocked tumor formation. Surface tumor nodules were manually annotated. View 1 and 2 denote front and back view of livers.

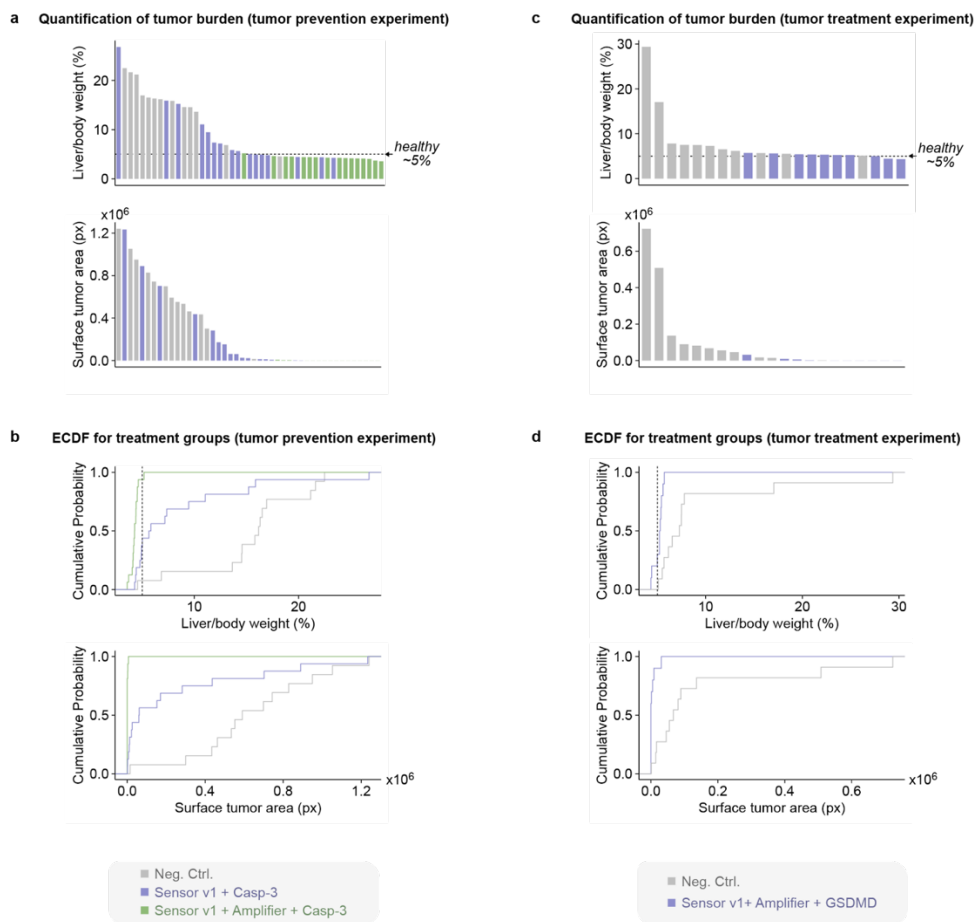


Fig. S4.3. Quantification of effects in tumor prevention and mRNA-LNP treatment experiments. (A and C) Distribution of liver tumor burden across treatment groups. *Top*: liver-to-body weight ratio. *Bottom*: total tumor surface area. **(B and D)** Empirical cumulative distribution function (ECDF) of tumor burden for each treatment group.

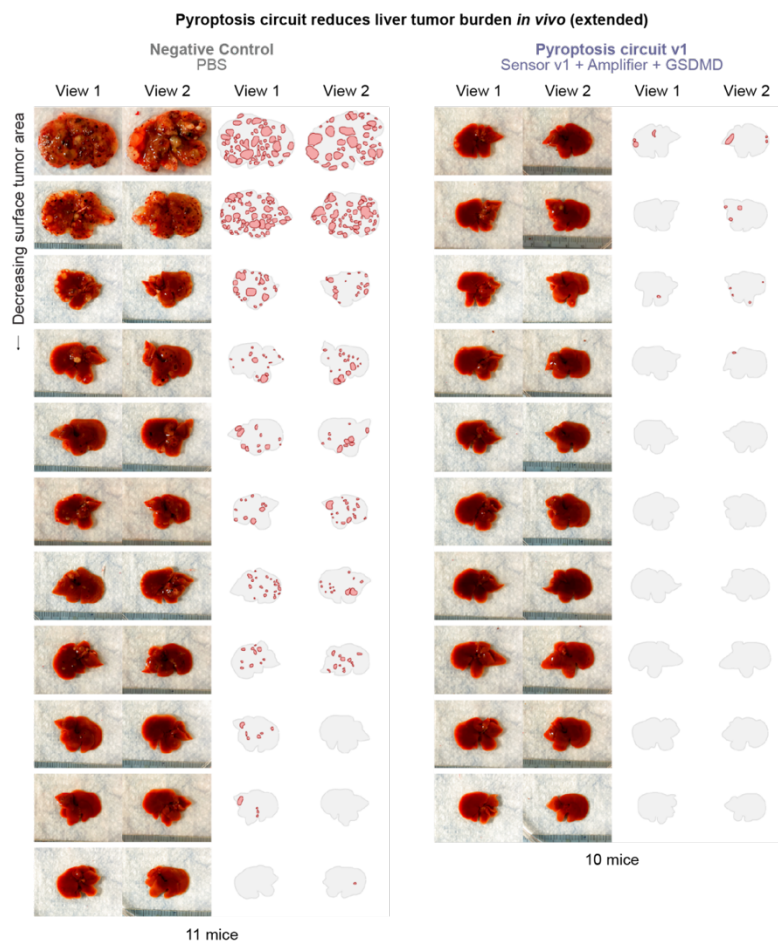


Fig. S4.4. Gross images of mouse livers after mRNA-LNP treatment. Mice were first induced with tumor-initiating agents, and tumors were allowed to develop before treatment. PBS-treated animals developed more extensive tumors than those receiving the full circuit, indicating therapeutic efficacy. Surface tumor nodules were manually annotated. View 1 and 2 denote front and back view of livers.

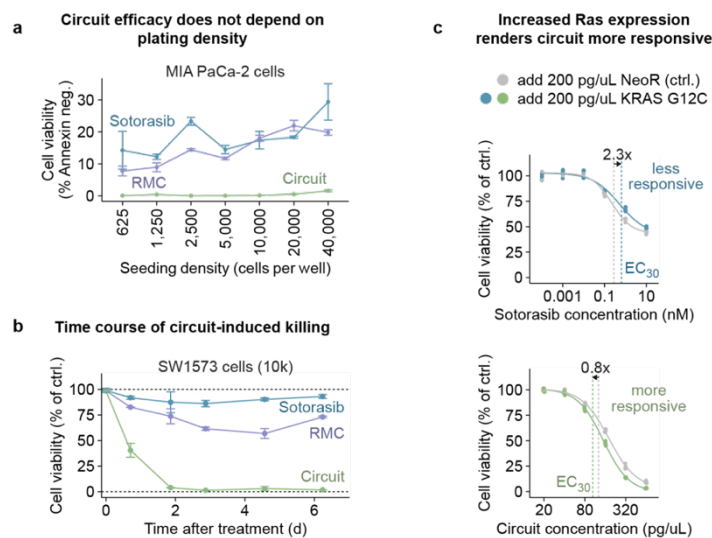


Fig. S4.5. Comparison of circuit and Ras inhibitors Sotorasib and RMC-7977.

(A) Killing efficacy of the mRNA-LNP circuit ($v2-s$ sensor, Casp-3) is independent of plating density in MIA PaCa-2 ($KRAS^{G12C}$) cells stably expressing GFP. Viability (mean \pm sd, $n = 3$ replicates) was determined by flow cytometry; live cells were defined as GFP high ($>10^5$ a.u.) and Annexin V low ($<10^4$ a.u.). **(B)** The circuit induces sustained depletion of SW1573 cells over 7 days, while Sotorasib- and RMC-7977-treated populations rebound after 3-5 days. Viability was measured using CellTiter-Glo (mean \pm sd, $n = 2$ replicates). **(C)** Transient Ras overexpression enhances circuit sensitivity and reduces Sotorasib efficacy. MIA PaCa-2 cells were co-treated with 200 pg/ μ L $KRAS^{G12C}$ or NeoR (control) mRNA-LNP and either Sotorasib or the circuit ($v2-s$ sensor, Casp-3). Viability (mean, $n = 4$ replicates) was assessed; dotted lines indicate EC_{30} values, and fold-change in response due to Ras overexpression is annotated.

4.5 Methods

Plasmid construction

Plasmids were generated via Gibson Assembly (NEBuilder HiFi DNA Assembly Master Mix; New England BioLabs) or KLD cloning (T4 Polynucleotide Kinase, T4 DNA Ligase, DpnI, T4 DNA Ligase Buffer; Thermo Scientific). Gene fragments were sourced from Twist Bioscience or Integrated DNA Technologies (IDT), or PCR-amplified from existing laboratory plasmid constructs. IDT synthesized all PCR primers. Plasmids were purified (QIAprep Spin Miniprep Kit or Qiacube machine; Qiagen), normalized (Thermo Scientific NanoDrop 8000), and sequence-verified (Plasmidsaurus or Genewiz) prior to experimental use.

Tissue culture and cell lines

Most cell lines were obtained from ATCC and cultured under standard conditions (37°C, 5% CO₂, humidified Eppendorf CellXpert C170i incubator). Adherent cells were maintained in Dulbecco's Modified Eagle Media (DMEM; Thermo Fisher) supplemented with 10% fetal bovine serum (FBS; Avantor), penicillin (1 unit/ml), streptomycin (1 µg/ml), glutamine (2 mM), sodium pyruvate (1 mM), and 1X Minimal Essential Media Non-Essential Amino Acids (all Thermo Fisher). HEK293FT cells were cultured for up to 20 passages, and human cancer cell lines for up to 15 passages, maintaining 10%-90% confluency. Cells were passaged using 0.25% Trypsin-EDTA (Thermo Fisher). Viable cell numbers for seeding densities were determined using Trypan Blue (Invitrogen) and the Countess 3 automated cell counter (Thermo Fisher). Cells were routinely confirmed mycoplasma-free (MycoStrip kit; InvivoGen). Cell lines with stably integrated fluorescent proteins used for microscopy were purchased from FenicsBIO.

Transient transfection

Transient transfections were performed utilizing FuGENE HD (Promega), Lipofectamine 3000 (Thermo Fisher), or LNPs (described below) as transfection agents. Unless otherwise noted, we seeded 10k cells (96-well plate), 200k cells (24-well plate) for FuGENE or LNP transfections, and 275k cells (24-well plate) for Lipofectamine transfections. Cells were reverse-transfected immediately after seeding following manufacturer instructions. For FuGENE transfections, we incubated 1 μ g plasmid DNA with 6 μ l transfection reagent. For FuGENE transfections, 200k cells were transfected with up to 566 ng of DNA. For Lipofectamine transfections, 1.5 μ l Lipofectamine 3000 and 1.5 μ l reagent P3000 were used with a total of 500 ng DNA to transfect an equivalent of 275k cells. The total amount of plasmid DNA applied in each transfection was scaled according to seeding densities.

Flow cytometry

Cells were collected two days post-transient transfection for flow cytometry, filtered through a 40- μ m cell strainer, and analyzed by flow cytometry (CytoFLEX S flow cytometer, Beckman Coulter). Unless otherwise noted, we used FITC-A channel (GFP of iTEVP reporter[37]; excitation 488 nm, emission 525/40 nm; gain of 1), ECD-A channel (mRuby3; excitation 561 nm, emission 610/20 nm; gain of 1), PB450-A channel (mTagBFP2; excitation 405 nm, emission 450/45 nm; gain of 1), and APC-A700-A channel (IFP of iTEVP reporter; excitation 638 nm, emission 712/25; gain of 100). Live cells and singlets were gated using FlowJo (version 10.10, BD Biosciences). iTEVP reporter activation was assessed by calculating the IFP (activation) to GFP (reporter expression) ratio for cells with GFP expression between 10^5 and 10^6 a.u., corresponding to the reporter expression regime with maximal dynamic range. As the reporter construct was always transfected as a separate polytransfection mix, selecting cells with high reporter expression did not bias subsequent analysis steps, *i.e.*, the expression distribution of other constructs (*e.g.*, reporter or ectopic Ras) remained unaffected.

mRNA production

DNA templates containing a 5' T7 promoter sequence followed by the dinucleotide sequence AG were linearized by PCR (Q5 High-Fidelity DNA Polymerase, NEB). A 3' end 120-base pair polyA-tail was added using PCR. The linear DNA templates were purified by Ampure beads or gel purification (Zymoclean Gel DNA Recovery Kit, Zymo). mRNA was subsequently produced via *in vitro* transcription (IVT) using NEB's HiScribe T7 High Yield RNA Synthesis Kit. The IVT reaction mix contained 10X Reaction Buffer (1X final), 1 µg DNA template, 4 mM CleanCap AG (TriLink), 2 µl T7 RNA polymerase mix, and the nucleotides ATP, GTP, CTP, and *N1*-Methyl-Pseudouridine-5'-Triphosphate (TriLink) at a final concentration of 5 mM. After an incubation period of 2 hours at 37 °C, DNase I (NEB) was added and reactions were incubated for another 15 minutes at 37 °C. Finally, mRNA was purified using Zymo's RNA Clean and Concentrator Kit and concentrations were read out by Nanodrop or Qubit RNA High Sensitivity or Broad Range kits. The concentration normalized mRNAs were stored at -80 °C.

Lipid nanoparticle (LNP) mRNA encapsulation

We adopted a previously described 4 component LNP formulation [21] (4A3-SC8, DOPE, Cholesterol, DMG-PEG) that enables transfection of cells in culture and *in vivo*.

To prepare the lipid stock solutions, a full 25 mg tube of 4A3-SC8 compound was dissolved in 167 µL of pure ethanol to yield a 150 mg/mL stock solution. Separately, 10 mg of DOPE was dissolved in 1.0 mL of pure ethanol to produce a 10 mg/mL stock solution (alternatively, 100 mg in 10 mL ethanol). Similarly, 10 mg of cholesterol was dissolved in 1.0 mL of pure ethanol (or 50 mg in 5 mL ethanol), and 10 mg of DMG-PEG was dissolved in 1.0 mL of ethanol (or 50 mg in 5 mL ethanol), resulting in 10 mg/mL stock solutions for each. A 20 mM working lipid mixture was prepared by combining 6.7 µL of the 4A3-SC8 solution (23.8%, 4.76 mM), 50.7 µL of the DOPE/DSPC solution (23.8%, 4.76 mM), 52.7 µL of the cholesterol solution (47.6%, 9.52 mM), and 34.2 µL of the DMG-PEG solution (4.8%, 0.96 mM).

The working lipid mixture was used to encapsulate mRNAs in the lipid nanoparticle (LNP) formulation. Initially, the lipid mixture was equilibrated at room temperature for at least 5 minutes and then vortexed at speed 10 for 5 seconds. A lipid mastermix was subsequently prepared by mixing 12 μL of the lipid mixture with 18 μL of 200-proof ethanol, yielding 30 μL per reaction. This mastermix was distributed into individual tubes. Each RNA mixture was prepared by combining 40 μL of RNA solution (250 ng/ μL ; total 10 μg RNA input) with 32 μL of nuclease-free water and 18 μL of 50 mM citrate buffer, yielding a total volume of 90 μL per reaction. To assemble the LNPs, 30 μL of the lipid mastermix was placed on a Vortex-Genie 2 vortex mixer set at speed level 1. While vortexing, 90 μL of the RNA mixture was rapidly pipetted into the lipid mastermix in a single action, and vortexing was continued for 30 seconds.

The resulting dispersion was incubated at room temperature for 5 minutes, and dialysis was initiated within 15 minutes of mixing. Dialysis was performed using Pur-A-Lyzer Midi 3500 dialysis tubes. Each tube was preconditioned by adding 900 μL of water, incubating for 5 minutes, and then removing the water. Approximately 120 μL of each LNP sample was transferred into the dialysis tubes, which were placed into a styrofoam holder and submerged in 1X PBS within a beaker. Dialysis was conducted either for 1 hour at room temperature or overnight at 4°C. After dialysis, each sample was transferred into an RNase-free 1.5 mL microcentrifuge tube, and the final volume was measured. Samples were adjusted to a total volume of 500 μL by adding the appropriate volume of 1X PBS. All samples were stored at 4°C.

The resulting mRNA-LNP particles exhibited nearly complete transfection efficiency of human MIA PaCa-2 cells, and allowed titration of expression over four orders of magnitude (**fig. S6a**). This approach was also compatible with multi-component delivery of separately encapsulated mRNAs (**fig. S6b**).

mRNA-LNP transfection of human cell lines

LNPs were reverse transfected by first adding LNPs to culture plates, followed by the addition of cells on top. To maximize transfection efficiency *in vitro*, mRNA-containing LNPs were pre-complexed with ApoE, a naturally excreted liver protein that binds lipids *in vivo* and recruits lipid particles to cells expressing the low-density lipoprotein (LDL) receptor.

Cell viability assay with CellTiter-Glo

Cell viability was assessed using the CellTiter-Glo (CTG) Luminescent Cell Viability Assay (Promega). Cells were seeded into 96-well plates at 100 μ L medium per well and incubated with treatments as described for each experiment. Nunc Edge 2.0 plates were used to minimize edge effects. On the day of the viability assay, plates were removed from the incubator and equilibrated at room temperature for 30 minutes prior to CTG reagent addition. Subsequently, 100 μ L of CTG reagent was directly added into each well. Plates were then placed on an orbital shaker in the Promega GloMax instrument and shaken for 2 minutes to facilitate cell lysis and thorough mixing of the reagent. Following shaking, plates were incubated at room temperature for an additional 10 minutes to stabilize the luminescent signal. During this incubation, 180 μ L of the mixture from each well was transferred into a white luminescence-compatible plate. Luminescence was measured using the GloMax according to the manufacturer's protocol. Cell viability was calculated by normalizing raw luminescence measurements of treated to untreated samples. Where applicable, dose-response curves were modeled with a four-parameter log-logistic model. The same model was used to calculate EC₃₀, EC₅₀, EC₇₀, and EC₉₀ concentrations. We compared the goodness of fit between different models with the sum-of-squares F-test. More specifically, we compared models fitting separate curves or a reduced four-parameter log-logistic model assuming a single curve.

Cell viability assay with flow cytometry

Cell Titer Glo (CTG) provides accurate measurements only within a specific range of cell densities. Thus, for experiments testing varying initial cell densities and their effects on

drug versus circuit efficacy, we used flow cytometry to quantify cell viability. Annexin V staining was used to gate and exclude dead cells from analysis.

Analysis of Ras circuit response to EGF

HEK293 cells (100k cells per well) were seeded in a 24-well plate and treated with epidermal growth factor (EGF) at concentrations of 0, 0.1, 1, 10, and 100 ng/mL for 1 hour. Following treatment, cells were processed for phospho-ERK staining and analyzed by flow cytometry. Specifically, cells were fixed by adding an equal volume (600 μ L) of 2X eBioscience™ IC Fixation Buffer directly to each well, followed by gentle vortexing to mix thoroughly. Samples were incubated for 20 minutes at room temperature in the dark. After fixation, cells were scraped thoroughly from each well using a pipette tip, collected, and centrifuged at $600 \times g$ for 5 minutes at room temperature, followed by removal of the supernatant. Cell pellets were then resuspended in the residual volume and permeabilized by adding 200 μ L ice-cold 90–100% methanol (HPLC grade), followed by vortexing and incubation for at least 30 minutes on ice. Subsequently, cells were washed by adding 600 μ L eBioscience™ Flow Cytometry Staining Buffer, centrifuged at $600 \times g$ for 5 minutes, and the supernatant discarded. The wash step was repeated, leaving approximately 100 μ L of residual staining buffer. Cells were stained with 5 μ L (0.125 μ g) directly conjugated anti-phospho-ERK1/2 antibody (Catalog #12-9109-42) for 30 minutes at room temperature in the dark. After staining, cells underwent two additional washes with 600 μ L Flow Cytometry Staining Buffer, each followed by centrifugation at 400 – $600 \times g$ for 4–5 minutes, with final resuspension in 100 μ L of staining buffer for analysis. Finally, cells were analyzed by flow cytometry using the entire remaining volume (100 μ L). The fraction of pERK positive cells was calculated as the fraction of cells with ECD-A signal $> 10^3$ a.u. Cell viability was measured as described above.

mRNA sequencing and analysis

mRNA was extracted from 96-well plates using Direct-zol-96 RNA Kits (Zymoresearch Cat# R2055). 50 ng of extracted mRNA from each sample was used as input for

downstream NGS library preparation. mRNA-seq libraries were prepared in 96-well format using a modified 3'Pool-seq protocol. In brief, reverse transcription reactions were prepared by mixing input RNA with 1 μ l Indexed RT Primer (10 μ M), 1 μ l 10 mM dNTP Mix (New England Biolabs Cat# N0447S), 1 μ l diluted ERCC Spike-In Mix 1 (0.004 μ L stock ERCC per μ g RNA, ThermoFisher Cat# 4456740), 3.6 μ l of 5X RT buffer (ThermoFisher Cat# EP0752), 0.5 μ l of RNase inhibitor (ThermoFisher Cat# EO0381), 1 μ l Maxima RT H Minus (ThermoFisher Cat# EP0752), and 2.5 μ l 10 μ M Template Switching Oligo in an 18 μ l reaction. Reverse transcription was carried out in a thermocycler using the program described in the 3'Pool-seq protocol. Samples from each row of the 96-well plate were pooled (column pooling) by mixing an equal volume of each reverse transcription reaction into a new well, for a total volume of 20 μ l. Residual primers were degraded by adding 1 μ l Exonuclease I (New England Biolabs) and incubating at 37 $^{\circ}$ C for 45 min, followed by denaturation at 92 $^{\circ}$ C for 15 min. Subsequent cDNA amplification, tagmentation, and row pooling were performed following the 3'Pool-seq protocol. Finally, 20 μ l of pooled NGS library was subjected to gel-based size selection using E-Gel EX Agarose Gel (ThermoFisher Cat# G401001) to enrich for fragments in the 200–1000 bp range, and eluted in 15 μ l. Eluted pooled NGS libraries were examined using an Agilent TapeStation 4200 (Agilent Technologies) to determine average fragment sizes. Library concentration was quantified using a Qubit 3.0 Fluorometer (Life Technologies). NGS libraries were diluted to 2 nM, denatured in 0.2 N NaOH, and loaded onto the Element AVITI sequencer following the Element Biosciences Cloudbreak Sequencing user guide. Read de-multiplexing was performed with Bases2Fastq, a standard software package used with the Element Biosciences system. De-multiplexed reads were aligned to the reference genome GRCh38.103 using STAR (2.7.8a) with the ENCODE standard options, except “–outFilterScoreMinOverLread 0.3 –outFilterMatchNminOverLread 0.3 –outFilterMultimapNmax 20”. Uniquely mapped reads that overlapped with genes were counted using HTSeq-count (0.13.5) with default settings, except “–m intersection-strict”. To normalize for differences in sequencing depth across samples, we rescaled gene counts to counts per million (CPM). Fold-changes and adjusted p-values were calculated using the R package DESeq2.

Drug treatment *in vitro*

Cells were treated with Sotorasib/AMG-510 (10 mM, MedChemExpress, Cat. No.: HY-114277), RMC-7977 (10 mM, MedChemExpress, Cat. No.: HY-156498), or Paclitaxel (10 mM, MedChemExpress, Cat. No.: HY-B0015) at the indicated concentrations per experiment.

Time-lapse microscopy

HEK293 and MIA PaCa-2 cell lines were engineered to stably express mRuby3 and GFP, respectively. A co-culture containing 50,000 total cells at a 3:1 ratio of HEK293 to MIA PaCa-2 was seeded into black-walled, glass-bottom 24-well plates (Ibidi) and incubated overnight. The following day, drug or circuit treatments were applied, and plates were imaged using an Olympus automated microscope controlled by MetaMorph software. Time-lapse image acquisition was performed every 2 hours. Images were processed using a custom pipeline in Python. Raw image tiles were first stitched with 10% overlap to reconstruct full fields of view. Stitched images underwent three main processing steps. First, Gaussian filtering (7×7 kernel) was applied to denoise background speckles. Second, image contrast was normalized using percentile-based intensity scaling, with intensities rescaled between the 1st and 99.9th percentiles to account for field-to-field variation. Finally, a dual-threshold segmentation strategy was used for cell detection and quantification. Pixels exceeding the high threshold (20th percentile of the normalized intensity range) were classified as healthy cells and assigned a fixed intensity value of 180. Pixels between the high (20th percentile) and low (15th percentile) thresholds were preserved with their scaled intensities to capture cells with reduced fluorescence signal, indicative of potential cell stress or death. This method enabled consistent detection of both bright and dim cells while preserving biologically relevant signal variation.

Sequential resistance selection with drugs and circuit

MIA PaCa-2 cells were plated in a 10 cm tissue culture plate (350k cells/plate). Cells were treated with the IC₇₀ concentrations that we previously determined, specifically 1 μ M of Sotorasib and 60 pg/ μ L each of Ras sensor and Casp-3 mRNA-LNPs. After treatment for five days, cells were washed with PBS, trypsinized, replated at the same density (350k cells), and re-treated identically as described above. In total, cells underwent three rounds of selection treatment. At two time points—before the first treatment (“no selection”) and after the final treatment—we collected cells and exposed them to concentration ranges of either Sotorasib or circuit. For Sotorasib, concentrations tested were 0.0001, 0.001, 0.01, 0.1, 1, and 10 μ M. For circuit testing, cells were treated with mRNA-LNPs of Ras sensor/Casp-3 at concentrations of 10, 20, 40, 80, 160, and 320 pg/uL. Cell viability was read out by CellTiter Glo three days post transfection.

Analysis of Sotorasib and circuit response to increased Ras expression

10k MIA PaCa-2 cells were transfected with either 200 pg/ μ L KRAS^{G12C} mRNA-LNP or 200 pg/ μ L NeoR mRNA-LNP as negative control. These mRNA-LNPs were co-delivered with 0.0001, 0.001, 0.01, 0.1, 1, and 10 μ M of Sotorasib or 10, 20, 40, 80, 160, and 320 pg/uL of circuit mRNA-LNP (sensor v2-s + Casp-3). Cell viability was read out by CellTiter Glo three days post transfection.

Animal studies

All animal handling, care, and treatment procedures were carried out in accordance with the applicable regulations and guidelines established by the relevant Institutional Animal Care and Use Committee (IACUC). Animals were housed in polycarbonate cages within an environmentally controlled, well-ventilated room maintained at a constant temperature of 20-26°C and a relative humidity of 40-80%. Fluorescent lighting was provided on a 12-hour light/dark cycle.

In vivo hydrodynamic tail vein injection liver tumor models

FVB/NJ mice (Jackson Laboratory, 001800) were used for HDT tumor models due to their enhanced susceptibility to tumor development. The FVB mice used in this study were ordered directly from Jackson Laboratory (001800). Hydrodynamic transfection was used to introduce transposable vectors expressing mutant NRAS-G12V, TP53 shRNA, and sleeping beauty transposase (SB100) into FVB mice. Mice were injected at 6-8 weeks of age, when their body weights were ~18-25 g. HDT plasmids were suspended at the noted concentrations in 2 mL of saline and administered via tail-vein injection over 7 seconds. A 10:1 mass ratio of combined HDT plasmids to SB100 transposase plasmid was used. In the genetic tumor rescue experiments PT2-NRAS-G12V was used, and 10 ug/mouse of each plasmid was added to the HDT volume. LNP studies substituted PT3-NRAS-G12V, and 1 ug of this plasmid/mouse was used due to increased tumor induction efficiency. In the *in vivo* mRNA-LNP experiments, LNPs were dosed at 1.5 mg total RNA per kg body weight dissolved in 0.2 mL PBS via the lateral tail vein at the noted time points.

Liver and body weight measurements

Animals were euthanized by cervical dislocation under isoflurane anesthesia. Livers were removed, weighed, and imaged at the time of sacrifice. Liver/body weight ratios were calculated as follows: $(\text{whole liver weight})/(\text{intact body weight}) \times 100$. Extracted livers were imaged (anterior and posterior view) and corresponding images were used to assess the surface tumor burden of each animal. More specifically, tumor nodules were annotated manually in a blinded fashion. Surface tumor burden was calculated as accumulated surface tumor area over anterior and posterior liver views.

Liver surface tumor area annotation and masking

Liver images were manually annotated for nodules by an independent annotator with no involvement in the study. The annotation process was blinded: image files were assigned numeric identifiers, and the annotator was not provided with any information regarding

experimental conditions. Tumors were manually segmented using NimbusImage on a total of 284 images of mouse livers. Each image received three separate masks: (1) “white nodes” for tumors that appeared lighter than surrounding tissue, (2) “black nodes” for tumors that appeared darker, and (3) a whole-liver mask outlining the total liver area. Only abnormalities larger than approximately 1 mm were included. Both raised masses and regions of distinct discoloration were classified as nodules. Non-tumor features such as fat deposits, blood vessels, bubbles, and specular reflections were excluded from annotation.

Kaplan-Meier curve

Tumors were induced in FVB mice as described above, with or without the noted circuits plasmids. Tumor development was allowed to proceed until reaching any of the three following clinical endpoints: a body condition score of 1, difficulty breathing, or decreased motility resulting in inability to obtain food or water, at which point mice were immediately euthanized at the recommendation of veterinary staff. Log-rank test was used to determine if differences in survival were significant.

LNP formulation and physical characterization for mouse studies

The following lipids were dissolved in 100% ethanol at a 15:30:15:3:7 molar ratio: 4A3-SC8 lipid (synthesized in-house), cholesterol (Sigma Aldrich Cat. No. C3045), DOPE (Avanti Polar Lipids Cat. No. 850725), DMG-PEG-2000 (Avanti Polar Lipids Cat. No. 880151), and DOTAP (Avanti, 890890P) with a total lipid:RNA mass ratio of 40:1. RNA was dissolved in 10 mM citrate buffer (pH 4.5) at a 3:1 v/v aqueous:organic phase ratio. LNPs were formed by microfluidic mixing of the lipid and RNA solutions using a Precision Nanosystems NanoAssemblr Benchtop Instrument, in accordance with the manufacturer’s protocol. LNPs were dialyzed in PBS overnight at 4°C and stored at 4°C for up to 72 hours. Particle size and dispersity were measured by dynamic light scattering (DLS) using a Malvern Zetasizer DLS instrument.

Software

The following software was used in this study:

Data collection: AlphaFold 3 (AlphaFold Server), Colabfold (v1.5.2), RFDiffusion (v1.1.0), ProteinMPNN-FastRelax (dl_binder_design v1.0.0), MetaMorph (version 6.2.6)

Data analysis: PyMol (version 2.5.4), ChimeraX (version 1.7.1), FlowJo (version 10.10.0), SnapGene (version 8.0.2), Geneious (version 2023.0.4), Bases2Fastq (Element Biosciences, <https://github.com/ElemBio/bases2fastq-dx>), NimbusImage, conda (v4.14.0), python (v3.12.3), bioconductor-biomart (v2.58.0), bioconductor-biostings (v2.70.1), bioconductor-deseq2 (v1.42.0), cairo (v1.18.0), imagemagick (v7.1.1_33), ipykernel (v6.29.5), ipython (v8.26.0), jupyter_server (v2.14.2), jupyterlab (v4.2.1), r-base (v4.3.3), r-cowplot (v1.1.3), r-dplyr (v1.1.4), r-essentials (v4.3), r-ggplot2 (v3.5.1), r-ggpubr (v0.6.0), r-ggrepel (v0.9.5), r-jsonlite (v1.8.8), r-magick (v2.8.3), r-colorbrewer (v1.1_3), r-tidyverse (v2.0.0), pandas (v2.2.3), matplotlib (v3.10.1), numpy (v2.2.4), scipy (v1.15.2), scikit-learn (v1.6.1), opencv-python (v4.7.0.72), scikit-image (v0.20.0), pillow (v9.5.0)

CHAPTER 4 BIBLIOGRAPHY

1. Prior IA, Hood FE, Hartley JL. The frequency of Ras mutations in cancer. *Cancer Res.* 2020;80: 2969–2974. doi:10.1158/0008-5472.CAN-19-3682
2. Prior IA, Lewis PD, Mattos C. A comprehensive survey of Ras mutations in cancer. *Cancer Res.* 2012;72: 2457–2467. doi:10.1158/0008-5472.CAN-11-2612
3. Miller MS, Miller LD. RAS Mutations and Oncogenesis: Not all RAS Mutations are Created Equally. *Front Genet.* 2011;2: 100. doi:10.3389/fgene.2011.00100
4. Andreyev HJ, Norman AR, Cunningham D, Oates J, Dix BR, Iacopetta BJ, et al. Kirsten ras mutations in patients with colorectal cancer: the “RASCAL II” study. *Br J Cancer.* 2001;85: 692–696. doi:10.1054/bjoc.2001.1964
5. Hu H-F, Ye Z, Qin Y, Xu X-W, Yu X-J, Zhuo Q-F, et al. Mutations in key driver genes of pancreatic cancer: molecularly targeted therapies and other clinical implications. *Acta Pharmacol Sin.* 2021;42: 1725–1741. doi:10.1038/s41401-020-00584-2
6. Wasko UN, Jiang J, Dalton TC, Curiel-Garcia A, Edwards AC, Wang Y, et al. Tumour-selective activity of RAS-GTP inhibition in pancreatic cancer. *Nature.* 2024;629: 927–936. doi:10.1038/s41586-024-07379-z
7. Biller LH, Schrag D. Diagnosis and treatment of metastatic colorectal cancer: A review: A review. *JAMA.* 2021;325: 669–685. doi:10.1001/jama.2021.0106
8. Martin J, Petrillo A, Smyth EC, Shaida N, Khwaja S, Cheow HK, et al. Colorectal liver metastases: Current management and future perspectives. *World J Clin Oncol.* 2020;11: 761–808. doi:10.5306/wjco.v11.i10.761
9. Zhou H, Liu Z, Wang Y, Wen X, Amador EH, Yuan L, et al. Colorectal liver metastasis: molecular mechanism and interventional therapy. *Signal Transduct Target Ther.* 2022;7: 70. doi:10.1038/s41392-022-00922-2
10. Li BT, Velcheti V, Price TJ, Hong DS, Fakih M, Kim D-W, et al. Largest evaluation of acquired resistance to sotorasib in KRAS p.G12C-mutated non-small cell lung cancer (NSCLC) and colorectal cancer (CRC): Plasma biomarker analysis of CodeBreaK100. *Journal of Clinical Oncology.* 2022 [cited 16 Apr 2025]. doi:10.1200/JCO.2022.40.16_suppl.102

11. Liu J, Kang R, Tang D. The KRAS-G12C inhibitor: activity and resistance. *Cancer Gene Ther.* 2022;29: 875–878. doi:10.1038/s41417-021-00383-9
12. Pao W, Chmielecki J. Rational, biologically based treatment of EGFR-mutant non-small-cell lung cancer. *Nat Rev Cancer.* 2010;10: 760–774. doi:10.1038/nrc2947
13. Perurena N, Cichowski K. Finding the sweet spot: Targeting RAS in tumors while sparing normal tissue. *Cancer Cell.* 2024;42: 943–945. doi:10.1016/j.ccell.2024.05.020
14. Punekar SR, Velcheti V, Neel BG, Wong K-K. The current state of the art and future trends in RAS-targeted cancer therapies. *Nature Reviews Clinical Oncology.* 2022;19: 637–655. doi:10.1038/s41571-022-00671-9
15. Liu J, Kang R, Tang D. Correction: The KRAS-G12C inhibitor: activity and resistance. *Cancer Gene Ther.* 2023;30: 1715. doi:10.1038/s41417-023-00692-1
16. Sabnis AJ, Bivona TG. Principles of resistance to targeted cancer therapy: lessons from basic and translational cancer biology. *Trends in molecular medicine.* 2019;25: 185. doi:10.1016/j.molmed.2018.12.009
17. Awad MM, Liu S, Rybkin II, Arbour KC, Dilly J, Zhu VW, et al. Acquired resistance to KRASG12C inhibition in cancer. *N Engl J Med.* 2021;384: 2382–2393. doi:10.1056/NEJMoa2105281
18. de Langen AJ, Johnson ML, Mazieres J, Dingemans A-MC, Mountzios G, Pless M, et al. Sotorasib versus docetaxel for previously treated non-small-cell lung cancer with KRASG12C mutation: a randomised, open-label, phase 3 trial. *Lancet.* 2023;401: 733–746. doi:10.1016/S0140-6736(23)00221-0
19. Vaux DL. In defense of the somatic mutation theory of cancer. *Bioessays.* 2011;33: 341–343. doi:10.1002/bies.201100022
20. Cheng Q, Wei T, Farbiak L, Johnson LT, Dilliard SA, Siegwart DJ. Selective organ targeting (SORT) nanoparticles for tissue-specific mRNA delivery and CRISPR-Cas gene editing. *Nat Nanotechnol.* 2020;15: 313–320. doi:10.1038/s41565-020-0669-6
21. Wang X, Liu S, Sun Y, Yu X, Lee SM, Cheng Q, et al. Preparation of selective organ-targeting (SORT) lipid nanoparticles (LNPs) using multiple technical methods for tissue-specific mRNA delivery. *Nat Protoc.* 2023;18: 265–291. doi:10.1038/s41596-022-00755-

22. [Wang Q, Wang Y, Ding J, Wang C, Zhou X, Gao W, et al. A bioorthogonal system reveals antitumour immune function of pyroptosis. Nature. 2020;579: 421–426. doi:10.1038/s41586-020-2079-1](#)
23. [Zhang Z, Zhang Y, Xia S, Kong Q, Li S, Liu X, et al. Gasdermin E suppresses tumour growth by activating anti-tumour immunity. Nature. 2020;579: 415–420. doi:10.1038/s41586-020-2071-9](#)
24. [Kolch W, Berta D, Rosta E. Dynamic regulation of RAS and RAS signaling. Biochem J. 2023;480: 1–23. doi:10.1042/BCJ20220234](#)
25. [Kiyatkin A, Aksamitiene E, Markevich NI, Borisov NM, Hoek JB, Kholodenko BN. Scaffolding protein Grb2-associated binder 1 sustains epidermal growth factor-induced mitogenic and survival signaling by multiple positive feedback loops. J Biol Chem. 2006;281: 19925–19938. doi:10.1074/jbc.M600482200](#)
26. [Coyle SM, Lim WA. Mapping the functional versatility and fragility of Ras GTPase signaling circuits through in vitro network reconstitution. Elife. 2016;5. doi:10.7554/eLife.12435](#)
27. [Boykevisch S, Zhao C, Sondermann H, Philippidou P, Halegoua S, Kuriyan J, et al. Regulation of ras signaling dynamics by Sos-mediated positive feedback. Curr Biol. 2006;16: 2173–2179. doi:10.1016/j.cub.2006.09.033](#)
28. [Holderfield M, Lee BJ, Jiang J, Tomlinson A, Seamon KJ, Mira A, et al. Concurrent inhibition of oncogenic and wild-type RAS-GTP for cancer therapy. Nature. 2024;629: 919–926. doi:10.1038/s41586-024-07205-6](#)
29. [Hou X, Zaks T, Langer R, Dong Y. Lipid nanoparticles for mRNA delivery. Nat Rev Mater. 2021;6: 1078–1094. doi:10.1038/s41578-021-00358-0](#)
30. [Masarwy R, Stotsky-Oterin L, Elisha A, Hazan-Halevy I, Peer D. Delivery of nucleic acid based genome editing platforms via lipid nanoparticles: Clinical applications. Adv Drug Deliv Rev. 2024;211: 115359. doi:10.1016/j.addr.2024.115359](#)
31. [Tada M, Omata M, Ohto M. High incidence of ras gene mutation in intrahepatic cholangiocarcinoma. Cancer. 1992;69. doi:10.1002/cncr.2820690509](#)

32. Chen X, Calvisi DF. Hydrodynamic transfection for generation of novel mouse models for liver cancer research. Am J Pathol. 2014;184: 912–923. doi:10.1016/j.ajpath.2013.12.002
33. Molina-Sánchez P, Ruiz de Galarreta M, Yao MA, Lindblad KE, Bresnahan E, Bitterman E, et al. Cooperation between distinct cancer driver genes underlies intertumor heterogeneity in hepatocellular carcinoma. Gastroenterology. 2020;159: 2203–2220.e14. doi:10.1053/j.gastro.2020.08.015
34. Hsieh M-H, Wei Y, Li L, Nguyen LH, Lin Y-H, Yong JM, et al. Liver cancer initiation requires translational activation by an oncofetal regulon involving LIN28 proteins. J Clin Invest. 2024;134. doi:10.1172/JCI165734
35. Ostrem JM, Peters U, Sos ML, Wells JA, Shokat KM. K-Ras(G12C) inhibitors allosterically control GTP affinity and effector interactions. Nature. 2013;503: 548–551. doi:10.1038/nature12796
36. Wasko UN, Jiang J, Dalton TC, Curiel-Garcia A, Edwards AC, Wang Y, et al. Tumour-selective activity of RAS-GTP inhibition in pancreatic cancer. Nature. 2024;629: 927–936. doi:10.1038/s41586-024-07379-z
37. To T-L, Piggott BJ, Makhijani K, Yu D, Jan YN, Shu X. Rationally designed fluorogenic protease reporter visualizes spatiotemporal dynamics of apoptosis in vivo. Proc Natl Acad Sci U S A. 2015;112: 3338–3343. doi:10.1073/pnas.1502857112

Chapter 5

CONCLUSIONS

5.1 Discussions

Our results demonstrate end-to-end development of therapeutic protein circuits that kill Ras-mutant cancer cells and treat tumors *in vivo*. In fact, despite the induced tumors analyzed here being aggressive and extremely difficult to treat, circuits still showed significant therapeutic benefit. The circuits designed here achieved comparable specificity and superior potency compared to state-of-the-art drugs, while being considerably easier and faster to design.

What accounts for these advantages?

1) First, unlike drugs, the efficacy of the sense-and-kill circuit mechanism is largely a function of only parameters of circuit delivery and of the sensing target, such as Ras expression level or specific conformational states. Circuit efficacy hence does not depend on the often unpredictable state of the cancer cell. In contrast, the efficacy and predictability of small molecule targeted therapies almost always hinge on the underlying cell state, which carries dramatic and critical therapeutic implications. This is perhaps best exemplified by Ras-targeted therapies such as Sotorasib or RMC-7977, where there is an absolute requirement that on-target cells must not only harbor Ras mutations, but also exhibit oncogene addiction to Ras signaling.

Ras oncogene addiction, as commonly defined, refers to a cellular state in which Ras signaling serves as a central and irreplaceable driver of cell survival and proliferation. In such cases, inhibition of Ras sets off a predictable cascade of molecular events- disruption of protein-protein interactions, altered post-translational modifications, and activation or de-repression of specific effector proteins- that ultimately lead to programmed cell death.

However, this dependence on oncogene addiction is problematic for several reasons. First, cancer cells and their signaling pathways are profoundly heterogeneous, both between patients and even within individual tumors. This heterogeneity encompasses genetic, epigenetic, and metabolic differences, all of which can influence pathway wiring and drug response. Second, these networks are resilient and adaptive. Cancer cells can rewire their signaling circuitry in response to selective pressure, finding alternative routes to sustain survival or growth. Third, the relevant signaling networks are often only partially mapped and poorly understood, making it difficult to predict which cells will truly be addicted to a given pathway, even when they carry the nominal target mutation.

A further complication is that it is fundamentally difficult to model the actual states of oncogenic addiction seen in human tumors (if we assume that such states truly exist at all). Preclinical systems like *in vitro* cell lines or xenografts in immunocompromised mice are, at best, rough approximations of real human tumors. It remains unclear whether these systems ever fully capture the complexity or authenticity of naturally evolved, Ras-addicted human cancers. **In some cancer types, even the idea of oncogene addiction itself may be more an artifact of simplified models than a reliable property of actual tumors.** If true oncogenic addiction is rare, unstable, or context-dependent in patients, then much of the logic behind current targeted therapy development becomes questionable. This uncertainty calls into question how much we can rely on results from reductionist or artificial models, and whether the assumptions guiding these therapies match the biological reality found in human disease.

Perhaps, then, the disappointing translation rate of targeted therapies- from promising *in vitro* results, to mixed outcomes in animal models, to often limited efficacy in human patients- is not primarily due to a lack of good targets or faulty drugs. **Instead, it may reflect a deeper problem: that an entire category of cancer therapeutics has been built upon the shaky foundation of assumptions about cell state, addiction, and model fidelity.** The sense-and-kill circuit approach, by decoupling therapeutic efficacy from these uncertain variables, represents a conceptual shift and a potential solution to this longstanding bottleneck in cancer drug development.

2) Second, the ability to use proteins as sensors is advantageous over small molecules for many reasons. For one, protein-based therapeutics allow for large binding interfaces that can detect molecular features that are otherwise challenging to drug. Unlike small molecules, proteins can engage extended or discontinuous surfaces on their targets, such as specific domains or allosteric sites, rather than being limited to small, solvent-exposed deep pockets. This enables proteins to bind with high affinity and selectivity to targets that have historically been considered “undruggable,” such as Ras, or to differentiate between closely related protein isoforms. Many oncogenic mutations, including most Ras mutations, do not create new pockets suitable for small molecule binding, but do alter the three-dimensional surface of the protein in ways that are accessible to engineered binders. Furthermore, protein-based sensors can be evolved or designed to recognize not just sequence changes, but also subtle conformational or structural differences that arise from oncogenic activation states.

Perhaps equally as important, while the diversity of small molecule libraries is constrained by the limitations of chemical synthesis, protein therapies benefit from both straightforward DNA encoding and synthesis. This experimental accessibility, together with computational protein design, enabled efficient exploration of the immense protein potential space and engineering of highly specific Ras sensor modules.

3) Third, scientifically, circuit therapeutics have many advantages. The circuits are genetically compact (*e.g.*, ~2kb for the pyroptosis circuit v2-s) and easily deliverable by LNP. From a safety point of view, the use of mRNA allows circuits to function transiently without permanent genome modification. Circuits also offer benefits compared to pyroptosis-inducing gasdermin agonists. Unlike these drugs, which broadly activate pyroptosis and could induce hyper-inflammation, circuits restrict its activation to cancer cells. Additionally, since circuits ectopically deliver gasdermins, they could overcome the observed problem of gasdermin silencing in tumor cells, which would render drugs ineffective [1–3].

4) Fourth, therapeutic circuits could potentially shift human medicine towards a more “engineered discipline”.

There is a frequent debate between those who argue we need to treat biology more like physics and engineering, and those who claim biology is inherently too complex for these approaches. Advocates for the engineering viewpoint say biological systems, despite their complexity, fundamentally obey physical and chemical laws. Synthetic biology, for example, has successfully engineered complex circuits and regulatory modules, such as genetic toggle switches, oscillators, and logic gates, showing biology can be predictably designed and controlled when adequately understood. Similarly, efforts like BioBricks and the International Genetically Engineered Machine (iGEM) competition have promoted modularity and standardization, enabling simpler and more predictable ways to build biological systems from interchangeable parts.

In contrast, skeptics highlight the immense complexity, context dependence, and emergent behaviors of biological systems, arguing that such unpredictability limits engineering approaches. Biological networks often display emergent properties and adaptability that defy rational predictions. Even rationally designed synthetic circuits frequently exhibit unexpected behaviors due to unknown interactions, epigenetic variability, or cellular context dependencies. This inherent complexity complicates the straightforward application of engineering principles traditionally successful in physics or electronics.

Yet, the engineering approach has gained substantial ground, largely due to advances in experimental tools. As Sydney Brenner famously said, “*Progress in science depends on new techniques, new discoveries, and new ideas, probably in that order.*” This underscores how tool development shapes scientific advances. For instance, advances in bacterial transcriptional control, such as well-characterized repressors and inducible promoters, were critical for creating synthetic biology’s early circuits, including Michael’s “repressilator” oscillator composed of three transcriptional repressors arranged in a negative-feedback loop.

Likewise, there is a parallel debate specifically within human medicine and therapeutic development. Proponents of treating medicine as an engineering discipline argue that therapies can and should be systematically designed, optimized, and improved iteratively, much like engineering machines or software. Rationally designed targeted therapies, like kinase inhibitors, show that well-characterized molecular pathways can sometimes be predictably targeted.

Critics, however, argue human disease complexity and individual variability fundamentally limit applying engineering principles to medicine. Diseases often arise from complex interactions among genetics, environment, immunology, and metabolism. Even rational therapies, such as targeted cancer drugs, often fail when transitioning from simplified preclinical models to real patients, reflecting fundamental limitations in model fidelity and biological understanding.

What happens if we try to draw from the same debate in biology and basic science? The main challenge with the “medicine as engineering” paradigm might not be the logic itself, but rather that human medicine currently lacks the sophisticated engineering toolbox that basic biology has developed for itself.

What even constitutes the “engineering toolbox” for oncology today?

Currently, small molecules represent by far the most common and heavily invested modality in oncology therapeutics. However, several factors limit their engineering potential. First, chemical diversity space is difficult to explore comprehensively, requiring complex synthetic methods and specialized expertise. Ideally, the foundational molecule for a therapy exists within a space that is cheap and easy to explore.

Second, small molecules face intrinsic constraints: a single molecule must simultaneously fulfill multiple challenging requirements. It must specifically bind protein targets, induce functional perturbations, efficiently cross cell membranes, achieve good pharmacokinetics and bioavailability, and maintain stability in the body. *Imagine telling an engineer to*

design an air conditioning system where the thermostat, the compressor, the refrigerant, and the fan all have to be made from the exact same component. Not housed in the same unit- literally the same material, performing all functions at once.

Third, good engineering ideally involves tight feedback cycles of iterative improvement. However, as discussed repeatedly throughout this thesis, small molecules face fundamental constraints because their efficacy strongly depends on the complex, variable, and often poorly modeled tumor cell states. Thus, medicinal chemists can screen compounds for binding specificity or efficacy in cell lines or mouse models, but it remains uncertain whether these feedback loops genuinely guide molecules toward reliable human efficacy.

Multifunctional molecules, such as PROTACs or tri-complex inhibitors like RMC-7977, represent promising advancements, potentially moving medicinal chemistry closer to engineering. These molecules partially overcome the constraint of simultaneously optimizing specificity and efficacy by separating targeting from therapeutic “rewiring.” PROTACs expand both sensing (by allowing targeting domains separate from effector domains) and therapeutic outputs (like inducing targeted protein degradation). Yet, PROTACs still rely on the tumor cell’s internal signaling machinery for efficacy, leaving them vulnerable to the same unpredictability as traditional small molecules.

CAR-T cell therapy is perhaps the clearest example of synthetic biology and cell engineering successfully translated into human medicine. CAR-T cells overcome fundamental limitations faced by earlier therapeutic approaches: clearly separating specificity (scFVs) from therapeutic outcomes (intracellular signaling domains), enabling more realistic modeling through human primary immune cells, and supporting iterative engineering through modular protein-domain structures. Although CAR-T therapies have their own challenges such as exhaustion, poor tumor infiltration, high costs, and cytokine toxicity, they undeniably sparked a paradigm shift in how medicine views therapeutic engineering.

The CAR-T example highlights how a single transformative technology reshaped the medicine-versus-engineering debate, demonstrating synthetic biology principles in clinical contexts. **The therapeutic circuits described in this thesis could similarly serve as another foundational technology, potentially bridging synthetic biology, oncology, and clinical medicine.** While significant challenges undoubtedly remain, including delivery and immunogenicity, these circuits provide a starting point for reconsidering how we approach designing cancer therapies. Ultimately, the hope is that circuits might offer more predictable therapeutic effects, less reliant on uncertain models or poorly defined cell states. If successful, they could complement existing modalities and perhaps move oncology one step closer toward genuinely engineered therapeutic solutions. However, as with any emerging technology, it will be critical to remain thoughtful and realistic about what is truly achievable, what limitations exist, and how these circuits can integrate into a broader clinical ecosystem.

The present circuits have several limitations. First, more *in vivo* studies will be required to comprehensively evaluate circuit function in cell- and patient-derived xenografts as well as in metastatic settings, in order to better understand their therapeutic potential across diverse Ras-driven cancers. In particular, it will be important to determine how apoptosis and pyroptosis should be balanced to maximize tumor clearance while minimizing potential toxicity from hyper-inflammation. Second, while the sensors respond to many Ras mutations, they do not respond equally to all. Future work could produce improved sensors with broader specificity or introduce mixtures of sensors for different Ras variants. Third, while intravenous LNP delivery can target some clinically relevant tissues, many other disease sites remain inaccessible [4–6]. This issue could be mitigated by intratumoral delivery (in the cancer context), or through emerging technologies like selective organ targeting (SORT) nanoparticles [4]. We note that the circuit paradigm effectively shifts the burden of specificity from the delivery method to the circuit itself, which could make circuits compatible with higher penetrance but less tissue-specific delivery methods. Fourth, a potential concern with any circuit that uses non-human proteins is immunogenicity. Here, we used a viral protease as a major component. In the future,

however, similar circuits could be implemented with humanized protease variants or by altering the substrate specificity of human proteases [7].

5.2 Future Directions

Perhaps the most interesting aspect of therapeutic circuits is their programmability. Replacing the sensor in the current circuits could retarget them to other cancer drivers such as MYC, β -catenin, or other oncogenes. In fact, circuits do not need to respond to oncogenes at all, but could be designed to sense any protein or combination of proteins that provide an accurate signature of disease state. Similarly, circuit outputs could also be broadened to include release of cytokines or activation of other therapeutic responses [7,8]. Together, these results establish a potent, specific, and programmable mechanism for treating cancer and other human diseases.

CHAPTER 5 BIBLIOGRAPHY

1. Fontana P, Du G, Zhang Y, Zhang H, Vora SM, Hu JJ, et al. Small-molecule GSDMD agonism in tumors stimulates antitumor immunity without toxicity. Cell. 2024;187: 6165–6181.e22. doi:10.1016/j.cell.2024.08.007
2. Oltra SS, Colomo S, Sin L, Pérez-López M, Lázaro S, Molina-Crespo A, et al. Distinct GSDMB protein isoforms and protease cleavage processes differentially control pyroptotic cell death and mitochondrial damage in cancer cells. Cell Death Differ. 2023;30: 1366–1381. doi:10.1038/s41418-023-01143-y
3. Kong Q, Xia S, Pan X, Ye K, Li Z, Li H, et al. Alternative splicing of GSDMB modulates killer lymphocyte-triggered pyroptosis. Sci Immunol. 2023;8: eadg3196. doi:10.1126/sciimmunol.adg3196
4. Cheng Q, Wei T, Farbiak L, Johnson LT, Dilliard SA, Siegwart DJ. Selective organ targeting (SORT) nanoparticles for tissue-specific mRNA delivery and CRISPR-Cas gene editing. Nat Nanotechnol. 2020;15: 313–320. doi:10.1038/s41565-020-0669-6
5. Hou X, Zaks T, Langer R, Dong Y. Lipid nanoparticles for mRNA delivery. Nat Rev Mater. 2021;6: 1078–1094. doi:10.1038/s41578-021-00358-0
6. Masarwy R, Stotsky-Oterin L, Elisha A, Hazan-Halevy I, Peer D. Delivery of nucleic acid based genome editing platforms via lipid nanoparticles: Clinical applications. Adv Drug Deliv Rev. 2024;211: 115359. doi:10.1016/j.addr.2024.115359
7. Aldrete CA, Call CC, Sant’Anna LE, Vlahos AE, Pei J, Cong Q, et al. Orthogonalized human protease control of secreted signals. bioRxiv. 2024. p. 2024.01.18.576308. doi:10.1101/2024.01.18.576308

8. Vlahos AE, Kang J, Aldrete CA, Zhu R, Chong LS, Elowitz MB, et al. Protease-controlled secretion and display of intercellular signals. Nat Commun. 2022;13: 912. doi:10.1038/s41467-022-28623-y